

THESIS FOR THE DEGREE OF DOCTOR OF PHILOSOPHY

Noise and electrical properties of YBCO nanostructures

EDOARDO TRABALDO



CHALMERS
UNIVERSITY OF TECHNOLOGY

Department of Microtechnology and Nanoscience - MC2
Quantum Device Physics Laboratory
CHALMERS UNIVERSITY OF TECHNOLOGY
Göteborg, Sweden 2020

Noise and electrical properties of YBCO nanostructures

EDOARDO TRABALDO
ISBN 978-91-7905-268-3

© EDOARDO TRABALDO, 2020.

Doktorsavhandlingar vid Chalmers tekniska högskola
Ny serie nr. 4735
ISSN 0346-718X

Quantum Device Physics Laboratory
Department of Microtechnology and Nanoscience- MC2
Chalmers University of Technology
SE-412 96 Göteborg, Sweden
Telephone +46 31 772 1000

Cover: Top left: SEM image of a grooved Dayem bridge (GDB), see chapter 5. Bottom left: Magnetic field noise of a GDB-based SQUID magnetometer at $T = 77$ K, see chapter 5. Top right: SEM image of two X-bars, see chapter 7. Bottom right: Noise spectrum of an X-bar at $T = 140$ K showing signatures of anti-correlation, see chapter 7.

Printed by Reproservice
Göteborg, Sweden 2020

Noise and electrical properties of YBCO nanostructures

EDOARDO TRABALDO

Department Microtechnology and Nanoscience
Chalmers University of Technology
Göteborg, Sweden 2020

Abstract

This thesis work deals with the investigation of noise properties in cuprate High critical Temperature Superconductor (HTS) $\text{YBa}_2\text{Cu}_3\text{O}_{7-\delta}$ (YBCO) nanoscale devices. Here the aim is to get a better understanding of nanoscale fluctuations in the normal state of HTSs from which superconductivity evolves. The observation of fluctuations in the electronic properties might offer valuable clues toward the microscopic mechanism leading to superconductivity in HTSs, which still represent one of the main unsolved problems in solid-state physics. In this respect, the YBCO nanodevices are implemented as tools to obtain new experimental signatures, which can deliver new insights about the complex properties of HTS materials. Since cuprate HTS undergo various nano-scale ordering transitions upon cooling and variation of hole doping, being able to study transport properties on the nanoscale is of utmost importance. In this respect, resistance noise properties of YBCO nanowires are studied as a function of temperature and hole doping. Indications of nematic fluctuations, that is local time dependent fluctuations of the in-plane conductivity anisotropy, have been observed in a wide temperature range above the superconducting transition. The observed fluctuations might be related to so-called charge stripe fluctuations, which represent a possible microscopic mechanism for superconductivity in these materials.

However, the interest in HTS nanostructures is not purely academic. The technological application of YBCO weak links in superconducting quantum interference devices (SQUIDs), is a major focus of research in the field of superconducting sensors such as ultra-sensitive magnetometers. In this thesis, we present a novel fabrication process of HTS weak links: the nanoscale Grooved Dayem Bridge (GDB). Here, the layout of the bridge and the weak link inside the bridge are realized during one single lithography process on a YBCO film grown on a single crystal substrate. This results in high-quality weak links with $I_c R_N$ products as high as $550 \mu\text{V}$ and differential resistances much larger than those observed in bare Dayem bridges at $T = 77 \text{ K}$. Moreover, the GDB greatly simplifies the fabrication procedure compared to grain boundary based JJs. We have used YBCO GDBs as novel nanoscale building blocks in HTS SQUID magnetometers coupled to an in plane pickup loop, which have been characterized via transport and noise measurements at $T = 77 \text{ K}$. These devices exhibit large voltage modulations ($\Delta V = 27 - 50 \mu\text{V}$), low values of white magnetic flux noise, $6 \mu\Phi_0/\sqrt{\text{Hz}}$, and corresponding magnetic field noise, $63 \text{ fT}/\sqrt{\text{Hz}}$, at $T = 77 \text{ K}$. Therefore, GDB based SQUIDs combine the nanofabrication advantages and the device reproducibility, which are typical of Dayem bridges, with the performances, i.e. low magnetic flux and field noise, of state-of-the-art SQUIDs based on grain boundary JJs. The achieved magnetic field noise paves the way for the realization of a single layer YBCO magnetometer with magnetic field noise below $20 \text{ fT}/\sqrt{\text{Hz}}$.

Keywords: HTS, SQUID, noise, YBCO, nanowire.

Acknowledgements

So many people need to be acknowledged, but I will try to be brief so you can quickly read and move on to enjoy this thesis.

To start with my supervisors, Thilo and Floriana, I will never thank you enough for the opportunity you gave me. I could not have asked for more supportive and inspiring person to work with. You have been an endless source of knowledge and, most of all, you impressed upon me a love for science and a dedication to research, which I will never forget.

Together with my supervisors, thanks to all the friends and members of our group: Eric, Gunta, Ananthu and Xavier. It was great to work and have fun together.

Thanks to all the components of the QDPL who contributed to make such a nice and engaging work environment. A special thanks to the SQUID LAB: Silvia, Chris, Alex, Justin and Dag, you have been close and helpful to me, both scientifically and as friends.

Thanks to all the other co-workers, friends and acquaintances at MC2 and around Chalmers university, who have contributed to this work, in a way or another.

This thesis work would not have been possible without the amazing work of our cleanroom staff here at MC2. I am specially thankful to Henrik and Mats for their help and support.

Thanks Riccardo, old Marco and Domenico, between a limoncello, a pizza and a black eye, you have been among my closest friends in Sweden.

Thanks Marco Scigiliuzzo and Sobhan, you may not be the friends I wanted, but I am very happy you are the one I got.

Grazie alla mia famiglia per il vostro continuo amore e supporto, i miei successi sono tanto vostri quanto miei. Grazie pa e ma per avermi insegnato a dare sempre il meglio, siete sempre nel mio cuore.

And the best for last, thanks Marina for putting a smile on my face everyday. I love you!

Edoardo Trabaldo, Göteborg, March 2020

List of appended papers

This thesis is based on the work contained in the following papers:

- I. **Improved noise performance of ultrathin YBCO Dayem bridge nanoSQUIDs**
Riccardo Arpaia, Marco Arzeo, Reza Baghdadi, **Edoardo Trabaldo**, Floriana Lombardi, Thilo Bauch
Superconductor Science and Technology, 30.1, 014008 (2016)
- II. **Noise properties of YBCO Nanostructures**
Edoardo Trabaldo, Marco Arzeo, Riccardo Arpaia, Reza Baghdadi, Eric Andersson, Floriana Lombardi, Thilo Bauch
IEEE Transactions on Applied Superconductivity, 27(4), 1-4, (2017).
- III. **Probing the phase diagram of cuprates with YBCO thin films and nanowires**
Riccardo Arpaia, Eric Andersson, **Edoardo Trabaldo**, Thilo Bauch, and Floriana Lombardi
Physical Review Materials, 2.2, 024804 (2018).
- IV. **Grooved Dayem Nanobridges as Building Blocks of High-Performance YBCO SQUID Magnetometers**
Edoardo Trabaldo, Christoph Pfeiffer, Eric Andersson, Riccardo Arpaia, Alexei Kalaboukhov, Dag Winkler, Floriana Lombardi, Thilo Bauch
Nano letters, 19.3, 1902-1907 (2019).
- V. **SQUID magnetometer based on Grooved Dayem nanobridges and a flux transformer**
Edoardo Trabaldo, Christoph Pfeiffer, Eric Andersson, Riccardo Arpaia, Alexei Kalaboukhov, Dag Winkler, Floriana Lombardi, Thilo Bauch
Submitted to *IEEE Transactions on Applied Superconductivity*, currently under review.
Preprint available at arXiv:1908.09875.
- VI. **Transport and noise properties of YBCO nanowire based nanoSQUIDs**
Edoardo Trabaldo, Riccardo Arpaia, Marco Arzeo, Eric Andersson, Dimitri Golubev, Floriana Lombardi, Thilo Bauch
Superconductor Science and Technology, 32.7, 073001 (2019).
- VII. **Electrical Properties of Grooved Dayem Bridge based YBCO Superconducting Quantum Interference Devices and Magnetometers**
E. Trabaldo, S. Ruffieux, E. Andersson, R. Arpaia, D. Montemurro, J. Schneiderman, A. Kalaboukhov, D. Winkler, F. Lombardi, and T. Bauch
Submitted to *Applied Physics Letter*
- VIII. **Noise anomalies in the resistive state of $\text{YBa}_2\text{Cu}_3\text{O}_{7-\delta}$ nanostructures with varying doping**

Edoardo Trabaldo, Riccardo Arpaia, Eric Andersson, Floriana Lombardi, Thilo Bauch
To be submitted to *Physical Review B*

Papers and book chapters which are outside the scope of the thesis:

I. **High Frequency Properties of Josephson Junctions**

Thilo Bauch, **Edoardo Trabaldo**, Floriana Lombardi

In: Tafuri F. (eds) Fundamentals and Frontiers of the Josephson Effect. *Springer Series in Materials Science*, vol 286 (2019).

II. **High transparency Bi_2Se_3 topological insulator nanoribbon Josephson junctions with low resistive noise properties**

Gunta Kunakova, Thilo Bauch, **Edoardo Trabaldo**, Jana Andzane, Donats Erts, Floriana Lombardi

Applied Physics Letters 115 (17), 172601 (2019).

III. **Fabrication and electrical transport characterization of high quality underdoped YBCO nanowires**

Eric Andersson, Riccardo Arpaia, **Edoardo Trabaldo**, Thilo Bauch, Floriana Lombardi

Submitted to *Sup. Sci. and Tech.*, arXiv preprint arXiv:1910.11062 (2019)

IV. **Untwinned YBCO thin films on MgO substrates: A platform to study strain effects on the local orders in cuprates**

Riccardo Arpaia, Eric Andersson, Alexei Kalaboukhov, Elsebeth Schroder, **Edoardo Trabaldo**, Regina Ciancio, Goran Drazic, Pasquale Orgiani, Thilo Bauch, Floriana Lombardi

Physical Review Materials, 3(11), 114804 (2019).

Contents

Abstract	iii
Acknowledgements	v
1 Introduction	1
2 Background	3
2.1 Superconductivity	3
2.2 YBCO	6
3 HTS-based devices	13
3.1 Nanoscale devices	13
3.2 Josephson effect	14
3.2.1 RSJ model	15
3.3 Superconducting quantum interference devices	16
3.3.1 Noise performances	17
3.4 HTS-based JJs and weak links	18
4 Nanowire-based SQUIDs	23
4.1 Nanowires	25
5 Properties and performances of GDB-based devices	29
5.1 Fabrication	29
5.2 Electrical properties of single GDB	31
5.3 GDB-based SQUIDS	36
5.3.1 Temperature dependence of electronic properties	37
5.4 Magnetometers	40
5.4.1 In-plane pick-up loop	40
5.4.2 Flip-chip Flux-transformer	44
5.5 Future considerations	46
6 Noise in nanowires	49
6.1 1/f noise model	50
6.2 Noise at $T = 100$ K	51
6.3 Dutta-Horn model	53

6.4	Noise for $T_c < T < 450$ K	55
6.5	TLFs analysis	56
7	Noise and anticorrelation	63
7.1	Model	63
7.2	Simulations	67
7.3	Results	70
8	Conclusions	73
Appendix A Nanowire fabrication		75
Bibliography		79
Appended papers		87

CHAPTER 1

Introduction

The phenomenon of superconductivity has been at the forefront of research in the field of condensed matter physics since its discovery, more than 100 years ago [1]. However, a new spark was ignited in the field when the first High critical Temperature Superconductor (HTS) was discovered [2]. These materials defy the theory developed to describe Low critical Temperature Superconductors (LTS), and add a new layer of complexity to the problem, due to their many inter-playing orders. As of now, after more than 30 years from the discovery of HTS, we still lack a comprehensive theory which describes the microscopic mechanism responsible for this phenomenon [3]. Superconductivity aside, there are more open questions regarding HTS: the pseudo-gap [4] and the strange metal phase [5] are just two examples of unexplained behaviour of these materials in their normal state. In the last decade, new properties of cuprates, the most studied class of HTS materials, have been reported, further complicating the problem. Different experiments have demonstrated unexpected spontaneous charge ordering in the form of charge density waves in these materials [6, 7].

Given the complexity of the problem, it is clear that we need new platforms and experiments to study HTSs and gain new insights [3]. In this thesis work we propose the study of the electrical properties of HTS nanostructures as a possible route to unravel the mystery. Electrical transport studies are a standard characterization tool in solid state systems. However, we can gather additional information on the microscopic behavior of cuprates by reducing the dimensions of our system, to approach the characteristic length scale of the various ordering phenomena. Since cuprate HTSs undergo various nanoscale ordering transitions upon cooling and variation of hole doping, being able to study transport properties on the nanoscale is of utmost importance. Therefore, we need to fabricate structures with dimensions in the nanoscale, which retain pristine material qualities. The work presented in this thesis is based on the characterization of nanostructures fabricated with $\text{YBa}_2\text{Cu}_3\text{O}_{7-\delta}$ (YBCO). This material is a cuprate and one of the most studied HTSs. YBCO nanodevices are implemented as tools to

obtain new experimental signatures, and deliver new insights about the complex properties of HTS materials. Our aim is to study the resistance noise properties of these nanostructures to possibly shine light on the dynamics of charge ordering. Noise measurements are instrumental to study properties of nanoscale fluctuations in the normal state of HTS which could not be accessed through standard transport measurements. The observation of fluctuations in the electronic properties might offer valuable clues toward the microscopic mechanism leading to superconductivity in HTSs.

Nanoscale YBCO devices are also instrumental for the technological development of HTS applications. The properties of HTSs, i.e. high critical temperature and critical magnetic field, makes them very attractive for technological applications. In this thesis we are interested in using YBCO nanoscale weak links, in particular nanowires, to fabricate SQUIDs and magnetometers. These sensors are important as tools for research and for commercial sensing technologies. Our aim is to build upon the high performance (low-noise) nanowire-based SQUIDs at temperatures below 20 K [8, 9] and overcome their limitations at high temperatures ($T = 77$ K)[10], where technological applications are more relevant.

This thesis provides an overview and the background for the work presented in the appended papers.

CHAPTER 2

Background

In the following we will introduce the basics of superconductivity with a chronological summary of the models developed in the field, up to the discovery of high critical temperature superconductors (HTSs). Particular attention is given to the key concepts which will be used in this thesis work. Thereafter, we give an overview of $\text{YBa}_2\text{Cu}_3\text{O}_{7-\delta}$ (YBCO), which is an HTS and is the base material for our work. We showcase the properties of YBCO, with emphasis on the open questions about the phase diagram, i.e. electronic properties as a function of temperature and doping, of this material, and the physics of HTSs in general.

2.1 Superconductivity

The phenomenon of superconductivity is characterized by two distinct and bewildering properties: perfect conductivity and perfect diamagnetism. The former is realized when a material has zero electrical resistance, e.g. a dc current flows without developing any voltage drop and without any energy loss. Perfect conductivity was first reported in 1904 by Camerling Onnes who observed a drastic drop in the resistance of Mercury, down to 0Ω , when cooling the material below a certain temperature [1]. This temperature is called the critical temperature T_c and is defined as the transition temperature from the normal state to what is later going to be known as the superconducting state (SC). T_c is an intrinsic property of the material, e.g. for Mercury $T_c \simeq 4.17$ K. The second property of a SC, the perfect diamagnetism or Meissner effect, was discovered in 1933 and refers to the tendency of a SC to expel from its bulk any externally applied magnetic field with value below a critical field B_c [11]. The Meissner effect is what discriminates between a superconductor, which displays a truly macroscopic quantum behavior, and a "trivial" perfect conductor.

One of the first models, which describes both the properties of a SC was developed in 1935 by the London brothers [12], after whom the model is named. The model describes

a two-fluid system where the first fluid represents the standard, resistive electrons. This is responsible for the finite values of conductivity at temperatures $T > T_c$. The second fluid, referred to as superfluid, represents the charge carriers which are responsible for superconductivity. The density of the superfluid, n_s , is equal to 0 for $T > T_c$, i.e. the normal state. However, for $T < T_c$, $n_s > 0$. In this regime, the superfluid abides the two London equations[12]:

$$\partial_t \vec{j}_s = \frac{n_s e^{*2}}{m^*} \vec{E} \quad (2.1)$$

$$\vec{\nabla} \times \vec{j}_s = -\frac{n_s e^{*2}}{m^*} \vec{B} \quad (2.2)$$

where \vec{j}_s is the superfluid current density, m^* and e^* are respectively the effective mass and charge of the superfluid charge carriers, and \vec{E} and \vec{B} are the electric and magnetic field, respectively.

In Eq. 2.1, a constant value of \vec{j}_s results in $\vec{E} = 0$. Hence, no voltage drop develops when a dc current flows in a SC. On the other hand, Eq. 2.2 describes the Meissner-state. This is more easily understood by combining this equation with Ampere's law, which gives:

$$\nabla^2 \vec{B} = \frac{1}{\lambda^2} \vec{B} \quad (2.3)$$

which implies the exponential decay of the magnetic field B inside the superconductor within a characteristic length scale λ . This length is called London penetration depth and it is defined as $\lambda = \sqrt{\frac{m^*}{\mu_0 n_s e^{*2}}}$. \vec{B} is expelled from the bulk of the SC by screening currents which circulate on the surface of the SC and, like \vec{B} , decay in the SC bulk over the same characteristic length λ .

After the London equations, one of the main contribution towards the understanding of superconductivity was the model developed by Ginzburg and Landau (GL) in 1950 [13]. The superfluid described by the London equations is assumed to be spatially constant, e.g. n_s is a constant. In the GL model, the superfluid properties (density and phase) can vary as a function of position \vec{r} . The GL model introduces the order parameter $\Psi(\vec{r})$, which holds spatial information on the density $n_s(\vec{r})$ and phase $\phi(\vec{r})$ of the superconducting fluid. This order parameter can be written as:

$$\Psi(\vec{r}) = |\Psi(\vec{r})| e^{i\phi(\vec{r})} \quad (2.4)$$

where $|\Psi(\vec{r})| = \sqrt{n_s(\vec{r})}$. However, the properties of Ψ can change only on a length scale larger than ξ , which is called the coherence length. λ and ξ are characteristic lengths, which depend on the material.

However, the GL theory is a phenomenological model and a successful microscopic description of the mechanism responsible for superconductivity was not developed until 1967 when Bardeen, Cooper and Schrieffer (BCS) [14] proposed a mechanism for the pairing of electrons. Generally, two particles with the same charge polarity repel each other due to Coulomb interaction. However, in certain conditions an attractive interaction, mediated by phonons, can form between two electrons, creating a so-called Cooper-pair. Single electrons are fermions, i.e. they have half integer spin value, thus

Material	Type	T_c [K]	λ [nm]	Δ [meV]	ξ [nm]	$H_c; H_{c,2}$ [T]
Al	LTS	1.2	16	0.2	1600	0.01
Nb	LTS	9	44	1.5	40	3
NbN	LTS	16	200	1.5	5	20
YBCO	HTS	93	150-300	20-25	1-3	250

Table 2.1: Summary of the main Superconductive parameters for some of the most common LTS materials compared to YBCO [17, 18]. The value of H_c are reported for the type-I SC (Al), while the upper critical field, $H_{c,2}$, is reported for the type-II SCs (Nb, NbN and YBCO). As introduced in Section 2.2, YBCO has anisotropic properties, which depend on the crystal direction. In this table, we report the properties of the ab -plane since we use c -axis oriented YBCO films for fabrication of nanostructures.

they obey Fermi-Dirac statistic, which forbids two electrons in a system from occupying the same quantum state. On the other hand, Coopers-pairs have integer spin value (sum of two half-integer spins) and thus are bosons, which can occupy the same quantum state. After formation, Cooper-pairs condense into the same ground state, which can be described by the wavefunction given in Eq. 2.4. For $T < T_c$, it is energetically favourable for electrons to form Cooper-pairs, the binding energy of a pair is called superconducting energy gap 2Δ . This energy is a property of the material and can be written as[15] $\Delta \simeq 2\hbar\omega_D e^{-1/N(E_F)g_{\text{eff}}} \simeq 1.76k_B T_c$, where ω_D is the Debye frequency, $N(E_F)$ is the electron density of states at the Fermi energy E_F , k_B is the Boltzmann constant and g_{eff} is the effective electron-phonon coupling.

The BCS theory successfully describes the phenomenon of superconductivity at low temperatures and is used to model low critical temperature superconductors (LTS). However, in 1986 Bednorz and Müller reported superconductivity in a class of materials called cuprates [2]. This is the discovery of the first High Critical Temperature superconductor (HTS). HTS materials exhibit superconducting behavior at temperatures much higher than what observed previously. In fact, while BCS theory predicts the highest possible critical temperature to be $T_c = 32$ K, HTS materials have critical temperatures well above the boiling point of liquid nitrogen (LN_2) $T = 77$ K, e.g. bulk YBCO, a common cuprate HTS, showed $T_c = 93$ K [16]. The behavior of HTSs cannot be explained in terms of the BCS theory and the formulation of a comprehensive theory, which describes the microscopic origin of high- T_c superconductivity is still the subject of intensive studies as of today.

In general, the critical temperature is not the only parameter which differentiates HTSs from LTSs. In contrast to LTSs, which are usually metals, HTSs are materials with a complex crystal structure and SC properties strongly tied to their charge doping. Moreover, the value of the parameters λ , ξ and Δ change drastically between the two classes of SC. A summary of the parameters for some of the most common LTS materials are compared to YBCO in Table 2.1. As it is expected from the expression for Δ , HTS materials exhibit a much higher energy gap given the increased T_c . Moreover, the London penetration is larger as compared to LTS mainly due to the lower carrier concentration, while the coherence length is decreased.

One can divide SCs in two categories, i.e. type-I or type-II, depending on the ratio λ/ξ . For $\lambda/\xi > 1/\sqrt{2}$, the SC is type-I. For these materials, when an applied magnetic field B_a exceeds the critical field H_c , superconductivity is broken and the material

is driven to the normal state ($n_s = 0$). In contrast, for type-II SC ($\lambda/\xi < 1/\sqrt{2}$), when B_a exceeds the lower critical field $H_{c,1}$, the material transitions to the so-called *mixed state*. In this regime, it is energetically favourable for the SC to let some of the magnetic field enter its bulk in the form of Abrikosov vortices [19] (also referred to as fluxons). Here, the order parameter is locally suppressed ($\vec{\Psi} \simeq 0$) over a length scale equal to ξ , forming the *normal* ($n_s = 0$) core of the fluxon. A supercurrent circulates around the core, decaying into the SC over a distance equal to λ . The spatial integral of the resulting magnetic field (both externally applied and the one originating from the circulating currents) over the whole vortex area equals exactly one flux quantum $\Phi_0 = h/2e$. The number and spatial arrangement (or lattice) of the vortices depend on B_a . However, when the applied field reaches the upper critical field $H_{c,2}$, superconductivity is completely broken and the material is driven to the normal state. Most devices based on type-II SCs are functioning even when the material enters the *mixed state* and since $H_{c,2} \gg H_c$ ($H_{c,2} \simeq 100$ T for YBCO), these devices have significantly improved working range in terms of magnetic field compared to their LTS counterpart.

The lack of a microscopic theory which describes the origin of superconductivity in HTSs is only one of the mysteries surrounding these materials. Indeed, the behavior of HTSs in the normal state ($T > T_c$) shows anomalies which are also the subject of extensive research. Moreover, the physical properties of some HTSs are strongly tied to their level of charge doping, adding a layer of complexity to the problem. An overview of the research conducted on cuprates, the most diffused class of HTSs, will be presented in the following section. We will focus on the properties of YBCO, the material which is the base for this thesis work, and is one of the most studied cuprates.

2.2 YBCO

As introduced above, YBCO is a cuprate and one of the most studied HTSs in the field. The crystal unit cell of $\text{YBa}_2\text{Cu}_3\text{O}_{7-\delta}$ is shown in Fig. 2.1. It has the characteristic layered structure of cuprate HTSs, with one or more CuO_2 planes per unit cell, which is shared by all cuprate materials. The unit cell of YBCO is composed of three perovskite cells separated by two CuO_2 planes. This quasi-two-dimensional layered structure results in a strong anisotropy of the superconducting and normal state properties along the c -axis compared to the ab -plane. In the absence of dopant elements ($\text{YBa}_2\text{Cu}_3\text{O}_6$ in Fig. 2.1) the cell structure is tetragonal, i.e. the lattice parameters along the a - and b -direction are the same, $a = b$, and the material is a Mott insulator [20].

The addition of oxygen atoms results in hole doping of YBCO CuO_2 planes, and formation of CuO chains along the b -axis, as shown for $\text{YBa}_2\text{Cu}_3\text{O}_7$ in Fig. 2.1. The CuO chains act as charge reservoirs for the CuO_2 planes, which are the main sites for electric conduction. Here, the hole doping is the result of electron transfer from the planes to the chains [21]. The formation of the CuO chains due to the additional oxygen atoms results in the deformation of the YBCO unit cell, which becomes anisotropic and elongated along the b -axis (orthorhombic crystal structure). This leads to anisotropy of the superconducting properties (e.g. λ , ξ and Δ) between the a - and b -axis [22, 23, 24, 25, 26], albeit on a much lower scale as compared to the anisotropy between the

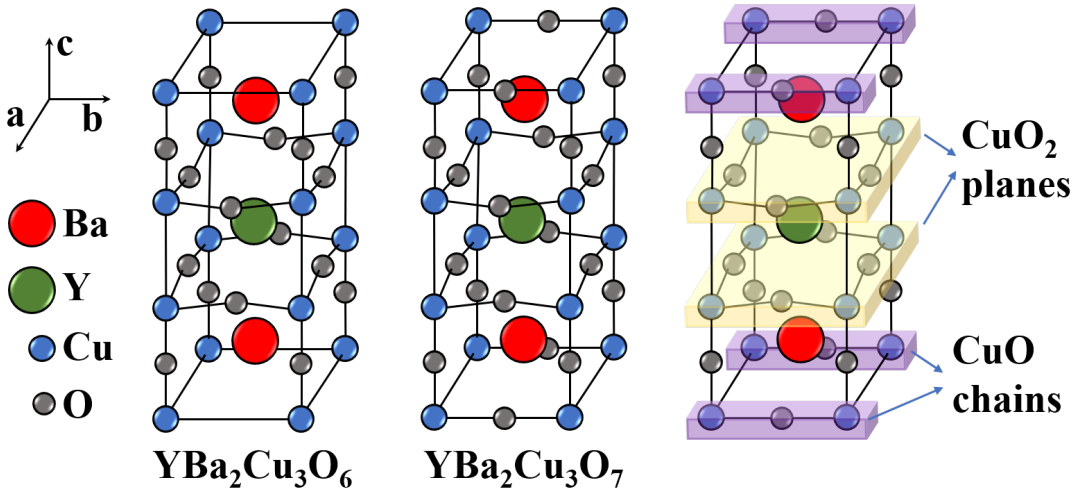


Figure 2.1: Schematic of a YBCO unit cell with no additional oxygen doping ($\mathbf{YBa}_2\mathbf{Cu}_3\mathbf{O}_6$) and with all the doping sites occupied ($\mathbf{YBa}_2\mathbf{Cu}_3\mathbf{O}_7$). The position of the \mathbf{CuO}_2 planes and \mathbf{CuO} chains are highlighted for the case of $\mathbf{YBa}_2\mathbf{Cu}_3\mathbf{O}_7$.

c-axis and the *ab*-planes. Moreover, due to the anisotropic unit cell, YBCO can be either *twinned* or *untwinned* [22, 27]. The latter, refers to samples of YBCO where the crystallographic orientation is preserved throughout the material, i.e. there is no alternation of the *a*- and *b*-axis along a \mathbf{CuO}_2 plane. On the other hand, twinning is caused by random in-plane exchange of the *a*- and *b*-axis. In this case, the SC properties of YBCO are expected to be isotropic in the *ab*-plane.

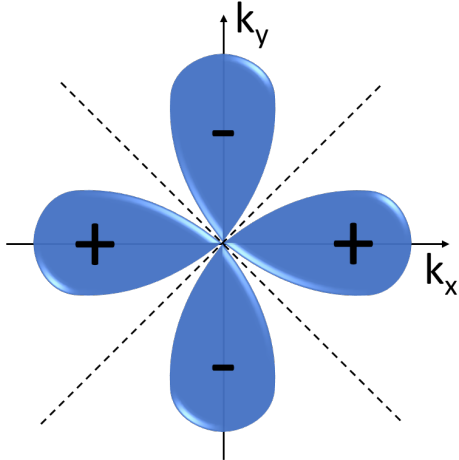


Figure 2.2: Sketch of the order parameter with $d_{x^2-y^2}$ symmetry (*d*-wave) in YBCO.

The oxygen vacancies in the chains, δ , play a key role in the electrical and superconductive properties of YBCO. For example, as shown in Fig. 2.3, T_c is a function of δ . Here, the hole doping per planar Cu atom, p , is commonly used to express the doping level of YBCO. Depending on p , the material can be defined as *overdoped*, *optimally doped* or *underdoped*, which corresponds to $p > 0.16$, $p \simeq 0.16$ and $p < 0.16$, respectively [28]. Optimally doped YBCO shows the highest values of critical temperature, while T_c decreases in the underdoped and overdoped regime. For $p = 0.16$, the lattice parameters of the YBCO unit cell are $a = 3.82$ Å, $b = 3.89$ Å and $c = 11.69$ Å [29].

In the superconducting state, the order parameter symmetry of YBCO differs from the characteristic *s*-wave type of LTSs, and has instead a $d_{x^2-y^2}$ symmetry (*d*-wave), as shown in Fig. 2.2.

As a consequence, the energy gap of YBCO is anisotropic in the k -space as $\Delta(\vec{k}) = \Delta_0(\cos(k_x a) - \cos(k_y a))$ [30, 31]. The energy gap has lobes along the directions of the k_x and k_y axes (which correspond to the *a* and *b* YBCO crystal axes). The or-

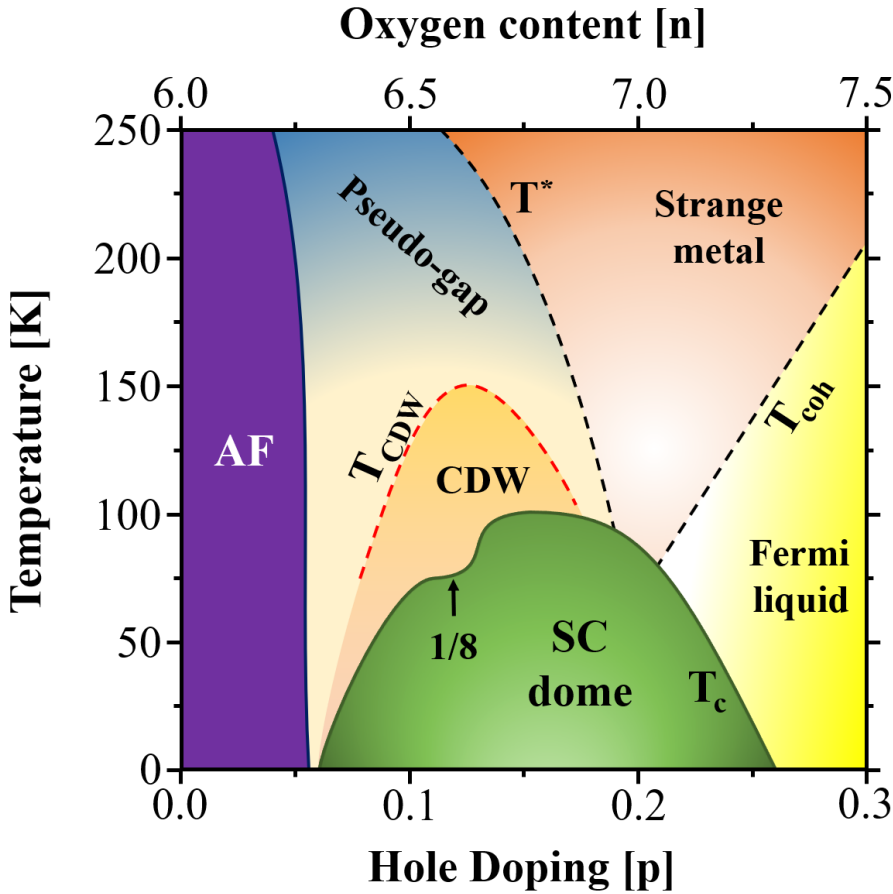


Figure 2.3: Phase diagram of YBCO with the most relevant interplaying orders and transition temperatures.

der parameter is suppressed for pure d -wave symmetry along the nodal lines at 45° . However, experimental evidences demonstrate the presence of a sub-dominant complex component *is* which results in non-zero order parameter along the nodal lines and full superconducting gap [32].

Superconductivity is only one piece of the HTS puzzle: the many interplaying orders which add to the mystery of these materials are found in the normal state and, as for superconductivity, they are doping dependent. The interplaying phases which characterize the electric and magnetic properties of cuprates are well represented as a function temperature and doping by the material phase diagram. As an example, a schematic of the phase diagram of YBCO is shown in Fig. 2.3. Here, the electrical properties of the material are shown as a function of hole doping, p , and temperature, T . Most of the phase diagram features are shared among all cuprates, albeit shifted to different temperatures and doping levels. The phase diagram of Fig. 2.3 shows a plethora of phases, which depend on doping and temperature. Many of the open questions regarding YBCO, and cuprates in general, are tied to the origin of these phases and their relation to each other, especially to superconductivity. Following the phase diagram of YBCO, the major phases which characterize the material are:

- **SC (Superconductor):** This region is commonly referred to as the *superconducting dome*. Here, T_c indicates the critical temperature and is a function of hole doping, p . The dome has two plateaus, the first at $p = 0.16$ ($T_c \simeq 93$ K) in correspondence of the optimal doped region, and the second at $p = 0.125$. The latter is referred to as 1/8 doping and its origin is believed to be related to the occurrence of (quasi-)static charge density wave order (see below), which competes with superconductivity [33].
- **Strange metal:** In correspondence of the optimally doped region, the strange metal regime is characterized by a linear dependence of the material resistance as a function of temperature, $R \propto T$. This phase is not fully understood and usually described as a *marginal fermi liquid* [34]. However, recently it has been proposed that the linear resistance might be the result of the material being in a new state, called *many body entangled compressible quantum matter*[5]. This might hold the key to understand the phenomenon of high- T_c superconductivity.
- **Pseudo-gap:** Several experimental techniques have confirmed the existence of a pseudogap region [35] for $T > T_c$ in the underdoped regime, which persists up to T^* , the pseudo gap temperature. However, the origin of the pseudogap, and its role in connection to superconductivity as competitor [36] or precursor [4], are still under debate.
- **CDW (Charge Density Wave):** Recent experiments [6, 37, 38, 39, 40] revealed the formation of (quasi-)static charge density modulations in the CuO₂ planes, called Charge Density Waves (CDW), which are incommensurate with the lattice period and ubiquitous to all cuprates. For YBCO, these modulations appear in the form of stripes in the underdoped regime for $T_{\text{CDW}} > T$. CDW order is still observable below T_c , although with a suppression of amplitude and reduction of coherence length upon cooling below T_c . This supports the notion of CDW being a competing order to superconductivity. Moreover, the maximum intensity of CDW is found for $p = 1/8$, corresponding to the suppression of T_c in the superconducting dome. The typical correlation lengths of CDW order are below 10 nm [6, 37]. The CDW correlation length can be interpreted as the patch size of a single CDW domain.
- **Fermi liquid:** YBCO behaves as a metal, the transition temperature between metallic and strange metal is T_{coh} , in the Fermi liquid region the resistance is $R \propto T^2$.
- **AF (Antiferromagnetic):** YBCO is a Mott insulator and has antiferromagnetic properties for low doping $p < 0.05$;

As described above, HTSs represent one of the most interesting and complex problem in solid-state physics and, after more than 30 years from the discovery of HTS, many questions remain open. What is the microscopic origin of high- T_c superconductivity and what is the role of the normal state phases (e.g CDW, pseudogap and strange metal) in relation to this phenomenon? To find the answers, one needs to go beyond standard characterization techniques and approach the problem from a new

perspective [3]. In this work, we focus on two key aspects for the study of the normal state properties of YBCO: reduced sample sizes and the dynamic electronic properties of this material. Our scope is first to fabricate nanostructures, which approach the characteristic length scales of the charge ordering phenomena. Second, perform resistance noise measurements to gather information on the electronic fluctuations in the nanostructures. Noise measurement can be instrumental to unveil new properties of the cuprates normal state which otherwise could not be accessed through standard (averaged) dc characterization techniques.

The idea of studying the dynamic electronic properties of YBCO gains importance in light of the numerous proposed models, which relate the phenomenon of high- T_c superconductivity to the presence of fluctuating charge stripes in HTSs. A key element in these models is the role of fluctuating charge stripes in establishing a superconducting order parameter. Here, two main pictures emerge from the various models. The first, proposes a BCS-like mechanism of pairing (see [41] for an overview), in which the fluctuating stripes act as the mediating boson ("glue") for the superconducting pairing of electron-like quasiparticles. The second approach is derived from the strongly correlated electron picture [42], where charge stripes are considered as one-dimensional systems. Within this stripe model, fluctuations of those one-dimensional stripes causes frustration of the dominant CDW order mechanisms causing the subdominant superconducting order to prevail. In this sense superconductivity occurs within the stripes themselves (see [43] for an overview).

Besides the fundamental aspects of HTSs, these materials are at the same time also very attractive for technological applications. The larger Δ would be beneficial for high power and large scale applications operational at liquid nitrogen temperature ($T = 77$ K), moreover, the large upper critical field, $H_{c,2}$, makes HTSs ideal candidates for the fabrication of ultra-high field magnets. The large critical field and the high T_c also extend significantly the range of working conditions of HTS devices. The high critical temperature also eliminates the need of liquid helium cooling (which is not only costly but He is also a limited resource) and opens the possibility for more compact, or even portable, sensing equipment. Overcoming the issues related to HTS fabrication, could usher a new era of technological applications for superconductors. In this respect, we apply the same nanofabrication process on YBCO for 1) the study of fluctuations in the electronic properties (noise) in YBCO nanostructures, and 2) the development of a new type of nanoscale YBCO weak link for the realization of a SQUID based magnetometer operational at $T = 77$ K.

The complexity conveyed by the phase diagram of HTS is matched by the challenges which have to be overcome to fabricate high-quality samples, especially for cuprates and for dimensions in the nanoscale. First, while the most common LTSs are monoatomic (e.g. Al and Nb), HTSs are complex materials which generally contain different heavy metals and other exotic atoms. This limits the number of techniques which can preserve the material stoichiometry during deposition of the thin films and achieve high quality samples. Moreover, the deposition of YBCO requires a substrate heated at high temperatures (over 700 K for pulsed laser deposition), which is not compatible with standard lithographic processing, such as lift-off. Cuprates are ceramic materials,

which are prone to defects and are brittle, limiting the quality of the deposited thin films. Some cuprates are also chemically reactive to water and common solvents used during fabrication. A crucial aspect of YBCO, especially for $p < 0.15$, is oxygen out-diffusion, even at moderate temperatures ($T \simeq 100$ C), which consequently alters the SC properties. Oxygen out-diffusion is very difficult to control at the nanoscale, limiting the smallest features which can be achieved during nanofabrication. All this factors make the fabrication of nanostructures very challenging and often not reproducible.

2. Background

CHAPTER 3

HTS-based devices

As introduced in Section 2, the fundamental aspects of HTS materials represent a major research field and, for more than 30 years, researchers have been trying to explain the microscopic mechanism of superconductivity in these materials. One of the main boost to both the study of fundamental aspects and application of HTS came from the improvement of nanofabrication techniques applied to HTS devices, enabling control of the dimensions down to the nanoscale.

However, the interest in these devices is not purely academical, the enhanced critical temperature and upper critical field makes HTS devices promising for technological applications. In this chapter we will introduce two of the basic application of superconductors, the Josephson effect and the superconducting quantum interference device.

3.1 Nanoscale devices

The *recently* discovered CDW order, together with the other phases of YBCO, prompted the investigation of HTSs at the nanoscale. In fact, the characteristic size (coherence length) of a charge density wave patch in cuprates is in the nanoscale. The maximum coherence length of 10 nm is reached for $p = 1/8$ and $T = T_c$ [6, 37]. Very recent work has reported the presence of dynamic charge fluctuations [44] for a wide range of p and T (much larger than what expected for CDW). The common characteristic for all these phenomena is the small coherence length (on the nanometer scale): the most interesting and unexplored physics is predominant at the nanoscale. By fabricating mesoscopic structures, we can explore the electrical properties of YBCO on the same length scale of these nanoscale ordering phenomena.

For this purpose, it is necessary to fabricate samples which can retain bulk properties for reduced lateral dimensions, down to tens of nanometer. If the sample under study is damaged by the fabrication, the defects would dominate the electrical prop-

erties, precluding the study of intrinsic properties of the material. As introduced in Section 2.2, nanofabrication is particularly challenging for cuprates, however, its improvement is of paramount importance also for the technological applications of HTSs. As shown in the following sections, small sizes, comparable to the coherence length, are necessary also for the fabrication of high performance Josephson Junctions (JJs) and weak links, which are the key elements of superconducting electronics and sensors.

The aim of this work is to improve upon the standard fabrication procedure (see Appendix A) to obtain pristine nanostructures. These are used as the platform to further advance our understanding of the resistance noise in the normal state of HTS and to improve the performance of YBCO-based magnetic flux sensors. In the following sections we will introduce the concept of JJs and superconducting weak links, and the working principle of SQUIDs.

3.2 Josephson effect

One of the fundamental application of SCs is the Josephson Junction (JJ). The Josephson junction was first proposed by Brian Josephson in 1962 and it is based on the *Josephson effect*[45]: the transfer of Coopers-pairs through a barrier which separates two superconductors. When a SC is in contact with a normal conductor (N), the condensate wave function Ψ extends from the SC into the normal conductor, decaying exponentially. When two SCs are separated by a small barrier, their wave functions can overlap inside N, allowing the transfer of Cooper-pairs and giving rise to the Josephson effect. JJs have been instrumental to study the properties of SC materials and are the key elements for most superconducting applications (e.g. SQUID [46, 47] and voltage standard [48, 49]). There are two fundamental equations governing the dynamics of a JJ, these are:

$$I = I_c \sin(\phi) \quad (3.1)$$

$$V = \frac{\hbar}{2e} \frac{\delta\phi}{\delta t} \quad (3.2)$$

The first is the DC Josephson equation or the Current Phase Relation (CPR) of the JJ, i.e. the relation between the supercurrent I flowing through the JJ and the phase difference of the two electrode wave-functions across the barrier ϕ . A supercurrent can flow without voltage drop when ϕ has constant value, as long as I is lower than the critical current I_c . The second equation is the AC Josephson equation, which describes the time evolution of the phase difference ϕ and its relation to the voltage drop across the junction V .

A JJ can be achieved with different types of barriers. When an insulator is sandwiched between two SCs the JJ is called SIS (Superconductor-Insulator-Superconductor), if a metal is used instead of the insulating barrier, the JJ is referred to as SNS (Superconductor-Normal conductor-Superconductor). The Josephson effect can also be realized in structures called *weak links*. Among the different type of weak links the most common is the SS'S. Here, the S' is a superconductor with different superconducting properties compared to S. This can be achieved by using a superconducting link which has a lower critical temperature or reduced geometrical dimensions (constriction-type of weak link) as compared to the electrodes.

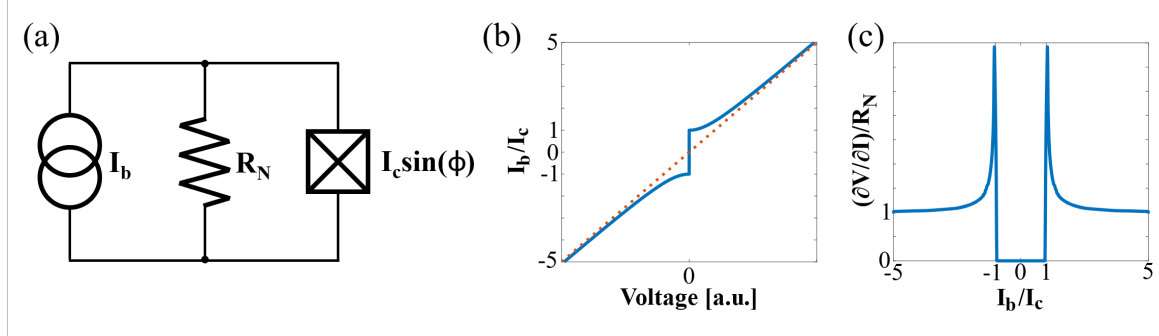


Figure 3.1: (a) Circuit schematic for the RSJ model. (b) Current Voltage characteristic of a JJ in the RSJ model, I_b is normalized by I_c . The dashed, red line shows the normal resistance, R_N . (c) Differential resistance calculated from the IVC shown in panel (b). The value of $\partial V / \partial I$ is normalized by the normal state resistance R_N

3.2.1 RSJ model

The model introduced above describes the properties of a JJ in terms of phase ϕ , however for most applications it is more relevant to understand the Current-Voltage Characteristic (IVC) of a JJ, e.g. the relation which ties directly current to voltage. A JJ is typically characterized by connecting it to a bias current source I_b and measuring the corresponding voltage drop V . For $I_b < I_c$, the voltage drop according to the Josephson equations (Eq. 3.1 and 3.2) is $V = 0$. To derive the voltage drop for currents above I_c one can use the Resistively Shunted Junction (RSJ) model. Here, the expression for $V(I_b > I_c)$ is obtained by solving the circuit shown in Fig. 3.1. Here, the JJ is connected in parallel to a resistor R_N which represents the normal state resistance of the junction. For simplicity the normal state resistance is assumed to be ohmic, i.e. independent of voltage. The total current flowing through the circuit of Fig. 3.1(a) can be expressed as:

$$I_b = I_c \sin(\phi) + \frac{V}{R_N} = I_c \sin(\phi) + \frac{\hbar}{2eR_N} \frac{d\phi}{dt} \quad (3.3)$$

where Eq. 3.2 was used to express the voltage drop over R_N . By integrating Eq. 3.3 over time, one obtains the expression for the average voltage:

$$\langle V \rangle = R_N \sqrt{I_b^2 - I_c^2} \quad (3.4)$$

for $I_b < I_c$, the JJ is in the superconductive state and $\langle V \rangle = 0$. The current voltage characteristic (IVC), and differential resistance, $\partial V / \partial I$, of a RSJ are shown in Fig. 3.1(a) and (b), respectively. When I_b is increased above the critical current, the voltage increases rapidly and the differential resistance $\partial V / \partial I$ is much higher than the normal state resistance R_N . When I_b is further increased, the JJ behaves more similarly to a linear resistor with resistance approaching R_N .

The RSJ model is a special case of the Resistively and Capacitively Shunted Junction (RCSJ) where the capacitance of the Junction has been neglected. The RCSJ model is more suitable to describe a SIS junctions. The IVC of a RCSJ is characterized by hysteresis between positive and negative current bias sweeps, which is detrimental in some technological applications, especially for SQUIDS.

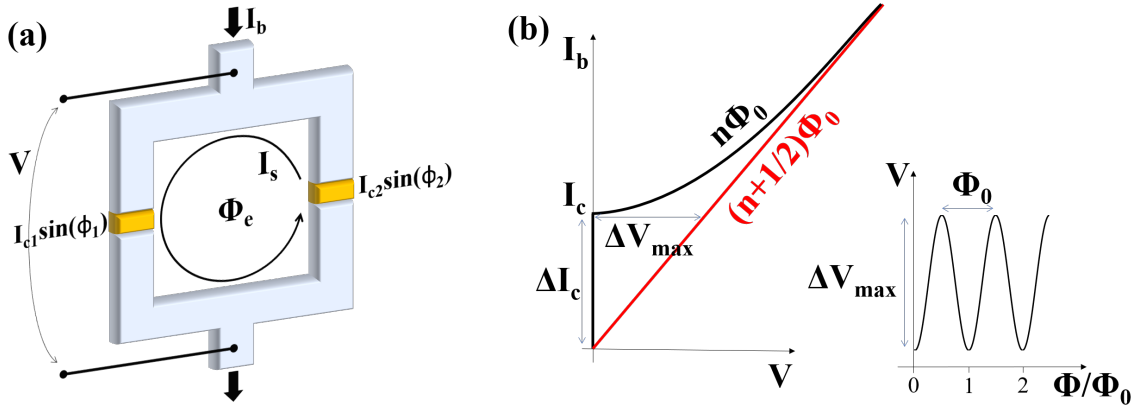


Figure 3.2: (a) Schematic of a DC SQUID where a superconducting loop is interrupted by two JJs. (b) IVC modulation for integer and half integer values of applied magnetic flux. Inset: SQUID voltage signal as a function magnetic flux.

3.3 Superconducting quantum interference devices

One of the most prominent application of SCs is the Superconducting QUantum Interference Device (SQUID). The working principle of a SQUID is based on the quantization of the magnetic flux through a superconducting loop. A dc SQUID is, in its simplest form, composed of a SC loop interrupted by two JJs, as shown in Fig. 3.2(a). The same result can be achieved with weak links (e.g. nanowires) instead of JJs. When the SQUID is biased with a dc current, I_{SQ} , we can write:

$$I_{SQ} = I_{c,1}\sin(\phi_1) + I_{c,2}\sin(\phi_2) \quad (3.5)$$

where $\phi_{1,2}$ are the phase differences across the two weak links. These phases have to fulfill the fluxoid quantization through the SC loop:

$$2\pi n = \phi_1 - \phi_2 + 2\pi \frac{\Phi}{\Phi_0} \quad (3.6)$$

where $\Phi_0 = h/2e$ is the superconductive flux quantum and $\Phi = \Phi_e + L_{SQ}I_s$ is the effective magnetic flux through the SC loop. Φ is the sum of the external applied flux Φ_e and the flux generated by the total loop inductance L_{SQ} and screening current I_s . One can substitute the expression for ϕ_1 from Eq. 3.6 into Eq. 3.5, and, by assuming symmetric junctions (i.e. $I_{c,1} = I_{c,2}$) and negligible SQUID inductance $L_{SQ} \simeq 0$, the current of the SQUID can be written as:

$$I_{SQ} = 2I_{c,1}|\cos(\pi \frac{\Phi_e}{\Phi_0})|\sin(\phi) = I_c(\Phi_e)\sin(\phi) \quad (3.7)$$

Thus, a SQUID behaves as a single JJ with critical current I_c which is a function of the magnetic flux through the SQUID loop. I_c has a maximum I_c^{\max} for multiple integer values of Φ_0 , while it modulates down to 0 for half-integer multiples of the flux quanta. Thus the critical current modulation depth is $\Delta I_c = I_c^{\max}$.

For simplicity, Eq. 3.7 has been obtained without considering the inductance of the SQUID loop and weak links. If $L_{SQ} > 0$, this has the effect of screening the applied flux

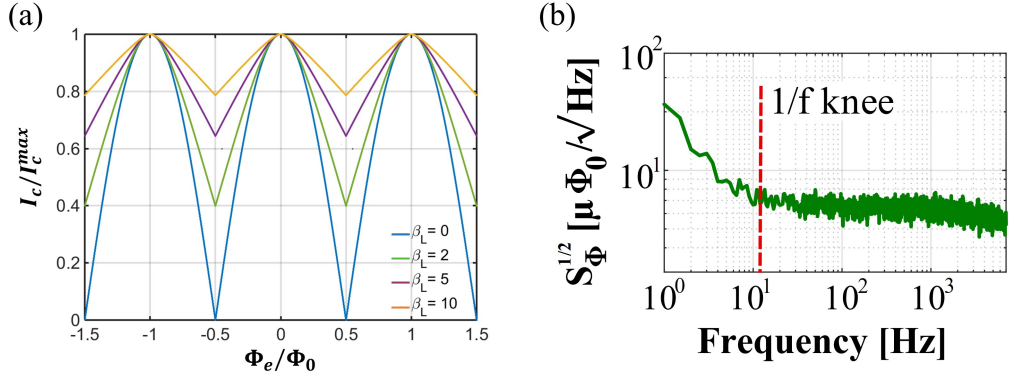


Figure 3.3: (a) Normalized critical current modulation as a function of applied magnetic flux for different values of β_L . (b) Magnetic flux noise of a nanowire-based YBCO SQUID, measured with ac bias reversal at $T = 77$ K. The broken, red line corresponds to the $1/f$ knee.

and decreasing the effective ΔI_c . There is no analytical expression of $I_{\text{SQ}}(\Phi_e)$ when $L_{\text{SQ}} > 0$ and the critical current modulation of the SQUID can be obtained through numerical calculations as shown in [50, 51]. The effect of L_{SQ} can be quantified by the screening parameter $\beta_L = L_{\text{SQ}}I_c^{\text{SQ}}/\Phi_0$. Larger values of β_L imply smaller modulation depth ΔI_c as is shown in Fig. 3.3(a). From numerical simulations one can approximate the relative critical current modulation depth as $\Delta I_c/I_c \simeq 1/(\beta_L + 1)$ [52, 53, 51].

When a dc SQUID is used as flux sensor, it is current biased just above I_c while the voltage drop over the device V is measured. As shown in Fig. 3.2(b), the critical current modulation, due to magnetic flux, results in a sinusoidal voltage signal. The SQUID sensitivity is given by its voltage response to an applied magnetic flux and the working point of the device is the point of maximum sensitivity $V_\Phi = \max(\delta V/\delta\Phi)$, called transfer function. Given the sinusoidal-like voltage response, V_Φ can be approximated as $V_\Phi \simeq \pi\Delta V_{\max}/\Phi_0$, where ΔV_{\max} is the voltage modulation depth at the working point (see Fig. 3.2 (b)). The voltage modulation depth at the working point can also be approximated as $\Delta V_{\max} = \Delta I_c \delta R$, where δR is the value of differential resistance $\delta V/\delta I$ at the working point. Thus, the sensitivity of the SQUID at the working point can be approximated as $V_\Phi \simeq \pi\Delta I_c \delta R/\Phi_0$. Thus, in order to optimize the sensitivity of SQUIDs as flux sensors, one needs to increase the differential resistance δR and the critical current modulation depth ΔI_c .

3.3.1 Noise performances

As for any other sensor, the performance of a SQUID can be quantified in terms of its noise property. Different technological applications usually require different levels of maximum noise. The measured voltage noise spectrum of a SQUID usually consists of two main contributions: flicker, or $1/f$, noise and white noise. The former is predominant at low frequencies and originates from either critical current fluctuations or thermally activated motion of vortices. The effect of I_c fluctuations can be reduced significantly via an ac bias reversal scheme [54, 55]. However, this scheme does not reduce the $1/f$ noise from vortex motion, and to mitigate such effect, special precautions have to be taken, such as active field cancellation [56, 57], flux dams [58] and narrowing of

the structures [59, 60]. In optimized systems, the vortex motion contributions to the 1/f noise can be lower than the critical current fluctuations. This results in 1/f knee usually below 10 Hz at $T = 77$ K, where the 1/f knee is the frequencies above which the flicker noise amplitude becomes lower than the white noise, as shown in Fig. 3.3(b).

The white magnetic flux noise $S_\Phi^{1/2}$ is usually the limiting factor for SQUID sensitivity, dominating the spectra at frequency above the 1/f knee. The minimal intrinsic flux noise of a SQUID can be achieved for $\beta_L \simeq 1$ [61]. $S_\Phi^{1/2}$ is the result of Johnson-Nyquist noise in the JJs, or weak links, plus the input voltage noise of the preamplifier $S_{V,\text{amp}}$. The white magnetic flux noise power spectral density, $S_\Phi^{1/2} = S_V^{1/2}/V_\Phi$, can be written as [62]:

$$S_\Phi^{1/2} \simeq \frac{1}{V_\Phi} \sqrt{\frac{12k_B T}{R_N} \left(\delta R^2 + \frac{(L_{\text{SQ}} V_\Phi)^2}{4} \right) + S_{V,\text{amp}}} \quad (3.8)$$

where δR is the dynamic resistance of the SQUID, defined in the previous section, and R_N is the normal resistance of the single junction. If we take typical values obtained on our SQUIDs (shown in Chapter 5), then we find that $(L_{\text{SQ}} V_\Phi)^2 \ll \delta R^2$. Thus, Eq. 3.8 can be approximated as:

$$S_\Phi^{1/2} \simeq \Phi_0 \sqrt{\frac{12k_B T}{\pi^2 \Delta I_c^2 R_N} + \frac{S_{V,\text{amp}}}{\pi^2 \Delta I_c^2 \delta R^2}} \quad (3.9)$$

hence, to decrease the magnetic flux noise of the SQUID, one needs to maximize the values of ΔI_c , R_N and δR . The last two parameters are tightly connected to each other since a larger junction resistance leads to a larger differential resistance. Since the voltage modulation depth is $\Delta V \simeq \delta R \Delta I_c$, its value gives a good first indication on the performance of a SQUID.

3.4 HTS-based JJs and weak links

LTS-based JJs can be readily fabricated through standard micro- and nanofabrication techniques, e.g. shadow evaporation and lift-off. However, cuprate materials are too complex for physical evaporation and are deposited, by other methods, at temperatures, which are too high for a lift-off process, precluding most of the fabrication techniques used for LTS. Moreover, for a cuprate JJ, the use of metals or other materials as barrier is very difficult due to the small coherence length ξ of the cuprates. In fact, one needs to get atomically clean interfaces since the superconducting order parameter can drop within a few nm (coherence length). Therefore, if the SC-N interface is *dirty* (damaged layer of e.g. YBCO in contact with N) the order parameter can be suppressed at the interface before reaching the normal conductor. The best SC-N interfaces implemented in YBCO- Au-Nb junctions have been achieved by the Twente group, which has led to pioneering experiments on phase sensitive studies of the superconductive order parameter in YBCO [22, 63].

Nevertheless, the technological advantages of HTS pushed the field to go beyond standard techniques and to produce alternative solutions for the fabrication of HTS-based JJs and weak links. In the following, we summarize some of the most prominent types of JJs and weak links which have been successfully implemented for YBCO:

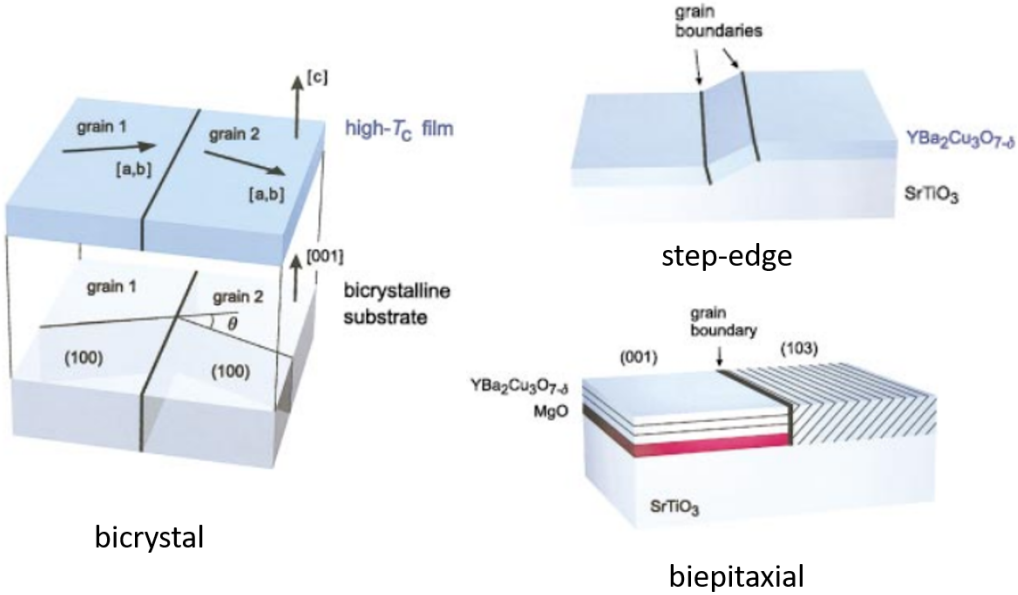


Figure 3.4: Schematic of grain boundary junctions. (Adapted from [64])

- **Grain Boundary:** A grain boundary (GB) is a highly disordered region, which forms at the interface between grains with different crystallographic orientation. This interface has strongly suppressed superconducting properties and can be used as the weak link or barrier in the fabrication of YBCO JJs [64]. There are different methods to obtain GB junctions: 1) *bicrystal*[65]: YBCO is epitaxially grown on a substrate, which is obtained by bonding together two crystals of the same material with different relative crystallographic orientation (bicrystal). During the thin film deposition, the YBCO grows with different crystallographic orientations on the two sides of the bicrystal (see Fig. 3.4, left panel). A GB is formed along the interface between the two YBCO films grown with different relative crystallographic orientations. The angle between the two orientation can be changed to tune the properties of the GB. 2) *step-edge*[66]: the substrate is etched to create a sloped step. For appropriate values of angle between substrate surface and step, YBCO can grow with a different crystallographic orientation on the surface of the step. A GB forms at the upper and lower edges of the step (see Fig. 3.4, top right panel). 3) *bi epitaxial*[67]: An epitaxially grown seed layer is patterned on top of the substrate. This layer is chosen to change the epitaxial growth orientation of YBCO over it and a GB is formed at the interface between the YBCO grown directly on the substrate and on the seed layer (see Fig. 3.4, bottom right panel).

GB-based JJs are the state-of-the-art technology for the fabrication of high quality YBCO JJs [68, 69]. However, this technique has some drawbacks: the number of fabrication steps and cost of production for step-edge are higher compared to other fabrication methods. The fixed position of the GB in bicrystals limits the flexibility in design of the final device. The presence of inhomogeneity along the GB line which are hard to control, might result in low reproducibility of GB-JJs

[70].

- **Ion irradiated:** YBCO is locally damaged by exposing the material to an highly energetic ion beam to create a region of suppressed superconductivity. The SC properties of YBCO can be tuned by changing the irradiation dose, thus changing the induced disorder and driving the material from SC to insulator [71, 72]. To limit the area of damage, YBCO can be protected with a mask which has openings to let the ions through locally [73, 74, 75]. However, the best result have been obtained with the Focused Ion Beam (FIB) technique [72, 76, 70, 77]. Here, the flow of ions is focused into an extremely narrow beam which can be controlled to *write* over the sample. This does not require the use of a mask and, since the beam can be focused to a diameter of 0.5 nm (for He ions), extremely narrow areas can be exposed. This technique has the advantage of being more tunable than the GB technology. Moreover, SIS and SNS JJs can be achieved by tuning the FIB dose [72, 70]. One can use the FIB to create a weak link along a pre-patterned wire [72, 70], introducing an extra fabrication step. Alternatively, the entire sample can be defined via FIB [77]. However, while this technique is very flexible, the time required to expose large areas is very long due to the small beam spot. Moreover, the best results reported in literature have been achieved at temperatures below 77 K, limiting technological applications.
- **Dayem nanobridges (nanowires):** YBCO weak links can be fabricated in the form of nanobridges, named Dayem bridges [78], by laterally narrowing down a section of a thin film, as shown in Fig. 3.5 (see also Appendix A). The resulting bridge has the same thickness as the thin film. Thanks to improvement of the nanofabrication, nanobridges with cross-section of $50 \times 50 \text{ nm}^2$ and pristine (bulk-like) SC properties have been achieved [79]. YBCO nanobridges have shown high values of critical current density, j_c . While this technology might be ideal for HTS single photon detector applications [80], SQUIDs based on nanobridges showed lower performance, i.e. higher flux noise values, especially at $T = 77 \text{ K}$, compared to GB-based devices. However, the fabrication procedure for nanobridges require less steps than for step-edge and ion-irradiated JJs, and the wire can be defined anywhere on the sample, in contrast to bicrystal-GB JJs. Moreover, Dayem nanobridges have shown high reproducibility, with spread of the measured critical current density around 10% at $T = 4.2 \text{ K}$ [79].

These are the main types of JJs and weak links which have been achieved with YBCO, however, in some cases two or more of these techniques can be combined. For example, FIB has been used to reduce the lateral size of GB junctions, resulting in ultra-low noise SQUIDs at $T = 4.2 \text{ K}$ [81, 82]. The work presented in this thesis will focus on the study of nanowires, their applications and the improvement of nanowire-based SQUID performance.

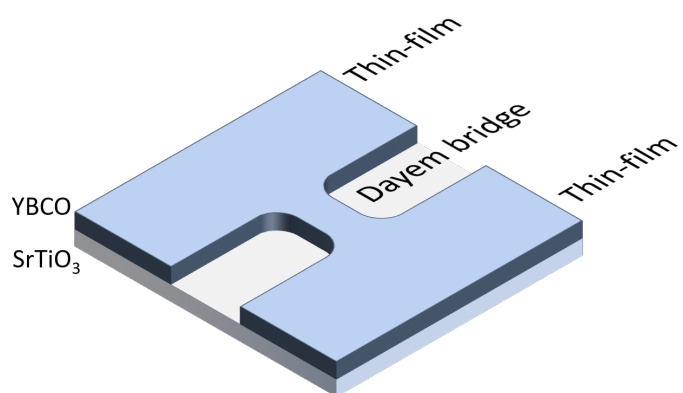


Figure 3.5: Sketch of a YBCO Dayem bridge, on a STO substrate.

3. HTS-based devices

CHAPTER 4

Nanowire-based SQUIDs

Nanowires can be used to study the physics of HTS materials, as well as to realize HTS-based devices, and, in both cases, the quality of the weak links has to be preserved during fabrication. The challenge in realizing a high quality YBCO nanowire stems from the chemical instability of the material, i.e. the out-diffusion of oxygen, combined with a high sensitivity of YBCO to disorder. The first sub-micron YBCO wires showing SC behavior, i.e. $I_c > 0$, at $T > 77$ K were reported in the first half of the 1990s [83, 84, 85, 86]. However, these nanowires showed suppressed SC properties compared to bare films, suggesting the YBCO quality was degraded during the fabrication. The lower quality of these nanowires was reflected in the performance of the first YBCO nanowire-based SQUIDs [87, 88], which showed low values of SQUID voltage modulation amplitude, ΔV_{\max} , ($< 10 \mu\text{V}$) and high flux noise ($> 50 \mu\Phi_0/\sqrt{\text{Hz}}$) at $T \simeq 77$ K.

In later years, the quality of YBCO nanowires has increased drastically thanks to the improvement of the fabrication process. Indeed, in the first half of 2010s the optimization of a process to fabricate Au capped nanowires developed in our group allowed to reach cross sections down to $50 \times 50 \text{ nm}^2$ [89, 79, 90] with pristine superconducting properties. The nanofabrication process for YBCO used in this thesis, see Appendix A, is based on the process presented in [89, 79], although without the implementation of a Au capping layer [91]. The first Au capped nanowires demonstrated critical current values close to the theoretical depairing limit, an indication of the pristine quality of the nanowires [79, 90]. The high quality of the YBCO nanowires paved the way for technological applications such as single photon detectors [80] and nanoSQUIDs [8, 92, 93]. Here, nanoSQUID refers to a SQUID with nanoscale weak links and loop sizes in the sub- μm scale, aimed at reducing L_{SQ} . The fabrication process presented in Appendix A allows to easily integrate the nanowires in a sub- μm scale loops to obtain a nanoSQUID[8, 93]. Such devices demonstrated white magnetic flux noise as low as $1 \mu\Phi_0/\sqrt{\text{Hz}}$ at $T = 8$ K [8].

Nanowire-based nanoSQUIDs represent an ideal platform for studying magnetic nanoparticles in a wide range of temperature and at moderate/high magnetic fields [94]. The performance of nanowire based nanoSQUIDs is further improved when no Au capping layer is implemented and reducing the YBCO film thickness (from 50 nm, down to 10 nm). In fact, nanowires without the Au capping layer showed differential resistance values, δR , almost 10 times higher than their capped counterparts. Reducing the thickness from 50 nm to 10 nm, results in an additional factor 8 increase of δR and further reduction of $S_\Phi^{1/2}$. The white magnetic flux noise measured on a nanoSQUID implementing nanowires with $10 \text{ nm} \times 75 \text{ nm}$ cross-section and without Au capping layer, was as low as $450 \text{ n}\Phi/\sqrt{\text{Hz}}$ above 100 kHz at $T = 18 \text{ K}$ [93]. This noise level is more than a factor 2 lower compared to previous results obtained on Au capped 50 nm thick YBCO nanoSQUIDs [8].

The performance of nanoSQUIDs with ultra-thin nanowires show the potential of this devices for technological applications, although it also highlights the intrinsic limitations of nanowires. In fact, considering the values of δR and Eq. 3.9, one would expect almost a factor 10 reduction of the nanoSQUID intrinsic noise contribution to the flux noise, plus a further reduction of the amplifier input noise contribution. However, the reported white magnetic flux noise is not as low as it would be expected by only considering the increase of δR . The reason is that, when reducing the YBCO thickness, the performance is limited by the increased kinetic inductance. A higher parasitic inductance of the nanowires contributes to a significant increase of the SQUID inductance, L_{SQ} , and the performance of the nanoSQUIDs will be limited by the resulting small values of ΔI_c . The inductance of a nanowire has a geometric (related to the magnetic field generated by the current) and a kinetic contribution (related to the inertia of the charge carriers). However, the former is negligible compared to the latter in narrow nanowires $wt < \lambda^2$ [95], where w and t are the width and thickness of the nanowire, respectively (see Fig. 4.1). The kinetic inductance per unit length of a nanowire, L_{kin} , is given by[96]:

$$L_{\text{kin}} = \frac{\mu_0 \lambda}{w} \coth\left(\frac{t}{\lambda}\right) \quad (4.1)$$

where w and t is the width and thickness of the nanowire, respectively, and μ_0 is the vacuum permeability. The kinetic inductance of a thin ($wt < \lambda^2$) nanowire with length l can then be approximated as

$$L_{\text{kin}} = \frac{\mu_0 \lambda^2 l}{wt} \quad (4.2)$$

Therefore, for smaller cross sections, the parasitic inductance of nanowires might have a non-negligible contribution to L_{SQ} .

In general, the performance of nanowire based SQUIDs can be limited by three main factors: low δR , large I_c and large L_{SQ} . The latter could be reduced with smaller SQUID loops, however this would be detrimental for SQUID magnetometer applications which require large magnetic areas and therefore a sizable SQUID loop inductance, as will be shown in details in section 5.4. If one assumes that $\delta R \propto l/(wt)$ and $I_c \propto wt$, it is clear that the wire dimensions which optimizes δR , e.g. small wt and large l , result in increased L_{kin} . Therefore, there is a trade-off when optimizing nanowire

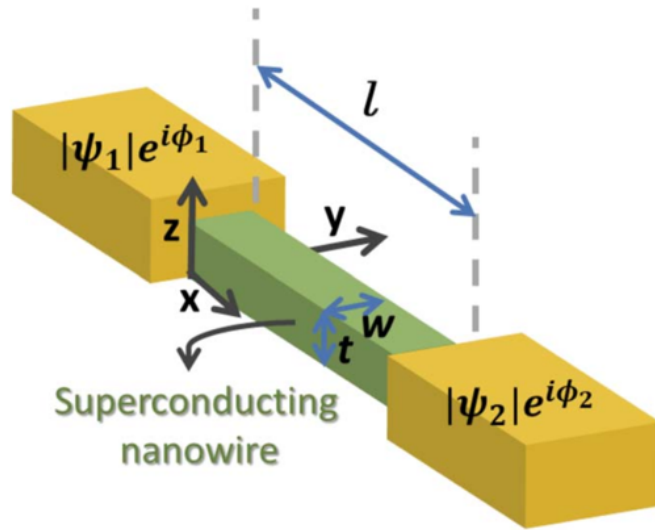


Figure 4.1: Schematic of a superconducting nanowire where the main dimensions are defined. (adapted from [95])

based SQUIDs which sets a limit to the performance, which can be achieved. Optimally doped YBCO nanowires generally have a large critical current density, $j_c \simeq 3 \text{ MA/cm}^2$, at 77 K [79, 8]. This, together with the parasitic kinetic inductance, sets a lower bound for the screening factor, $2I_c L_{\text{kin}}/\Phi_0 = 4j_c L \mu_0 \lambda^2/\Phi_0$ on the order of 1-3 at 77 K for a typical bridge length $l = 150 \text{ nm}$. [8] This limit has been calculated based solely on the parasitic inductance of nanowires, and given the additional contribution of the SQUID loop, the value of the total SQUID screening parameter, β_L , is further increased.

Low magnetic flux [8] and field [9] noise in nanowire based YBCO SQUIDs have been achieved at low temperatures ($T < 18 \text{ K}$). However, nanowire based SQUIDs and magnetometers showed noise levels at least one order of magnitude higher than GB-based devices at $T = 77 \text{ K}$ [10]. To go beyond the limitations of nanowires, we developed a novel type of weak link, the grooved dayem bridge (GDB). As the name suggests, a GDB is an alternative take on the standard Dayem bridge (nanowire), where a groove is etched into the nanostructure to locally suppress superconductivity. As will be shown in detail in chapter 5, these novel weak links overcome the low differential resistance and large parasitic inductance of bare nanowire, resulting in SQUID sensitivities at par with state-of-the-art GB-based devices.

4.1 Nanowires

As introduced in Section 3.4, an effect similar to the Josephson effect can be observed also when two SCs are coupled through another SC instead of a barrier. In the case of weak links, e.g. nanowires, a section of SC with suppressed superconductive properties or reduced dimensions substitute the barrier. The Josephson effect in the case of short one-dimensional structures was predicted soon after the discovery of JJs [97]. However, the critical current and the current phase relation of nanowires may change when departing from the short one-dimensional limit. Indeed, depending on the nanowire di-

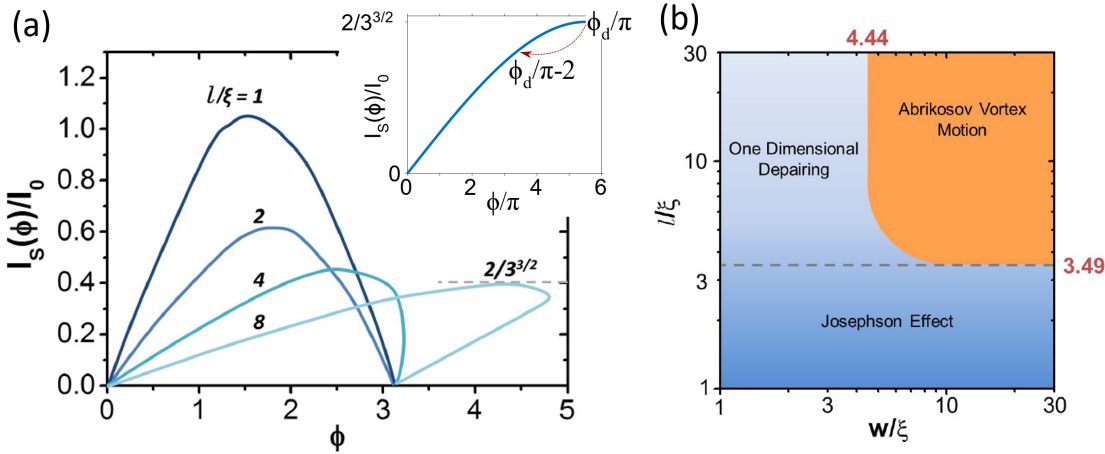


Figure 4.2: (a) Normalized current phase relation of a long one-dimensional weak link for increasing values of the ratio l/ξ . Here $I_0 = w * t * j_0^{\text{AL}}$. The inset shows the positive branch of the CPR of a nanowire in the depairing limit ($l = 30\xi$). Here, the arrow at ϕ_d refers to a phase slip event. (adapted from [98]) (b) Criteria for the origin of the CPR of nanowires with different geometries. (adapted from [99])

mensions, different regimes can be identified. In the following, we will give an overview of the properties of nanowires with different dimensions, i.e. width, w , length, l , and thickness, t , as shown in Fig. 4.1:

- **Short one-dimensional wires:** When two bulk SCs are separated by a short ($l \ll \xi$) one-dimensional ($w, t \ll \xi$) SC, the critical current density can be expressed as [97]:

$$j_s^{\text{AL}} = \frac{\Phi_0}{2\pi\mu_0\lambda^2\xi} \sin\phi \quad (4.3)$$

In this regime the CPR is strictly sinusoidal, as for standard JJs, see Eq. 3.1. In this limit, the critical current density of the weak link is given by eq. 4.3 as $j_0^{\text{AL}} = \Phi_0/2\pi\mu_0\lambda^2\xi$. Since ξ is a function of temperature and its value diverges for T close to T_c , most weak links enter the short one-dimensional limit when T is close to the critical temperature, thus showing a sinusoidal CPR. Since the coherence length, ξ , of HTS is extremely small ($\xi_{a,b} \simeq 2$ nm), short one-dimensional HTS weak links can be achieved only for $T \simeq T_c$. When the width of short nanowires ($l < 3.49\xi$) is increased, the weak link is still expected to show standard Josephson effect (single valued CPR). As for the one-dimensional case, this regime has been exhaustively studied for LTS [100], but cannot be accessed with HTS due to the small ξ .

- **Long one-dimensional wires:** If the length of a wire is increased, the CPR departs from purely sinusoidal behavior and becomes increasingly more a *slanted* sinusoidal for increasing ratio l/ξ , eventually becoming multivalued for $l > 3.49\xi$ [98]. In Fig. 4.2(a) we show the evolution of the weak link CPR for increasing values of l/ξ , while the different regimes of a nanowire weak link are shown schematically in Fig. 4.2(b). For $l \leq 3.49\xi$, the weak link behaves according to the classic Josephson effect and the CPR is single valued, although the critical current decreases for longer wires. When $l > 3.49\xi$, the CPR becomes multival-

ued and the weak link starts transitioning to a regime where the critical current is limited by the one dimensional depairing effect. Here, the value of critical current keeps decreasing for longer wires and, for $l > 10\xi$, it saturates to the depairing critical current $I_d = 2I_0/3\sqrt{3}$, where $I_0 = wtj_0^{\text{AL}}$ is the critical current of short one-dimensional wires. In the one dimensional depairing regime, if the phase difference, ϕ , is increased above its critical value (see below), the order parameter can be temporarily and locally suppressed in a small portion of the wire. This area becomes the center for the nucleation of phase slips: when $|\Psi| = 0$, the phase difference is unrestricted and it can *slip*, i.e. have a sudden change of value [15]. Since the phase needs to be single valued, ϕ can only slip by 2π , or a multiple integer of it. A phase slip results in a finite voltage drop.

In the limit $l > 3.49\xi$, the stable branch of the CPR, shown in inset of Fig. 4.2(a), which was derived by Likharev and Yakobson [98], can be expressed as:

$$j_s^{\text{LY}} = \frac{\Phi_0}{2\pi\mu_0\xi\lambda^2} \left[\frac{\xi}{l}\phi - \left(\frac{\xi}{l}\phi \right)^3 \right] \quad (4.4)$$

To find the maximum phase gradient before a phase slip occurs, ϕ_d , one needs to maximize this equation with respect to the phase gradient, obtaining $\phi_d = l/\sqrt{3}\xi$. Substituting ϕ with ϕ_d in Eq. 4.4, one obtains the expression for the depairing critical current density:

$$j_d = \frac{\Phi_0}{3\sqrt{3}\pi\mu_0\lambda^2\xi} \quad (4.5)$$

For standard JJs, the CPR is purely sinusoidal and it is fully described in the interval $-\pi < \phi < \pi$. The corresponding interval for long nanowires ($l \gg \xi$) is $-\phi_d < \phi < \phi_d$, which is significantly larger than that for the sinusoidal case. For $\phi \ll \phi_d$, the cubic term in Eq. 4.4 can be neglected and the phase increases linearly with the current as

$$I = \frac{wt}{\mu_0\lambda^2 l} \frac{\Phi_0}{2\pi} \phi = \frac{\Phi_0}{2\pi L_{\text{kin}}} \phi \quad (4.6)$$

Here, we obtained the same expression for $L_{\text{kin}} = \mu_0\lambda^2 l/wt$ as from eq. 4.2. Therefore, in this limit the weak link behaves as a linear inductance.

- **Long wires with increasing width:** For long nanowires ($l > 3.49\xi$), if w is increased above 4.44ξ , the phenomenon which determines I_c transitions from the one-dimensional depairing effect to the entry of Abrikosov vortices into the wire [99, 101], see Fig. 4.2(b). Here, a fluxon may enter the nanowire by overcoming the so-called Bean-Livingston barrier [102], i.e. the finite edge barrier, which normally prevents vortices from entering the bridge. Increasing the supercurrent flowing in the nanowire, I_s , gradually reduces the edge barrier. When I_s approaches the critical current, the barrier is completely suppressed at the edges of the wire over a distance ξ . This allows the nucleation of Abrikosov vortices; their motion, due to the Lorentz force, results in a finite voltage drop. In this regime, the critical current can be calculated by considering the phase difference, ϕ_v , at which the vortices start to nucleate. In the limit $t < \lambda$ and $w < \lambda_P = \lambda^2/t$, which is usually

true for YBCO nanowires ($\lambda \geq 200$ nm), Bulaevskii et al. [103] showed that this phase difference corresponds to $\phi_v = l/2.718\xi \simeq 0.64\phi_d$. Therefore, the critical current density due to Abrikosov vortex motion is $j_v \simeq 0.826j_d$.

Since $t < \lambda$ and $w < \lambda_P = \lambda^2/t$, the current density can be considered homogeneous over the weak link. Thus, the nanowire can still be approximated as one-dimensional [103, 104] and the CPR has the same multivalued form given by Eq. 4.4.

CHAPTER 5

Properties and performances of GDB-based devices

Grooved Dayem nanobridges (GDB) represent a new concept for the fabrication of high quality YBCO weak links [105, 106, 107]. Thanks to enhanced electrical properties, GDB overcomes most of the limitations of bare nanowires presented in the previous chapter, i.e. low δR , large I_c and large parasitic (kinetic) inductance L_{kin} . In this chapter, we will first present the fabrication procedure to obtain GDBs in comparison to the standard nanowire fabrication. Thereafter, the electrical properties of this novel weak link are studied as a function of geometry to find the optimal configuration. From the temperature dependence of the electrical properties of GDB based SQUIDs (I_c , ΔV , δR) we conclude that at low temperatures the GDBs behave like short Dayem bridges whereas at temperatures above $T \simeq 60$ K the weak links behave like SNS junctions. GDB are furthermore employed in SQUID-based magnetometers, resulting in improved noise properties as compared to nanowire-based devices and magnetic field noise values comparable to the state-of-the-art are obtained. Finally, future considerations to further improve GDBs are presented, with some preliminary but promising result.

5.1 Fabrication

A Grooved Dayem nanobridge consists of a standard nanowire with a small groove etched along its width in the middle of the bridge. The YBCO films are grown by pulsed laser deposition (PLD) on (001) SrTiO₃ (STO) substrates, and have thickness $t_{\text{YBCO}} = 50$ nm. The fabrication procedure to obtain a GDB follows directly from the one used for nanowires, which is reported in Appendix A. The main difference is the design of the etching mask, which makes use of the particular etching dynamic inside a nanogap to reduce the etching rate and results in a groove in the nanowire. Nevertheless, the same fabrication steps used for nanowires are also used for GDB, thus maintaining the fabrication advantages compared to other weak links and JJs

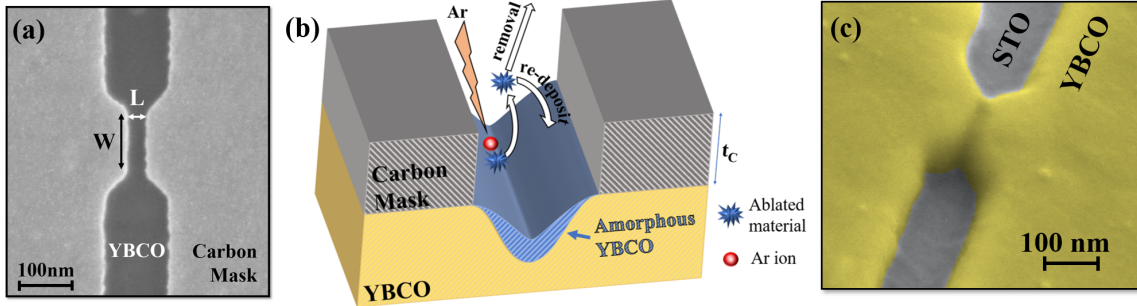


Figure 5.1: (a) SEM image of the etching mask for GDB with relevant dimension parameters. (b) Schematic process of the Ar⁺ ion etching inside the mask gap. (c) SEM image of a GDB after fabrication. The shallow etching of the groove can be seen in the middle of the nanobridge.

technologies presented in section 3.4.

Starting with the fabrication procedure reported in Appendix A, which is based on the work done in Ref. [89, 79, 92], the key difference with the GDB fabrication process is a small gap in the Carbon mask which is designed perpendicular to the nanobridge direction. An example is shown in Fig. 5.1(a), where the relevant mask parameters are also indicated. The gap is designed with width W corresponding to the width of the nanobridge and the gap length L , which can be varied. However, the ratio of L and carbon mask thickness $t_C \simeq 100$ nm (see Fig. 5.1(b) and Appendix A) is crucial to determine the outcome of the Ar⁺ ion milling process. In fact, the effective etching rate of the material inside the gap can be varied, with respect to the rest of the sample, depending on the value of t_C/L [108].

In a physical etching process, the target material is hit with highly energetic particles, in our case these are Ar⁺ ions. These accelerated particles ablate material from the target, which can then be completely removed, i.e. fly off, or re-deposit on the surface. In standard processes, the rate of re-deposition is much lower than the rate of removal and it does not influence strongly the etching rate. However, the re-deposition rate increases if some of the ablated clusters cannot be removed, e.g. due to physical constrictions. Indeed, when etching inside a narrow gap, the re-deposition rate increases drastically when the thickness of the mask is comparable or larger than twice the gap length L [108] (i.e. $t_C/L \gtrsim 2$). A schematic of the etching process inside a nanogap is shown in Fig. 5.1(b). The re-deposition of material leads to a reduction of the effective etching rate inside the mask gap compared to other areas of the samples. Given a fixed value of mask thickness t_C , which in our case is $t_C = 100$ nm, the effective etching rate will depend on the gap length L : if $t_C/L < 2$, the re-deposition is reduced and the etching rate is increased; vice versa, for $t_C/L > 2$, less material is removed from the nanogap and the etching rate is strongly reduced. The etching mask is designed so that the ratio $t_C/L \simeq 2$ is valid only inside the mask gap, elsewhere the mask features are comparable to or larger than t_C . Hence, the etching rate is reduced only inside the gap, while the rest of the YBCO film is etched at a higher rate. This allows to etch the sample and the groove feature during the same Ar⁺ ion milling step: the time required to etch through the YBCO film results in only partial etching inside the nanogap. This allows to keep the same fabrication steps used for nanowires, without complicating the

process.

The final result is a nanobridge with a groove etched in the center. A Scanning electron microscope (SEM) image of a GDB is shown in Fig. 5.1(c). Here, the YBCO film is completely etched to obtain the designed nanobridge and electrodes, while a shallow groove can be seen in the center of the structure. The GDB in Fig. 5.1(c) is obtained with the etching mask shown in panel (a) of the same figure, which has dimensions $W = 200$ nm and $L = 50$ nm. After fabrication, the thickness of the pristine YBCO (not considering the amorphous re-deposited material) inside the groove is t_{GDB} , see Fig. 5.1. (b), which is a function of the effective etching rate inside the gap, and thus of the gap length L (the Carbon thickness is kept constant at $t_{\text{C}} = 100$ nm). The groove acts as the weak link reducing locally the superconducting properties of the nanowire. This type of weak link is akin to a variable thickness bridge [109, 100], where a central section of the structure has reduced geometrical dimensions. Moreover, in a GDB the superconducting properties of the groove could be locally reduced due to damage to the material during Ar^+ ion milling. The properties of the GDBs can be expected to depend strongly on the groove thickness t_{GDB} and thus on the gap length L . It is then crucial to tune the etching mask design (W and L) to optimize the depth of the groove and hence the electrical properties of the GDB.

5.2 Electrical properties of single GDB

Following the fabrication introduced above, in this chapter we investigate the electrical properties of GDBs as a function of etching mask geometry. We aim at optimizing the electrical properties of GDBs with working temperature $T = 77$ K for HTS applications which work at LN_2 temperature. Both width W and length L of the nanogap can be expected to play an important role for the electrical properties of a GDB. Since SQUIDs are the main target application for this weak link, the objective is to find the optimal geometric parameters, which would overcome the limitations of bare nanowires. First considering the kinetic inductance, L_k from Eq. 4.1, which is inversely proportional to the width of the weak link W , wider structures would result in a reduction of the parasitic kinetic inductance L_k . For bare nanowires, increasing W leads to an increased I_c , which is detrimental for maintaining $\beta_L \simeq 1$ [61]. However, for a GDB, I_c can be expected to be directly proportional to t_{GDB} and, therefore, inversely proportional to the gap length L , so wider structures with low I_c can be obtained by increasing L . Finally, the differential resistance $\delta V/\delta I$ should be maximized to increase the SQUID voltage response to an applied magnetic flux. To find the optimal geometric parameters, GDBs with different values of length L and width W have been fabricated and characterized at $T = 77$ K.

When designing the etching mask, one needs to consider the minimal feature sizes which can be achieved with electron beam lithography (EBL). In fact, it is challenging to expose nanogaps with length $L \leq 20$ nm. With such a small gap, the exposed mask is not reproducible and might result in shorts, or connections, between the nanogap banks. This sets a lower limit for the nanogap length $L_{\min} \simeq 30$ nm in order to obtain reproducible GDBs. Fortunately, this is not too restrictive since, as will be shown below, to achieve a proper reduction of I_c the gap length has to be $L \geq 40$ nm. On

the other hand, the EBL sets a limit also for the maximum achievable W . In fact, the mask exposure becomes increasingly more challenging for wider nanogaps (increased W). Indeed, GDB fabricated with $W \geq 250$ nm, do not show consistently a reduction of I_c as compared to bare nanobridges having the same width and thickness, even for longer gaps $L = 60 - 70$ nm. During the EBL, higher values of W can reduce the fidelity of the exposed mask, resulting in connections between the two sides of the gap or inhomogeneous gap length across the gap. Therefore, while W should be maximized to reduce L_k , we have an upper limit for the achievable width $W_{\max} \simeq 200$ nm.

While the EBL sets the limits W_{\max} and L_{\min} , also the effects of the Ar^+ ion milling reduce the useful range of W and L . When the width is reduced to $W = 100$ nm, the GDBs fabricated with $L = 30 - 50$ nm show rather large deviation of the electrical properties among nominally identical devices. Here, some of the best devices show low I_c ($< 100 \mu\text{A}$) and high differential resistance ($\delta V/\delta I > 15 \Omega$) at $T = 77$ K. Unfortunately, the non-reproducible electrical properties make GDBs with $W \leq 100$ nm not suitable for technological applications. Moreover, for $W = 100$ nm, if L is further increased ($L \geq 60$ nm), no I_c can be measured at $T = 77$ K, i.e. the SC properties are completely suppressed. This indicates that the damage to the structures during the Ar^+ ion milling plays a role in the final properties of the GDB. This becomes more prominent when the nanogap width approaches 100 nm, setting the lower limit for the GDB width at $W_{\min} = 100$ nm.

Therefore, the optimal range for the nanogap width is $W = 150 - 200$ nm, as will be shown below. This leads to the best results in terms of electrical properties and reproducible values of I_c . However, the nanogap length L still needs to be optimized for this optimal range of W . GDBs fabricated with $W = 150 - 200$ nm and $L > 60$ nm generally do not exhibit any superconducting behavior and are resistive at $T = 77$ K. On the other hand, if L is reduced below 40 nm, the groove is too shallow ($t_{\text{GDB}} \simeq t_{\text{YBCO}}$, where t_{YBCO} is the thickness of the YBCO thin-film) and the weak links show values of I_c close to bare nanobridges. Thus, the best GDBs can be achieved for $L = 40 - 60$ nm.

We carried out an extensive study with GDBs fabricated with $W = 200$ nm and L ranging from 40 nm to 60 nm. The average values of I_c measured at $T = 77$ K extracted as a function of nanogap length are shown in Fig. 5.2. Here, the value of I_c decreases rapidly when L is increased. This is expected since a longer gap results in higher etching rate inside the groove, hence lower value of t_{GDB} . The standard deviations of the measured I_c are rather small, indicating that the fabrication procedure

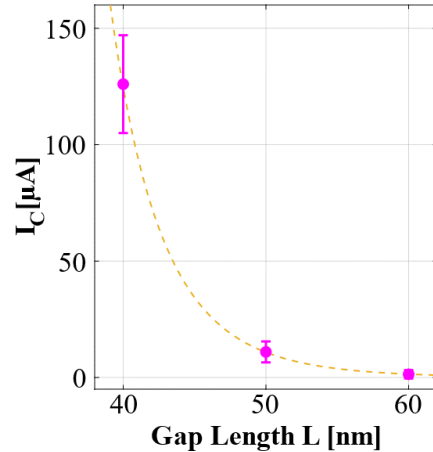


Figure 5.2: Average I_c as a function of gap length L . The GDBs have $W = 200$ nm, the total amount of measured devices fabricated on 9 different chips are 28, 56, and 16 for $L = 40$, 50, and 60 nm, respectively. The dashed line represents a power law dependence and is intended as a guide for the eye. (adapted from [105])

Fig. 5.3 IVC & $\delta V/\delta I$	L [nm]	W [nm]	I_c [μA]	R_N [Ω]	$I_c R_N$ [μV]
(b) & (d)	40	200	110	5	550
(a) & (c)	50	200	10	20	200

Table 5.1: Summary of the electrical properties extracted from the data presented in Fig. 5.3 for GDBs with $W = 200$ nm and $L = 40 - 50$ nm at $T = 77$ K. These GDBs were fabricated with $t_{\text{YBCO}} = 50$ nm and $t_{\text{C}} = 100$ nm.

is well reproducible. The measured I_c are within $\sim 15\%$ of the average value, which is only slightly worse than the best results obtained on Au capped YBCO nanowires. From this measurements, we can exclude $L = 60$ nm and select the values of 40 nm and 50 nm as the optimal nanogap length for $W = 200$ nm at $T = 77$ K.

The Current-Voltage Characteristics (IVCs) at $T = 77$ K for two GDB with $W = 200$ nm and $L = 50$ nm and 40 nm are shown in Fig. 5.3(a) and (b), respectively. The behavior of these two weak links is representative for most of the measured GDB IVCs. From these data we can extract the values $I_c = 110 \mu\text{A}$ for $L = 40$ nm and $I_c = 10 \mu\text{A}$ for $L = 50$ nm. Those are respectively a factor 5 and 50 lower than a bare nanowire with similar width (assuming critical current density $J_c = 5 \times 10^6 \text{ A/cm}^2$ for nanowires with $W = 200$ nm at $T = 77$ K [110]). An interesting feature of the IVCs is their shape: it differs from the power law increase of voltage with applied bias current I_b , which we typically observe in our bare nanobridges at $T = 77$ K and $I_b > I_c$. The IVCs of GDB show a trend which resembles the one expected for Resistively Shunted Junctions (RSJ) (see Fig. 3.1(b)), similarly to JJs defined with FIB [72], and indicative of a SNS-type weak link. This behavior can be seen also in the differential resistance $\delta V/\delta I$ as a function of bias current, shown in Fig. 5.3(c) and (d) for $L = 40$ nm and 50 nm, respectively. These curves can be compared to the $\delta V/\delta I$ versus I_b of a RSJ (see Fig. 3.1(c)). Indeed, the differential resistance of GDBs show narrow peaks for I_b slightly above I_c . However, in contrast with RSJ, the differential resistance does not converge to a constant value of R_N for high I_b . Instead, $\delta V/\delta I$ keeps increasing almost linearly with increasing I_b , which could be an indication of a flux-flow regime or possibly heating effects.

To compare the electrical properties of weak links, we can use the *characteristic voltage*, which is defined as $I_c R_N$. This is a figure of merit for a JJ and higher values of $I_c R_N$ are generally associated with better device performances. However, the IVCs of the GDBs do not converge to a constant resistance value at high bias current, hence R_N cannot be extracted. As an approximation for the value of R_N in GDB, we select therefore the value of $\delta V/\delta I$ in the voltage range $V = 100 - 200 \mu\text{V}$. A summary of the electrical properties for the GDBs from Fig. 5.3 is reported in Table 5.1.

The GDBs presented here have characteristic voltages in the range $I_c R_N = 200 - 550 \mu\text{V}$. These values are almost an order of magnitude higher than for He ion irradiated JJs and bare nanowires at $T = 77$ K [72, 10]. The highest $I_c R_N$ values in YBCO junctions have been achieved for GB-based JJs [68, 69] with values in the range $800 - 1200 \mu\text{V}$. While the best characteristic voltages of our GDBs have values close to this range, GB-based JJs are usually SIS-type junctions, which are characterized by higher $I_c R_N$ values as compared to their SNS counterparts. Nevertheless, as it will

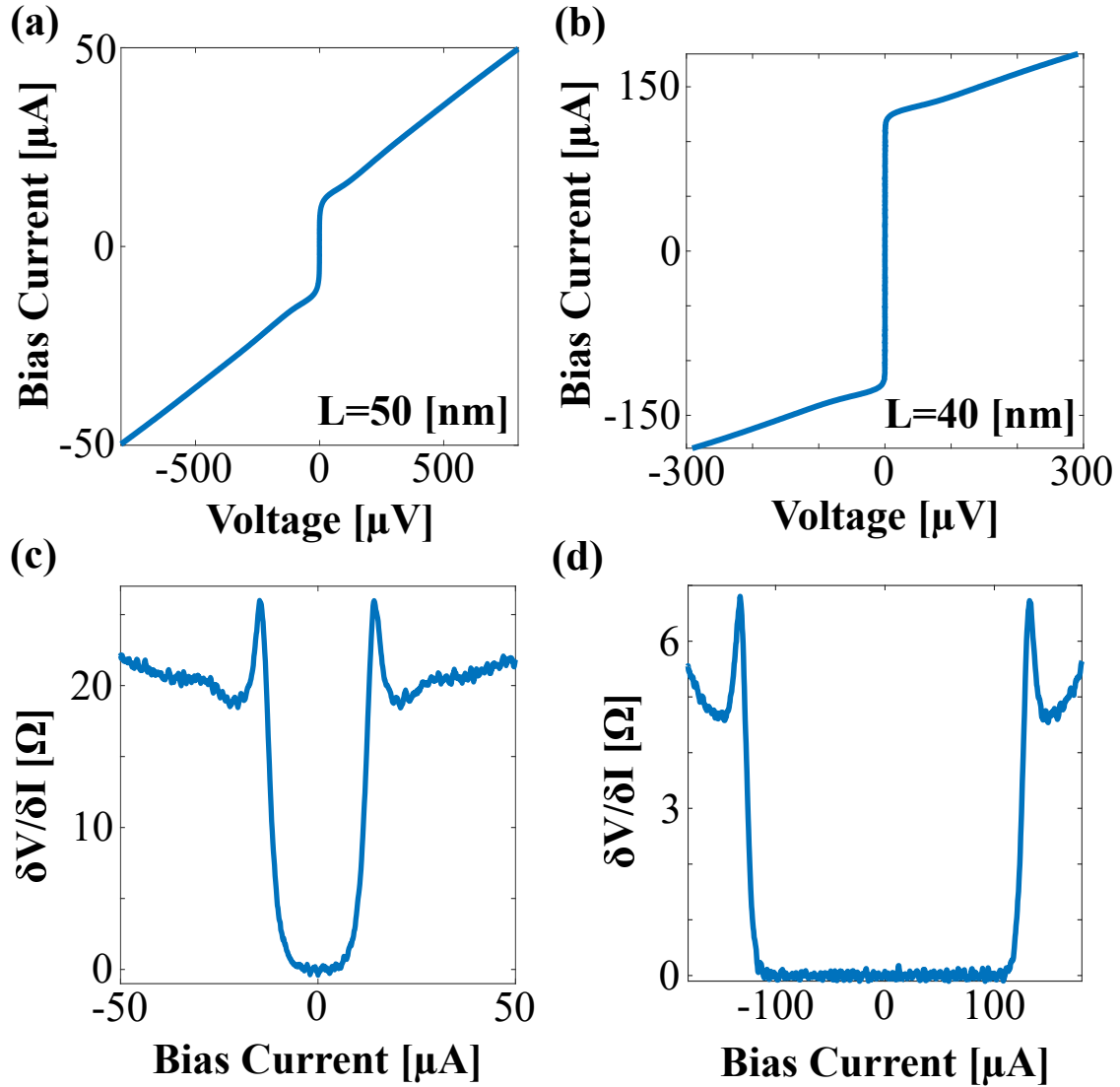


Figure 5.3: (a)-(b) Current voltage characteristics (IVCs) measured at $T = 77 \text{ K}$ for two GDBs with $W = 200 \text{ nm}$ and $L = 50 \text{ nm}$ and $L = 40 \text{ nm}$, respectively. (c)-(d) $\delta V/\delta I$ calculated from the IVCs presented in panel (a) and (b) respectively.

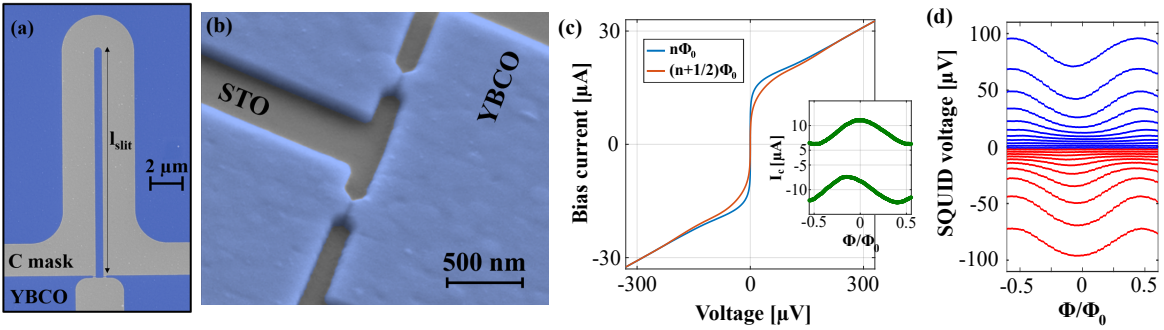


Figure 5.4: (a) Hairpin loop etching mask. (b) SEM image in false color of a GDB-based SQUID (device SQ1). (c) IVCs of SQ1 for two different values of applied magnetic field. Inset shows the critical current modulation as a function of normalized magnetic flux. (d) SQUID voltage modulations of SQ1 as a function of normalized magnetic flux measured for increasing values of I_b with 1.8 μA steps. (adapted from [105])

be shown later in this chapter, the properties of GDBs result in SQUIDs with performances comparable to state-of-the-art GB-based devices, even though they have lower characteristic voltages.

From the above discussion, we conclude that for GDBs with $W = 200$ nm the optimal value of L at 77 K is 50 nm, since it yields lower I_c and higher $\delta V/\delta I$ as compared to the $L = 40$ nm devices. While the GDB with $L = 40$ nm has higher value of $I_c R_N$, it is more important for SQUID application to reduce I_c (lower screening parameter β_L) and increase $\delta V/\delta I$. Hence, the electrical properties of GDBs with $W = 200$ nm and $L = 50$ nm are the most suitable to boost the performance of SQUIDs. These GDBs have critical current values roughly 40 times lower and differential resistance values approximately 50 times larger than those of bare nanobridges with similar dimensions [105].

One of the objective of this work is to improve nanowire-based SQUIDs beyond the limitations, which affect this type of weak links [10]. Previously reported nanowire-based SQUIDs showed promising results, but had noise performances not competitive with state-of-the-art at $T = 77$ K. Here we have shown that GDBs have electrical properties, which overcome the limitations of nanowires, making them very interesting for applications. In the next section we will present the results obtained for GDB-based SQUIDs. Our work focused on optimization of SQUIDs aimed at magnetometer applications (i.e. increased SQUID magnetic area). At the same time, the development of low noise HTS SQUIDs is of paramount importance for future, alternative applications of HTS such as high-frequency HTS superconducting quantum interference filters (SQIFs) [111], HTS rapid single flux quantum (RSFQ) circuits [112], and large-scale junctions arrays for high-performance computing and high-frequency sensors [113, 114]. GDB-based nanoSQUIDs could also be instrumental in the development of ultra-low noise magnetic flux sensors for fundamental studies of magnetism at the nanoscale and the detection of a single electron spin [81, 115, 116].

5.3 GDB-based SQUIDs

SQUIDs implementing YBCO GDBs as weak links with different hairpin loop sizes, have been fabricated on STO substrates. The linewidth and slit width of the hairpin loops (see Fig. 5.4(a)) are 2 and $0.5\ \mu\text{m}$, respectively, while the slit length l_{slit} is varied to change the SQUID loop inductance L_{SQ} . An SEM image of a GDB-based SQUID (device SQ1) with $W = 200\ \text{nm}$ and $L = 50\ \text{nm}$ is shown in Fig. 5.4(b). A summary of the geometry and electrical properties for the SQUIDs presented here is reported in table 5.2. Two IVCs at $T = 77\ \text{K}$ for SQ1 are shown in Fig. 5.4(c). Here we show the IVCs obtained for integer ($n\Phi_0$) and half integer ($(n + 1/2)\Phi_0$) values of applied magnetic flux quanta. The modulation of the SQUID critical current I_c as a function of magnetic flux is presented in the inset of Fig. 5.4(c). Device SQ1 shows electrical properties similar to the one reported for single GDBs: the IVCs resemble those of a RSJ with critical current value, I_c , strongly suppressed in comparison to bare nanowires. The voltage modulations of SQ1 as a function of applied magnetic flux are shown in Fig. 5.4(c). Here, each curve corresponds to a fixed value of bias current, which is increased with $1.8\ \mu\text{A}$ steps.

Since for GDBs the I_c and parasitic kinetic inductance are lower than bare nanowires, larger SQUID loops can be implemented, while maintaining large values of ΔV and low magnetic flux noise $S_\Phi^{1/2}$. As we will discuss in the next section, larger SQUID loops are instrumental to improve the performances of SQUID-based magnetometers. Our GDB-based SQUIDs exhibit large values of voltage modulation, with $\Delta V_{\text{max}} = 27 - 50\ \mu\text{V}$ ($l_{\text{slit}} = 20 - 8\ \mu\text{m}$, $L_{\text{SQ}} = 160 - 20\ \text{pH}$). Comparing these values to nanowire based SQUIDs with similar hairpin loop dimensions, which have voltage modulation depth in the range $1-5\ \mu\text{V}$ for $l_{\text{slit}} = 2 - 32\ \mu\text{m}$ [10], corroborates the improved weak link properties of GDBs.

The voltage modulation depth ΔV of SQ1 measured as a function of I_b is shown in Fig. 5.5(a), green line. From this, we can extract the maximum voltage modulation depth $\Delta V_{\text{max}} = 27\ \mu\text{V}$, at $I_b \simeq 17\ \mu\text{A}$. This can be used to approximate the transfer function of the SQUID, which is defined as $V_\Phi = \max(\delta V/\delta\Phi) \simeq \pi\Delta V_{\text{max}}/\Phi_0$; for SQ1 we obtain $V_\Phi = 115\ \mu\text{V}/\Phi_0$. Moreover, we define δR as the differential resistance obtained at the working point of the SQUID, i.e. in correspondence of the maximum voltage modulation

The magnetic flux noise of the SQUID $S_\Phi^{1/2}$ is measured in a magnetic shielded room (MSR) to minimize the environmental noise contribution. The device is connected to a commercial Magnicon SEL-1 dc SQUID electronics. This setup allows to measure the SQUID in a Flux locked loop (FLL) configuration [117]. Moreover, the contribution of the low frequency critical current noise of the SQUIDs to the total measured voltage noise is minimized by using an ac bias reversal scheme at a frequency of 40 kHz. The voltage noise of the SQUID is first measured and the flux noise is obtained as $S_\Phi^{1/2} = S_V^{1/2}/V_\Phi$. The magnetic flux noise for SQ1 is shown in Fig. 5.5(b). The bias current value at which ΔV is maximized corresponds to the crossing point of the $\delta V/\delta I$ vs I_b curves taken at $\Phi = n\Phi_0$ and $\Phi = (n+1/2)\Phi_0$ (see red and blue lines in Fig 5.4(a)). The value of $\delta V/\delta I$ at the crossing point defines our δR .

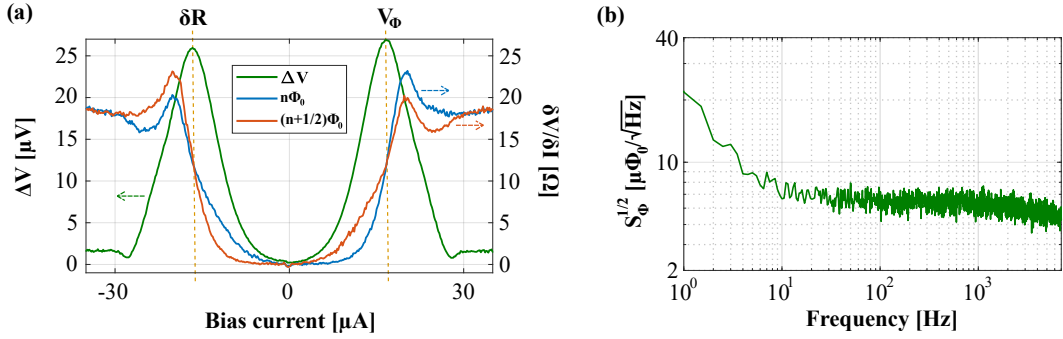


Figure 5.5: (a) left axis: ΔV as a function of bias current, right axis: $\delta V/\delta I$ as a function of bias current, the two curves are calculated from the IVCs measured at $\Phi = n\Phi_0$ (red line) and $(n + 1/2)\Phi_0$, see Fig. 5.4(b). (b) Magnetic flux noise measured on SQ1 at $T = 77$ K.

The $1/f$ knee is at 10 Hz while the white magnetic flux noise is as low as $S_\Phi^{1/2} = 6 \mu\Phi_0/\sqrt{\text{Hz}}$. This value is close to the expected magnetic noise calculated with Eq. 3.8 and is comparable to the state-of-the-art sensitivity obtained with grain boundary-based YBCO SQUIDs $2.2 - 10 \mu\Phi_0/\sqrt{\text{Hz}}$ [118, 119, 120, 121, 122, 123]. The noise obtained for SQ1 is almost an order of magnitude lower than the one obtained on bare nanowire-based SQUIDs [10]. This shows the potential of GDBs for SQUID applications and makes them a valid alternative to GB-based JJs in terms of noise performance, while offering a more scalable fabrication procedure.

5.3.1 Temperature dependence of electronic properties

Our aim is to optimize the performances of the SQUIDs at $T = 77$ K, nevertheless their operation can be extended to any temperature, from ultra-low up to the critical temperature of the weak links. We characterized a GDB-based SQUID as a function of temperature and determined the evolution of the SQUID voltage modulations, critical current and differential resistance in the temperature range $8 \text{ K} < T < 84 \text{ K}$. The data presented here have been obtained on device SQT, which was fabricated with $W = 150$ nm and $L = 40$ nm, and had $I_c = 92 \mu\text{A}$ at $T = 77$ K. SQUID SQT has a hairpin loop with linewidth of $2 \mu\text{m}$, slit width $0.5 \mu\text{m}$, and slit length $l_{\text{slit}} = 8 \mu\text{m}$.

In Fig. 5.6(a) we show the voltage modulation depth extracted at the working point ΔV_{\max} of SQUID SQT as a function of T . This shows some interesting features which are tied to the physics governing the GDB transport. Starting from low T , the value of ΔV_{\max} decreases rapidly and reaches a plateau for $T \geq 25$ K. From here, ΔV_{\max} is decreasing slowly up to $T \simeq 60$ K, where we observe an increase in voltage modulation depth, reaching a local maximum at $T = 65$ K. If T is further increased, ΔV_{\max} decreases rapidly once again and reaches 0 at $T \geq 84$ K, which is the critical temperature of the weak links (the critical temperature of the YBCO film is $T_c = 89$ K). This non-monotonic trend is the result of the combined behavior of δR and ΔI_c , which are shown in Fig. 5.6(b). Here, one can see that while the critical current modulation depth $\Delta I_c(T)$ decreases with increasing temperature, the differential resistance δR is non-monotonic. The latter decreases with T in the interval $8 \text{ K} < T < 30$ K while it starts to increase linearly for $T > 55$ K. The product $\Delta I_c \delta R$, cross symbols in Fig. 5.5(a), follows closely the measured value of ΔV_{\max} (open discs).

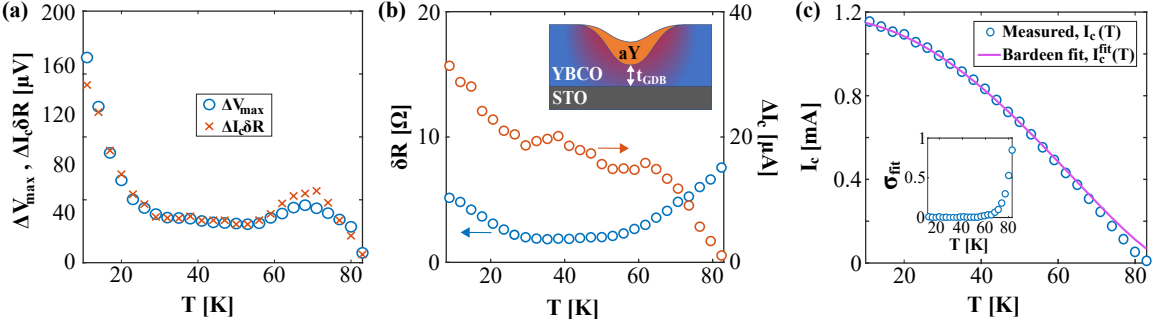


Figure 5.6: (a) The voltage modulation at working point ΔV_{\max} (open discs) as a function of temperature, obtained as the maximum of the measured ΔV , is compared to the product $\Delta I_c \delta R$ (crosses). (b) Differential resistance (blue circles) at the working point δR and critical current modulation depth (red circles) ΔI_c vs. T . The inset shows a schematic cross section of a GDB. t_{GDB} is the thickness of the superconducting YBCO in the groove, while aY represents the amorphous YBCO layer re-deposited during Ar^+ ion milling. (c) Measured critical current versus temperature, I_c (open symbols), compared to the Bardeen fit, I_c^{fit} (solid line). Inset show the deviation, σ_{fit} , of the measured critical current from the fit as $\sigma_{\text{fit}} = (I_c^{\text{fit}} - I_c) / I_c^{\text{fit}}$. (adapted from [107])

The behavior of δR at higher T is characteristic of SNS-type junctions [72], where R_N (here replaced by δR) increases with increasing temperature. A similar behavior of ΔV_{\max} was reported for *unintentionally* damaged nanowires [88], especially when the weak links lateral dimension was reduced below 200 nm. In [88], the damage from the fabrication procedure resulted in different values of T_c along the wire. SQUIDs based on such weak links demonstrated a $\Delta V_{\max}(T)$ very similar to the data shown in Fig. 5.6(a). These results were attributed to a transition from SS'S to SNS-type junction.

To test if the transport properties of our GDBs as a function of temperature are influenced by a transition from a SS'S- to a SNS-like weak link behavior, we performed a fit of the measured critical current vs temperature (see Fig. 5.6(c)) using the Bardeen expression for the depairing current of superconducting nanowires. The Bardeen expression reads [79, 124]

$$I_c \propto \left(1 - \left(\frac{T}{T_c}\right)^2\right)^{3/2} \quad (5.1)$$

where T_c is the critical temperature of the YBCO film (in our case $T_c = 89$ K). It has been shown that Eq. 5.1 can be used to successfully reproduce the critical current of pristine YBCO nanowire, from low temperature up to T_c [79]. From Fig. 5.5(c), one can see that Eq. 5.1 fits well the I_c measured for SQT at low T . This suggests that in this temperature range the GDBs behave as short Dayem bridges with a length close to the gap length L and thickness equal to t_{GDB} . This thickness can be estimated by dividing the critical current of the GDB at low T by the typical critical current density of thin Dayem nanobridges at $T = 4.2$ K. Hence, given that $j_c(4.2 \text{ K}) \simeq 2 \times 10^7 \text{ A/cm}^2$ [110], we obtain $t_{\text{GDB}} \simeq 15 \text{ nm}$ as the thickness of the superconducting groove, see inset of Fig. 5.5(b).

However, for $T \geq 60$ K the measured $I_c(T)$ departs from the fit, showing lower values than those predicted by the Bardeen expression. This could be the result of weakening of the superconductivity in the groove for $T > 60$ K due to thermal fluc-

tuations. In fact, it has been previously observed that a marked broadening of the superconductive transition occurs in the resistance versus T measurements of thin YBCO films[110](thinner than 30 nm). Such a broadening could be attributed to a Kosterlitz-Thouless vortex-antivortex pair dissociation transition close to the T_c of the film [125, 126]. Alternatively, the thermal activation of vortices overcoming the Bean-Livingston edge barrier could be responsible for the broadening of the resistive transition and therefore the suppressed superconductivity in the groove [92].

These results suggest that the GDBs undergo a change of transport regime when the temperature is changed, with transition at $T \simeq 60$ K. The $I_c(T)$ indicates that at low temperature the GDBs behave like short nanowires and the weak link is of SS'S-type. On the other hand, when T is increased above 60 K, superconductivity in the groove is suppressed compared to the film, making the GDB more similar to a SNS-type weak link. This is reflected in the linear increase of δR with T , which is expected for a SNS-like weak link.

Finally, we investigate the SQUID hair pin loop inductance of device SQT as a function of temperature. A current injection scheme [127] (see Fig. 5.8(a)) is used to modulate the SQUID critical current. The injection current, I_{mod} , modulates the phase difference between the two GDBs. From the modulation period ΔI_{mod} we extract the inductance of the hair pin loop as $L_c = \Phi_0 / \Delta I_{\text{mod}}$, which is shown as a function of temperature in Fig. 5.7. The inductance of the SQUID loop is composed of geometric L_c^{geo} and kinetic inductance L_c^{kin} . Using the empirical expression for a slit inductance per unit length[47] $0.4 \text{ pH}/\mu\text{m}$ we obtain $L_c^{\text{geo}} = 3.2 \text{ pH}$. The kinetic inductance per unit length can be approximated by $\mu_0 \lambda^2(T) / wt$ with μ_0 the vacuum permeability, and $w = 2 \mu\text{m}$ the line width of the hair pin loop, respectively. The temperature dependence of the London penetration depth can be approximated by the empirical expression $\lambda(T) = \lambda_0 [1 - (T/T_c)^n]^{-1/2}$, where λ_0 is the zero temperature penetration depth and the exponent n is typically $\simeq 2$ for YBCO. The total inductance of the hairpin loop L_c reads

$$L_c = L_c^{\text{geo}} + L_c^{\text{kin}} = L_c^{\text{geo}} + 2l_{\text{slit}}\mu_0 \frac{\lambda^2(T)}{wt}, \quad (5.2)$$

Fitting this expression to the measured data we obtain $\lambda_0 = 140 \text{ nm}$, and $n = 2.1$, see Fig. 5.7. These values are consistent with the expected values for bulk YBCO [17, 9]. The fit shows that even for structures larger than the GDBs (e.g. hairpin pickup loop, linewidth=2 μm), the main contribution to the SQUID loop inductance comes from the kinetic term. This is most prominent at high T where, due to $L_c^{\text{kin}} \propto \lambda^2(T)$, the kinetic term increases dramatically. The change of inductance with temperature must be taken into consideration when designing a SQUID-based magnetometer since, as it will be shown in the next section, this strongly influences the magnetic field sensitivity of such a device (change of coupling with the pick-up loop). To reduce the change of inductance with T , one could implement SQUIDs with a wider hairpin loop line width in combination with a longer slit length, l_{slit} , to minimize the kinetic contribution to the total loop inductance.

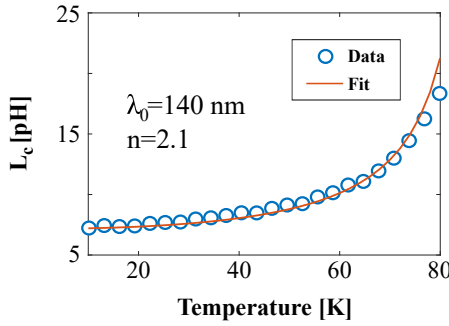


Figure 5.7: SQUID inductance versus temperature, calculated from the modulation current period I_{mod} . The data are fit with Eq.5.2.

5.4 Magnetometers

Standard SQUIDs, as they have been discussed so far, are extremely sensitive magnetic flux sensors, but, due to their small dimensions (i.e. small effective area A_{eff}), have limited magnetic field sensitivity. The effective area of a SQUID is given by $A_{\text{eff}} = \Phi/B_a$, where Φ is the magnetic flux through the SQUID loop and B_a is an externally applied field. For nanoSQUIDs, a small loop is beneficial to reduce the device inductance L_{SQ} [8, 128, 81]. However, while small L_{SQ} leads to optimal values of magnetic flux white noise $S_{\Phi}^{1/2}$, most technological applications have requirements tied instead to the white magnetic field noise $S_B^{1/2} = S_{\Phi}^{1/2}/A_{\text{eff}}$. In fact, SQUID-based magnetometers are used today in several biomedical applications [129, 130, 131, 132, 119, 10] and geophysical surveys [133, 134]. Here, in order to meet the technological requirement for $S_B^{1/2}$, it is necessary to increase A_{eff} while maintaining low values of $S_{\Phi}^{1/2}$. Different solutions can be adopted to increase the effective area A_{eff} of the device. In this work we present SQUID-based magnetometers fabricated with two of these solutions: in-plane galvanically coupled pick-up loop and flux-transformer flip-chip. These two are the most easily integrated with the fabrication process used for nanowires and GDBs.

5.4.1 In-plane pick-up loop

Magnetometers with an in-plane pick-up loop galvanically coupled to the SQUID loop have been fabricated and characterized at 77 K. A schematic circuit for the galvanic coupling is shown in Fig. 5.8(a). Here, the main advantage is the possibility of integrating the pick-up loop into the SQUID design and avoiding additional fabrication steps. An SEM image of a series of SQUIDs with hairpin loop is shown in Fig. 5.8(b), the slit length l_{slit} can be varied to change the hairpin loop inductance L_C . Several SQUID (up to 48) have been coupled to the same pick-up loop, as shown in Fig. 5.8(b), these devices can be characterized separately and the one with best performances is chosen for magnetometer application. A sketch of an in-plane pick-up loop is shown in Fig. 5.8(c). In this configuration, the applied magnetic field threading the pick-up loop leads to a screening current $I_S = B_a/L_{\text{loop}}$. Due to the galvanic coupling, this current flows around the hairpin loop. Here, I_S results in a phase difference between the weak links, which reads $\Delta\phi \propto I_S L_C 2\pi/\Phi_0$, where L_C is the coupling inductance between pick-up loop and SQUID (i.e. the hair-pin loop inductance). The phase differ-

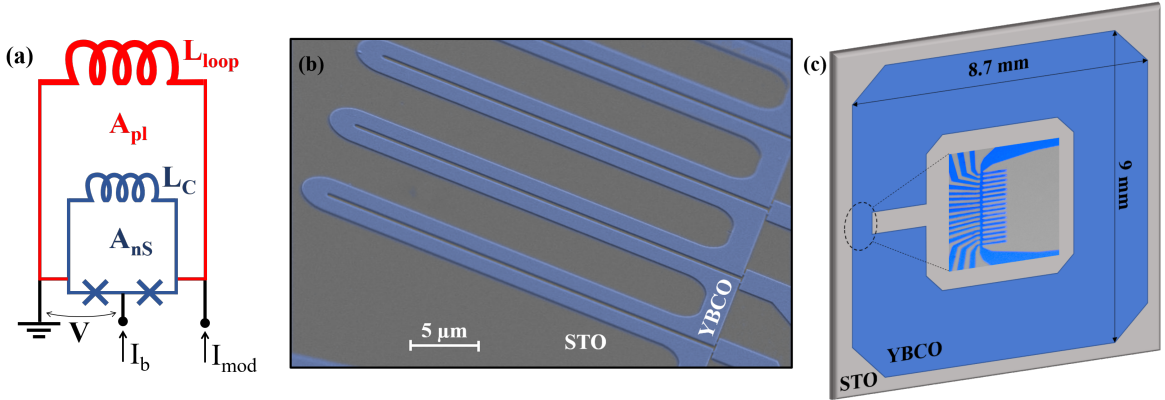


Figure 5.8: (a) Schematic circuit of the galvanic coupling with in-plane pick-up loop. A_{pl} and A_{nS} are the effective areas of pick-up loop and SQUID, respectively, and L_{loop} and L_C are the inductances of pick-up loop and hairpin loop, respectively. (b) Series of SQUID loops connected to pick-up loop. (c) Schematic of the pick-up loop fabricated on a $10 \times 10 \text{ mm}^2$ STO substrate.

ence induced by I_S results in modulation of the SQUID critical current. The galvanic coupling of a pick-up loop to the SQUID hairpin loop results in a total effective area of the SQUID equal to[9]:

$$A_{\text{eff}} = A_{nS} + A_{pl} \frac{L_C}{L_{\text{loop}}} \quad (5.3)$$

where A_{nS} and A_{pl} are the effective areas of the bare nanoSQUID and the pick-up loop, respectively, and L_{loop} is the inductance of the pick-up loop. The latter is dominated by the geometric component, due to the large linewidth of the loop (typically $1 - 2 \text{ mm}$). From Eq. 5.3, it is clear that in order to increase A_{eff} , one needs to increase the coupling between pick-up loop and SQUID by increasing L_C . However, this has the adverse effect of increasing the total inductance of the SQUID L_{SQ} which results in increased β_L . To obtain the lowest value of $S_B^{1/2}$, the optimal value of L_C needs to be found to optimize both flux noise and effective area or rather the ratio between the two quantities, $S_\Phi^{1/2}/A_{\text{eff}}$.

Moreover, the maximum dimensions of the pick-up loop are limited by the choice of substrate dimensions. In our PLD system, which is used to grow the YBCO films in the nanofabrication laboratory at Chalmers university, the substrate dimensions cannot exceed $10 \times 10 \text{ mm}^2$ without detrimental effects to the film quality. In this work, two different substrate sizes have been used to fabricate the magnetometers, resulting in two different pick-up loop dimensions. First, on a $5 \times 5 \text{ mm}^2$ STO substrates, we achieved a pick-up loop with lateral dimensions of $3.5 \times 3.5 \text{ mm}^2$ and linewidth of 0.5 mm . Second, $10 \times 10 \text{ mm}^2$ substrates allowed us to increase the pick-up loop outer dimension to $8.7 \text{ mm} \times 9 \text{ mm}$ with linewidth of 2 mm (shown in Fig. 5.8(c)).

To characterize a magnetometer, the flux noise $S_\Phi^{1/2}$ of the device is first measured and the field noise is obtained according to $S_B^{1/2} = S_\Phi^{1/2}/A_{\text{eff}}$. The effective area is determined separately by measuring the responsivity dV^{el}/dB_a of the magnetometer operated in FLL mode using a calibrated coil. Here V^{el} is the output voltage of the SQUID electronics in FLL mode. Together with the SQUID transfer function operated

	L [nm]	W [nm]	pick-up loop [mm 2]	l_{slit} [μm]	ΔV [μV]	I_c [μA]	L_C [pH]	A_{eff} [mm 2]	$S_{\Phi}^{1/2}$ [$\frac{\mu\Phi_0}{\sqrt{\text{Hz}}}$]	$S_B^{1/2}$ [$\frac{\text{fT}}{\sqrt{\text{Hz}}}$]
SQT	40	150	-	8	50	92	18	-	-	-
SQ1	50	200	3.5×3.5	20	27	15	160	0.122	6	100
SQ2	50	200	8.7×9.0	16	39	15	48	0.15	6	85
SQ3	50	200	8.7×9.0	30	16.5	30	102.6	0.39	10.6	63
SQ4	50	200	8.7×9.0	30	18.7	16	103	0.39	11	59

Table 5.2: Summary of the geometry and electrical properties of the different GDB-based SQUIDs at $T = 77$ K.

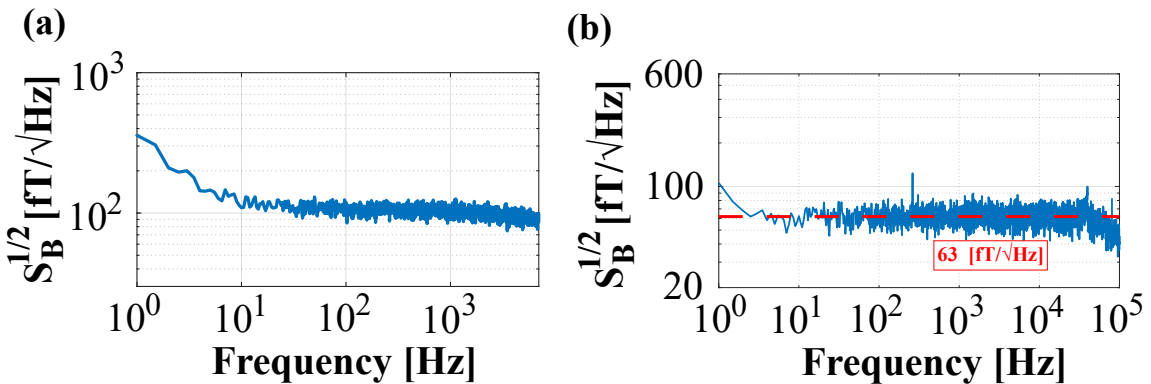


Figure 5.9: (a) Magnetic field noise measured on device SQ1, the white field noise is as low as $S_B^{1/2} = 100$ fT/ $\sqrt{\text{Hz}}$. (b) Magnetic field noise measured on device SQ3, the red broken line indicates the white field noise $S_B^{1/2} = 63$ fT/ $\sqrt{\text{Hz}}$

in FLL mode, V_{ϕ}^{FLL} , one obtains the effective area $A_{\text{eff}} = (dV/dB_a)/V_{\phi}^{\text{FLL}}$, see [118] for details. The measurements are performed in the same setup (MSR and SQUID electronics) used to measure the flux noise data presented in the previous section. A summary of the geometrical and electrical properties of different devices is reported in Table 5.2. Device SQ1 is the best magnetometer which we obtained with a 5×5 mm 2 substrate. SQ1 shows a particularly high value of voltage modulation depth (30 μV) considering the high value of coupling inductance $L_C = 160$ pH. This ΔV_{max} is an order of magnitude higher than what was previously obtained with nanowire-based SQUIDs with similar values of L_C [10]. The high voltage modulation depth results in white flux noise as low as $6 \mu\Phi_0/\sqrt{\text{Hz}}$, with the 1/f knee close to 10 Hz. Moreover, the large value of L_C leads to good coupling between pick-up loop and SQUID, resulting in an effective area $A_{\text{eff}} = 0.122$ mm 2 . This, combined with the flux noise, gives a white magnetic field noise $S_B^{1/2} = 100$ fT/ $\sqrt{\text{Hz}}$, as shown in Fig. 5.9(a). This is a very promising result considering it has been obtained for a magnetometers with a pick-up loop smaller than standard in-plane magnetometers ($\geq 8 \times 8$ mm 2) [135, 136, 68, 10, 119, 121].

To increase the effective area further we realized SQUID magnetometers on two 10 mm \times 10 mm STO substrates. Each chip contained one large pick up loop galvanically connected to a set of GDB-based SQUIDs with varying values of l_{slit} . SQ3 and SQ4 were fabricated on the same substrate sharing the same pick up loop whereas SQ2 was realized on a second substrate with nominally the same pick up loop dimensions

as the one for SQ3 and SQ4. Among the three, the best result in terms of flux noise has been achieved for SQ2 ($l_{\text{slit}} = 16 \mu\text{m}$), with $S_\Phi = 6 \mu\Phi_0/\sqrt{\text{Hz}}$. However, the coupling inductance was lower than expected with $L_c = 48 \text{ pH}$ given a hairpin loop with $l_{\text{slit}} = 16 \mu\text{m}$, compared to $L_C = 160 \text{ pH}$ obtained with SQ1, where $l_{\text{slit}} = 20 \mu\text{m}$. Therefore, the A_{eff} of SQ2, with a $10 \times 10 \text{ mm}^2$ substrate, is only slightly larger than device SQ1 on a $5 \times 5 \text{ mm}^2$ substrate, showing the importance of high values of L_C . Such a difference in inductance, given hairpin loops with similar dimensions, can be explained by differences in the YBCO films. Since the PLD process depends on the size of the substrate (see Appendix A) this can result in different film properties. For example, a small difference in film thickness and T_c could be expected between films deposited on $5 \times 5 \text{ mm}^2$ and $10 \times 10 \text{ mm}^2$ substrates. However, even a small change of these parameters would lead to substantial changes in the value of the SQUID loop kinetic inductance. This is most likely the cause of the discrepancy between L_C measured for devices fabricated on $5 \times 5 \text{ mm}^2$ and $10 \times 10 \text{ mm}^2$ substrates.

Nevertheless, when l_{slit} is increased, the performance of the magnetometers improves. In fact, on SQ3 and SQ4 the coupling was improved, with effective areas as large as $A_{\text{eff}} = 0.4 \text{ mm}^2$. On the other hand, the flux noise increased to $11 \mu\Phi_0/\sqrt{\text{Hz}}$, due to lower values of ΔV , as expected for increased L_{SQ} . The measured magnetic field noise for SQ3 is shown in Fig. 5.9(b), here we can see that the 1/f knee is at 2 Hz and the white magnetic field noise is $S_B^{1/2} = 63 \text{ fT}/\sqrt{\text{Hz}}$ at $T = 77 \text{ K}$. This is almost a factor 2 improvement compared to device SQ1 and represents the lowest magnetic field noise achieved with nanowire-based SQUID magnetometers. Our result also compares well with the noise values obtained in the state-of-the-art SQUID-based magnetometers, fabricated with GB-based JJs coupled to an in-plane pick-up loop, which reached $S_B^{1/2} = 20 - 50 \text{ fT}/\sqrt{\text{Hz}}$ [135, 136, 119, 121, 118, 123].

The results obtained on the 5×5 substrate show the potential of our GDB-based SQUIDs for magnetometer applications. In fact, if the performances of SQ1 (i.e. low level of flux noise $S_\Phi = 6 \mu\Phi_0/\sqrt{\text{Hz}}$), in combination with its large coupling inductance value ($L_C = 160 \text{ pH}$), is obtained on a $10 \times 10 \text{ mm}^2$ substrate, the resulting effective area would approach $A_{\text{eff}} \simeq 0.6 \text{ mm}^2$ resulting in a white magnetic field noise as low as $S_B^{1/2} = 20 \text{ fT}/\sqrt{\text{Hz}}$. Here, the main technological limitation is the fabrication process, in particular the PLD, which needs to be optimized for $10 \times 10 \text{ mm}^2$ substrates. Since the quality of the YBCO film deposited by PLD degrades when using larger substrates, lower quality GDB are obtained with less reproducible properties, i.e. the spread of the measured critical current density is around 22% (compared to 15% obtained for GDB on 5×5 substrates). The larger spread would additionally lead to asymmetric weak links in the SQUIDs, resulting in a further reduction of the critical current modulation depth ΔI_c , decreasing ΔV_{max} . Optimizing the process to obtain results at par, or better, with the $5 \times 5 \text{ mm}^2$ substrates would place GDB-based magnetometers at the state-of-the-art in terms of magnetic noise performance. This is especially appealing for technological applications given the fabrication procedure for GDBs, which is more easily scalable, cost effective and reproducible.

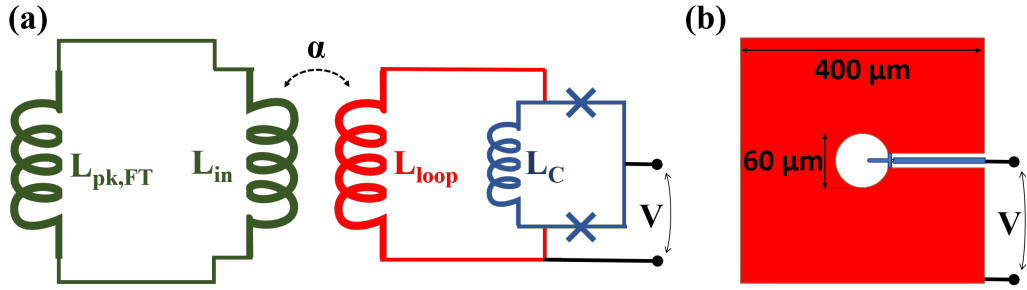


Figure 5.10: (a) Electric circuit schematic of the two-level coupling used for the flip-chip flux-transformer magnetometers. (b) Schematic of the washer pick-up loop design (red) coupled to the SQUID hairpin loop (blue). The washer has outer dimensions of $400 \mu\text{m} \times 400 \mu\text{m}$ and inner loop diameter of $60 \mu\text{m}$.

5.4.2 Flip-chip Flux-transformer

To further increase the A_{eff} of SQUID magnetometers, a flip-chip device coupled to an external multturn superconducting flux-transformer (FT) has been fabricated. In general, for such devices the SQUID loop is inductively coupled to an external FT. In our case, the latter consists of a big pick-up loop galvanically coupled to a multi-turn flux focusing loop [10, 121]. Generally, when the SQUID is coupled to an external flux-transformer, a washer type SQUID loop is coupled to the FT [137, 128]. Washer type SQUID loops have the advantage of reduced L_{SQ} despite the large dimensions (outer width in the $100 \mu\text{m}$ range). However, this approach results in low coupling between the SQUID and FT due to the YBCO film thickness being smaller than the London penetration depth ($t_{\text{YBCO}} = 50 \text{ nm}$) [138]. To partially solve this problem, a two-level coupling scheme is used [10]. Here, the SQUID is first galvanically coupled to an in-plane pick-up loop, as shown in the previous section. The pick-up loop is then inductively coupled to the FT, acting as an intermediary coupling between FT and SQUID loop. A sketch of this coupling scheme is shown in Fig. 5.10(a). The best performance (e.g. best coupling) is achieved when the dimension of the pick-up loop matches the inner most dimension of the flux-focusing coil, which in our case is $60 \mu\text{m}$. Here, $L_{\text{pk,FT}}$ and L_{in} are the inductance of flux-transformer pick-up loop and focusing coil, respectively, while $\alpha (<1)$ is the coupling parameter between focusing coil and SQUID pick-up loop. For $t_{\text{YBCO}} = 50 \text{ nm}$, the typical value for the coupling parameter is $\alpha \simeq 0.4$ for a flip-chip to pick-up loop separation ranging from 300 nm to $10 \mu\text{m}$ [138]. α decreases rapidly when the separation increases above $10 \mu\text{m}$. The final effective area of a SQUID magnetometer based on flip-chip technology employing this coupling scheme can be approximated as[10]:

$$A_{\text{eff}} \simeq \frac{\alpha}{2} \frac{L_C}{\sqrt{L_{\text{loop}} L_{\text{in}}}} A_{\text{eff,FT}} \quad (5.4)$$

where $A_{\text{eff,FT}}$ is the effective area of the flux-transformer. The SQUID is fabricated with the same hairpin loop design as for the devices presented in the previous section (see Fig. 5.8(a)). The data presented here have been measured on device SQFT, which has $l_{\text{slit}} = 12 \mu\text{m}$, GDBs with $W = 200 \text{ nm}$ and $L = 40 \text{ nm}$, resulting in $I_c = 175 \mu\text{A}$ and $I_c \delta R = 350 \mu\text{V}$ at $T = 77 \text{ K}$.

To improve the coupling between FT and SQUID pick-up loop, the latter uses a

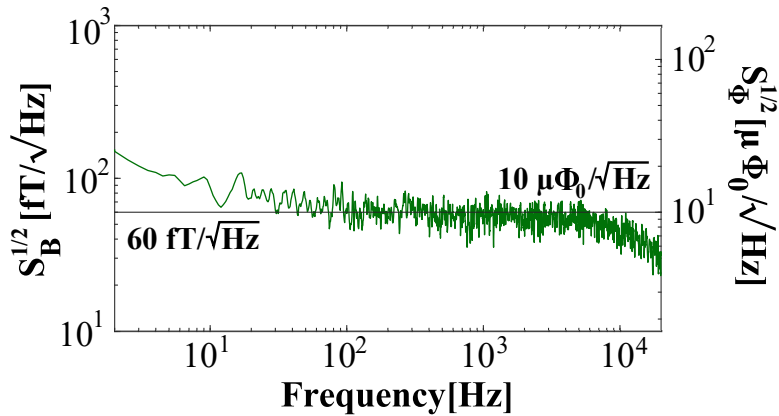


Figure 5.11: Magnetic field (left-axis) and flux (right-axis) noise measured on SQFT, the white magnetic field and flux noise are $60 \text{ fT}/\sqrt{\text{Hz}}$ and $10 \mu\Phi_0/\sqrt{\text{Hz}}$, respectively. (adapted from [106])

washer design, which is shown in Fig. 5.10(b). This design increases the coupling parameter, α , while keeping a low value of inductance L_{loop} , hence improving the coupling between washer and SQUID loop as well (lower L_{loop} increases the ratio $L_C/\sqrt{L_{\text{loop}}}$ in Eq. 5.3). The inner diameter of the washer is $60 \mu\text{m}$ to match the innermost circle of the flux-transformer focusing coil. The multilayer YBCO FT was fabricated by M. Chukharkin at Chalmers on a SrTiO_3 (001) substrate and is composed of a square pick-up loop (outer dimensions are $9 \times 9 \text{ mm}^2$ with linewidth of 1 mm) galvanically coupled to a multi-turn flux focusing coil. The latter has 12 turns with linewidth of $7.5 \mu\text{m}$ and $4 \mu\text{m}$ pitch. The details for the FT fabrication are reported in [139].

SQUID SQFT has been measured in the same setup used for the previously discussed SQUID experiments in section 5.3 (MSR plus Magnicon SEL-1 SQUID electronics). The effective area obtained from responsivity measurements is $A_{\text{eff}} = 0.41 \text{ mm}^2$. This value is consistent with previously reported data obtained on similar devices [10]. The measured flux noise is shown in Fig. 5.11, here the white flux noise is $S_\Phi^{1/2} = 10 \mu\Phi_0/\sqrt{\text{Hz}}$ above 10 Hz. This value is comparable with the SQUIDs reported in Table 5.2. However, SQFT has a much smaller squid loop (small l_{slit} and L_C) which should have given a lower flux noise. The measured $S_\Phi^{1/2}$ might be higher due to low quality of the GDBs (low ΔI_c and δR), most likely related to fabrication issues.

The small SQUID loop is detrimental for A_{eff} since it results in low L_C . Nevertheless, the effective area of SQFT is $A_{\text{eff}} = 0.41 \text{ mm}^2$, yielding a white magnetic field noise $S_B^{1/2} = 60 \text{ fT}/\sqrt{\text{Hz}}$, see Fig. 5.11. These values are comparable with the best results we obtained on SQUIDs with in-plane pick-up loop (see SQ3 and SQ4 from Table 5.2). Considering the low quality of the GDBs and small l_{slit} , the noise performance of SQFT shows the potential improvement of magnetic field noise achievable with flip-chip devices. Indeed, the lowest level of magnetic field noise for SQUID-based magnetometers $S_B^{1/2} = 4 \text{ fT}/\sqrt{\text{Hz}}$ has been achieved with an external flux-transformer[68] (albeit with dimensions of $16 \times 16 \text{ mm}^2$). While still far away from the state-of-the-art, the results obtained with SQFT represents a net improvement compared to previously reported levels of sensitivity for flip-chip magnetometers based on bare nanowires

($S_B^{1/2} = 240 \text{ fT}/\sqrt{\text{Hz}}$ [10]). If the two-level coupling scheme could be substituted by a direct inductive coupling of the flux-transformer to a washer type SQUID loop, then a possible effective area $A_{\text{eff}} \simeq 2.2 \text{ mm}^2$ could be achieved [138]. Such a large value of effective area, together with flux noise $S_\Phi^{1/2} = 6 \mu\Phi_0/\sqrt{\text{Hz}}$, would result in white magnetic flux noise $S_B^{1/2} \simeq 6 \text{ fT}/\sqrt{\text{Hz}}$. This would represent one of the lowest levels of field noise reported for a YBCO SQUID-based magnetometer, comparable with results obtained for LTS-based SQUID magnetometers ($1 - 5 \text{ fT}/\sqrt{\text{Hz}}$ [140]), making GDB-based devices one of the best choices for technological applications.

However, the increased sensitivity of FT based magnetometers comes at the cost of a more complicated and expensive fabrication. In fact, an in-plane pick-up loop magnetometer is fabricated in a single process, while for flip-chip devices the additional fabrication of the FT, which is in itself a challenging process [139], is required. Moreover, the $1/f$ knee frequency in this type of devices is typically higher than for the in-plane magnetometers, in our case just below 100 Hz, an order of magnitude higher than for SQ3. Thus, the specific requirements of the target technological application (measurement sensitivity and frequency range) should be taken into consideration when selecting which kind of magnetometers to use. For example, HTS-based MEG would outperform their LTS counterpart already with magnetic field noise $\leq 50 \text{ fT}/\sqrt{\text{Hz}}$ [141]. Here, the performance of GDB-based magnetometers with in-plane pick-up loops would suffice, while the low cost of fabrication would be beneficial for large-scale production.

5.5 Future considerations

In this chapter we have shown that GDBs can be instrumental for the fabrication of high-performance YBCO-based devices, in particular SQUIDs. While the results obtained here are promising, the novelty of GDBs implies that a considerable amount of improvement can still be achieved by further optimizing these weak links. In the following we present some of the possible ways, which can lead to an improvement of GDBs performance.

As presented in section 5.2, the EBL sets an upper limit for the GDBs width, $W_{\text{max}} \simeq 200 \text{ nm}$, which at the moment limits the optimization of GDBs through further variations of the nanogap dimensions. However, it should be possible, by optimizing the various process steps, such as EBL, oxygen plasma and ion milling, to achieve GDB with $W_{\text{max}} \geq 200 \text{ nm}$ and reproducible values of I_c . This could improve the performance of GDB-based SQUIDs by further reducing the L_{kin} of the weak links.

Alternatively, one of the configurations already used to boost the performance of YBCO-based devices is the junctions array [113, 111]. Here, several (from tens up to thousands) junctions, or weak links, are connected in series to increase considerably the characteristic voltage of the final device, or in some case in parallel for absolute magnetic field detection, e.g. in superconducting quantum interference filters SQIF [111]. In fact, considering a series of N_{wl} weak links, assuming homogeneous SC properties (critical current, I_c , and normal resistance, R_N , for the single weak link), the characteristic voltage of this series is equal to $N_{\text{wl}}I_cR_N$. Hence, the performance of the series scales linearly with N_{wl} . Arrays of Josephson Junctions have shown the potential

for metrological applications [48, 49], quantum electronics [142] and sensors [111, 113, 143].

However, for HTS applications, it is challenging to fabricate arrays of GB-based JJs, especially if they need to be integrated in a SQUID. GDBs would represent the ideal platform to implement arrays of weak links. In the easiest case, a nanobridge containing two grooves in series could be easily integrated in the SQUID design. This would possibly result in a factor 2 increase of the SQUID δR and, thus, twofold increase of ΔV_{\max} . Moreover, this kind of solution could be easily scaled to multiple gaps ($N_{wl} > 2$) GDBs, without any complication of the fabrication process. Devices implementing multiple-gap GDBs will be fabricated and characterized in the future and could represent a marked improvement for this technology.

Finally, a very promising route for the optimization of GDBs is electromigration at $T \simeq 4.2$ K and high bias voltages ($V \geq 0.6$ V). If optimized, this would be an interesting route to obtain GDBs with higher differential resistance and lower critical current. Electromigration has been previously reported for different YBCO-based JJ and weak links [144, 145, 146]. For GDBs, we found that by applying high values of bias current at $T = 4.2$ K, the electrical properties of the weak links can be tuned due to electromigration effects. The final results depend strongly on the voltage drop V over the weak link. In fact, two regimes can be identified, similarly to [145], depending on the value of V : the first is *healing*, for $V = 0.5 - 0.7$ V; the second is *degradation*, for $V > 0.7$ V. These voltage regimes are consistent among different samples and have the following effect:

- **Healing** ($V = 0.5 - 0.6$ V): In this regime, the I_c of the weak link can be increased by a few 10%. Most probably, oxygen is moved from the electrodes to the GDB where it compensates for the possible oxygen loss during the fabrication process.
- **Degradation** ($V > 0.7$ V): In this regime, the I_c of a GDB can be strongly reduced (from $I_c > 100$ μ A down to only 5 μ A) while the shape of the IVC becomes more RSJ-like. Moreover, while I_c decreases, the value of R_N (and thus δR) increases and can reach values $R_N \geq 1$ k Ω . While in the degradation regime, I_c can be completely suppressed, driving the weak link to the resistive behavior.

Some preliminary results of electromigration performed on a GDB are reported in Fig. 5.12. In panel (a), one can see the comparison between IVCs measured on the same GDB right after fabrication (blue), after healing (red) and after degradation (orange). The original critical current is $I_c = 100$ μ A, after the healing it increased to $I_c = 130$ μ A, the shape of the IVCs are also different, however they are not yet close to be described by the RSJ model. When I_b is further increased and the voltage drop over the GDB exceeds 0.7 V, the I_c start decreasing rapidly and is lowered to roughly 5 μ A. The IVC for the GDB after degradation resembles closely the IVC of a RSJ, see inset of Fig. 5.12(a). While the I_c decreases, the normal resistance is strongly increased and can reach values as high as $R_N = 1.2k$ Ω . The differential resistance calculated from the IVC after degradation is shown in Fig. 5.12(b). Here the shape of $\delta V/\delta I$ resembles the differential resistance expected for a RSJ (see Fig. 3.1(c)). Such a high value of R_N results in a very high characteristic voltage, given the low value of critical current.

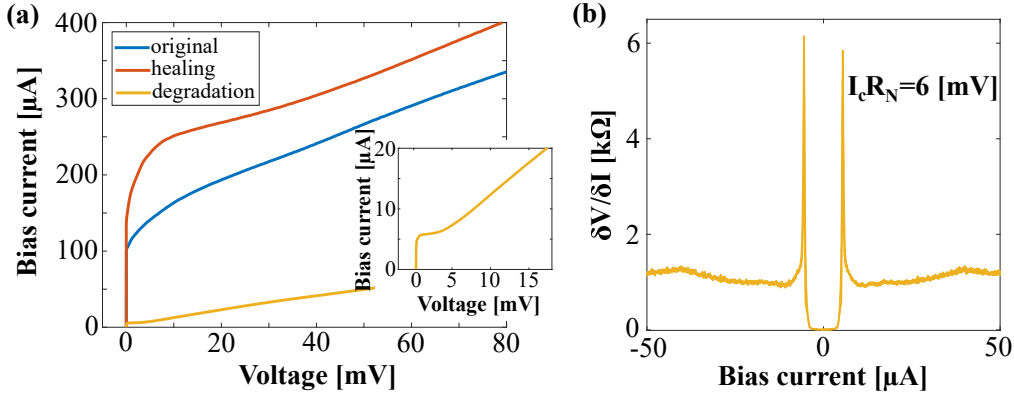


Figure 5.12: (a) Comparison of the IVCs measured at $T = 4.2 \text{ K}$ on the same junctions as fabricated (blue line) and after two steps of electromigration (healing in red, degradation in orange). Inset shows a zoom-in for the IVC of the junction after degradation, which is very close to a RSJ. (b) Differential resistance $\delta V/\delta I$ obtained from the IVC for the junction after degradation.

Indeed, after degradation, the GDB presented in Fig. 5.12 has $I_c R_N \simeq 6 \text{ mV}$.

This GDB does not show SC behavior at $T = 77 \text{ K}$ after the degradation. Nevertheless, the electromigration process could be optimized to work at LN₂ temperature. This has been tested but at $T = 77 \text{ K}$ the electromigration is more difficult to control. This can be related to lower heat dissipation resulting in overheating of the GDB and extreme degradation of the material. If the electromigration can be optimized, the performance of devices with such weak links would be very interesting for technological applications. The data presented in this chapter are very promising for the future of GDBs and, with a little optimization, these weak links could represent a new state-of-the-art for HTS devices. Furthermore, if electromigration would be applied to SQUIDs, the process could be used to improve the weak links parameters (I_c and δR) and at the same time possibly achieve more symmetric SQUIDs for improved critical current modulation depth ΔI_c , resulting in improved ΔV_{\max} .

CHAPTER 6

Noise in nanowires

The phase diagram of YBCO, introduced in Chapter 2, exemplifies the complexity, which researchers face when studying the physic of cuprate HTSs. The yet unknown microscopic mechanism ruling the physical properties of high- T_c superconductors is inevitably tied to the understanding of the interplaying orders exhibited by these materials in the normal state at different doping levels and temperatures. Recent studies using x-ray scattering techniques have revealed the occurrence of a Charge Density Wave (CDW) order [6, 37, 38], a two dimensional charge modulation which has been found to be ubiquitous in all cuprates. Furthermore, different orders of electronic nematicity have been observed through transport [7, 147] and torque-magnetometry [148] measurements throughout the entire phase diagram. More recently, resonant x-ray scattering studies also revealed dynamic charge fluctuations [44] in a large portion of the phase diagram, at temperatures much higher than the previously reported static CDW order.

It is clear that additional experimental investigations are required to shine light on how all those different orders are related to each other and how they are related to the phenomenon of high critical temperature superconductivity. Due to the complexity of the problem, any new finding can represent an important piece of information for the final solution. For this reason, the study of the noise properties of YBCO nanowires could be instrumental to access information on the dynamics of charge fluctuations and nematicity in the normal state of the material [149, 150]. Here, nanowires are instrumental to approach sample sizes comparable to the phenomena under study and to be sensitive to such small effects [151, 152]. Moreover, the pristine quality of the material must be ensured to minimize the contribution of defects and damaged material to the electric properties. The nanofabrication procedure presented in Appendix A has been used to obtain reproducible and high-quality nanostructures with features down to 50 nm[79, 89, 105, 153]. Measurements performed on pristine nanowires can reveal intrinsic properties of YBCO, which otherwise might not be accessible in macroscopic

devices. Moreover, a better understanding of the origin of noise in YBCO nanowire is also instrumental to improve the performances of YBCO nanodevices for technological applications.

In the following, we show the noise characterization of nanowires fabricated following Appendix A. This is the first extensive study of the resistance fluctuations of YBCO nanostructures where both temperature and doping level are varied to span a large portion of the phase diagram.

6.1 1/f noise model

A first characterization of the voltage noise due to resistance fluctuations in optimally doped YBCO nanostructures is performed at a fixed temperature, $T \simeq 100$ K, in the normal state ($T > T_c$). Here, one can expect the samples to show 1/f noise, i.e. the resistance noise power spectral density scales inversely with frequency. This is an ubiquitous form of noise which has been found in almost all electronic systems (semiconductors, metals, superconductors, etc.), but its underlying microscopic mechanism is not completely understood as of now [154]. The origin of 1/f noise noise has been understood in some, separate cases, however, no universal mechanism has been proposed for such a ubiquitous form of noise. A better understanding of 1/f noise in YBCO would be instrumental to possibly reduce its negative effect in technological applications. Moreover, this study could provide the ground for understanding if fluctuating charge order and/or locally fluctuating nematicity (breaking of rotational symmetry), as described in the next section, do contribute to the electronic noise.

The simplest picture underlying 1/f noise was introduced by Hooge [155], who found an empirical relation between the amplitude of the measured voltage 1/f noise, the dc voltage drop, and the total number of free charge carriers in the specimen. One of most important result of this picture, is the introduction of the Hooge's parameter γ [155] which is commonly used to compare the measured noise power spectral density (PSD) or the "noisiness" between different materials. γ is a material dependent, unitless parameter, which describes the strength of the underlying noise sources. The value of γ can be extracted by fitting the 1/f noise with the Hooge's empirical relation for the voltage PSD $S_V(f) = \gamma V^2 / (f \cdot n \cdot Vol)$, where V is the applied dc voltage, n is the charge carrier density, f the frequency, and Vol the structure volume ($n Vol$ gives the total number of charge carriers). This relation can be understood by assuming that the total resistance noise arises from a large ensemble of independent microscopic resistance fluctuators having a broad distribution of activation energies [154] (see also discussion of the Dutta-Horn model below). From this relation, one can see that the relative noise level is inversely proportional to the sample volume $S_V/V^2 \propto 1/Vol$. This is an additional advantage when studying nanoscale structures: by decreasing the sample volume, Vol , the relative noise fluctuations are enhanced, facilitating the detection of noise [156].

The 1/f noise of YBCO has been previously studied in a variety of samples (from bulk crystals to microbridges) with values of γ ranging from 10^{-3} to 10^7 [157, 158]. These results show the challenge of measuring the intrinsic noise for a material which

has a complex crystal structure and composite nature on long ranges ($> 1 \mu\text{m}$), making it prone to nucleation of defects. The latter are sources of high magnitude noise which can dominate the PSD in the case of 'dirty' samples. Indeed, larger samples are usually characterized by grains and extended imperfections, which might be the source of the large noise values observed in macroscopic samples [157, 159].

The relation of noise to inhomogeneity is clear when previous studies are compared. Measurements performed on YBCO crystals have shown γ values ranging from 10^3 [160] to 10^7 [157]. For YBCO films, γ is lower when compared to single crystals and in the range from 10^1 to 10^{-2} [161, 162]. If the samples lateral sizes are further reduced to reach μm -scale, then γ can be as low as 10^{-3} [158, 163]. This trend indicates that smaller samples are generally more homogeneous and have less defects which can account for the different results reported in literature. Moreover, the noise magnitude measured in our nanowires, as will be shown in the following, shows a lower value of γ [156], in the order of 10^{-4} . The noise levels reported in literature have also seen a net improvement over the years, which reflects the improvements achieved in the growth of higher quality YBCO crystals and films. To study the electric properties intrinsic of the material, it is thus necessary to deposit thin-films with the highest homogeneity and fine tune the lithography process so to preserve the pristine quality of the material down to the nanoscale [89, 79, 156, 153].

6.2 Noise at $T = 100$ K

We performed voltage noise measurements on slightly overdoped YBCO nanostructures ($T_c \simeq 86$ K) with varying lateral dimensions (ranging from 65 nm to 1 μm) fabricated on MgO substrates. We measured the voltage noise at $T = 100$ K as a function of bias current and compared our low frequency noise data to the predictions of Hooge's empirical model. Our measurement scheme is shown in Fig. 6.1(a). Here, a nanowire with resistance R is biased with a dc current I_b . The measured voltage fluctuations δV are related to the nanowire resistance fluctuations δR through $\delta V = \delta R I_b$ [164]. The voltage power spectral density is calculated as $S_V = (\delta V)^2 = S_R I_b^2$, where $S_R = (\delta R)^2$. Considering the nanowire to be ohmic, this can be written as $S_V = V^2 S_R / R^2$, where V is the DC voltage drop over the sample, therefore the power spectral density scales as $S_V \propto V^2$. The PSD is obtained by computing the discrete Fourier transform (DFT) of the measured time trace using the fast Fourier transform algorithm (FFT) [165]: $S_V = \text{FFT}(V(t))^* \cdot \text{FFT}(V(t))$, where $V(t)$ is the measured voltage time trace and $\text{FFT}(V(t))^*$ is the complex conjugate of the DFT.

In Fig. 6.1(b) we show the measured voltage noise power spectral densities at $T = 100$ K of a 50 nm thick, 100 nm wide and 300 nm long YBCO (slightly overdoped) nanowire, fabricated on a MgO substrate, for various applied bias current values. At low frequencies the noise spectra are dominated by 1/f noise, which increases with the applied bias current. The measured noise spectrum at zero bias current (blue line in Fig. 6.1(b)) is representative of the voltage amplifier input noise. At higher f , the measurements are limited by the white input voltage noise of the Low Noise Amplifier (LNA), which is $S_V^{\text{amp}} = 2.1 \times 10^{-17} \text{ V}^2/\text{Hz}$. The contribution of the latter can be minimized by implementing a cross-correlation setup using two amplifiers connected

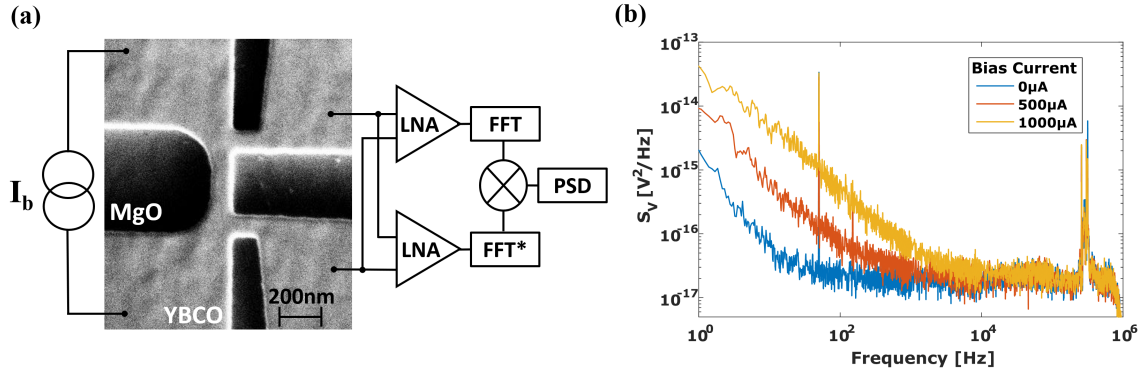


Figure 6.1: (a) SEM image of a 100 nm wide nanowire connected to a schematic of the noise measurement setup. (b) Voltage noise power spectral density measured on a 100 nm wide and 300 nm long (slightly overdoped) YBCO nanowire at $T = 100$ K for various bias current values. (adapted from [156])

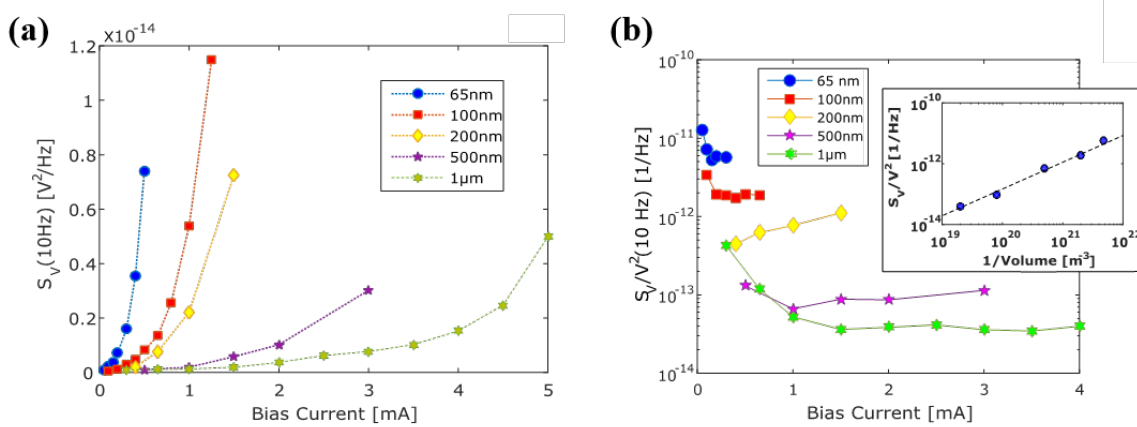


Figure 6.2: (a) Voltage PSD at $f = 10$ Hz as a function of bias I_b for different sample sizes. (b) Normalized PSD at $f = 10$ Hz as a function of bias current I_b for different sample sizes. Inset shows the dependence of S_V^2/V^2 at 10 Hz on sample volume. (adapted from [156])

to the same device. Calculating the cross-correlation spectrum from the two amplifier outputs ($V_1(t)$ and $V_2(t)$) the contributions of the uncorrelated amplifier input noise sources to the total measured noise are averaged out [166]. The cross-correlated PSD is calculated as $\text{FFT}(V_1(t))^* \cdot \text{FFT}(V_2(t))$, a schematic of the measurement setup is shown in Fig.6.1(a).

To properly confirm Hooge's empirical relation and extract γ for our YBCO nanowires, samples with different volumes are fabricated on MgO substrates following the process presented in Appendix A. The nanowires have width $W_{\text{nw}} = 65 - 1000$ nm, thickness $t = 50$ nm and length $L_{\text{nw}} = 3W_{\text{nw}}$. These samples are cooled to $T \simeq 100$ K and measured using the same scheme as in Fig.6.1(a). The values of the measured PSDs extracted at $f = 10$ Hz as a function of bias current for various sample volumes are shown in Fig.6.2(a). The corresponding normalized PSDs, S_V/V^2 , at $f = 10$ Hz are shown in Fig.6.2(b). The measured noise for all samples show a quadratic dependence on bias current, $S_V \propto I_b^2$, as expected for an ohmic resistor, which is also reflected by the values of the normalized PSDs, S_V/V^2 , approaching constant values at high

bias currents. The deviation from the expected behavior of S_V and S_V/V^2 at low values of bias current is due to contribution of the LNA input noise, which is instead negligible at higher bias. From the results presented in Fig. 6.2(b), we extract the value of $S_V^2/V^2 \times Vol. = const. \simeq 2 \times 10^{-33} \text{ m}^3/\text{Hz}$. By assuming the carrier density $n = 5.75 \times 10^{27} \text{ 1/m}^3$ [158, 161], one can use Hooge's empirical relation to extract $\gamma = 3.4 \times 10^{-4}$. This is the lowest value of γ reported in literature for YBCO and is lower than the values of γ reported for metals at $T = 300 \text{ K}$ [154]. This is an additional proof of the high-quality of the nanowires obtained with the fabrication process reported in Appendix A. Moreover, as shown in inset of Fig.6.2(b), the normalized PSD shows a linear dependence on $1/Vol$, as predicted by the Hooge's relation. This is the first instance where this relation has been shown to hold for YBCO. In fact, a strong departure from the $1/Vol$ dependence of the measured $1/f$ noise was reported in the case of devices with dimensions larger than $1 \mu\text{m}$ [163]. This has been attributed to the defects spacing in the material which is in the order of few μm .

Regarding the underlying origin of $1/f$ noise, previous studies have suggested that the resistance noise in YBCO might originate from the dynamics of doping oxygen which is located in the CuO chains [158]. Due to the strong tie between oxygen content and electrical properties of YBCO, the fluctuation of the former would result in temporal fluctuations of the local charge carrier density and local fluctuations of the conductivity. This implies that the $1/f$ noise originates from a large ensemble of noise sources or fluctuators. In this case, we can introduce the Dutta-Horn model, which describes the $1/f$ noise as the collective result of a large ensemble of Two Level Fluctuators (TLFs)[167].

6.3 Dutta-Horn model

In this model, the characteristic $1/f$ dependence of the noise is a consequence of the broad activation energy distribution of the TLFs in the ensemble. Starting from a single TLF, this can be well described by a particle in a double well potential as shown in inset of Fig. 6.4(a). The particle moves between two metastable states, which are separated by an energy barrier ΔE . In the case of a resistance fluctuator, the left and right state of the double well potential would correspond to two different resistance values. The noise spectral density of this system is given by a Lorentzian function of the form

$$S_x(f) = \frac{4\tau}{(\delta x)^2} \frac{4\tau}{1 + (2\pi f)^2\tau^2} \quad (6.1)$$

δx is the amplitude of the fluctuations and τ is the average lifetime of the particle in the two states. For given lifetimes in the two states, $\tau_{1,2}$, the average lifetime is given by $\tau = 1/(\tau_1^{-1} + \tau_2^{-1})$ [168]. In the case of a thermally activated fluctuator, τ is a function of T and can be written as

$$\tau(T) = \tau_0 \exp(E_a/(k_B T)) \quad (6.2)$$

here τ_0^{-1} is the particle attempt frequency, E_a the activation energy and k_B the Boltzmann constant. An example of a Lorentzian spectrum is shown in the inset of Fig. 6.3. Here the characteristic corner frequency of the Lorentzian is given by $f_c = 1/(2\pi\tau)$.

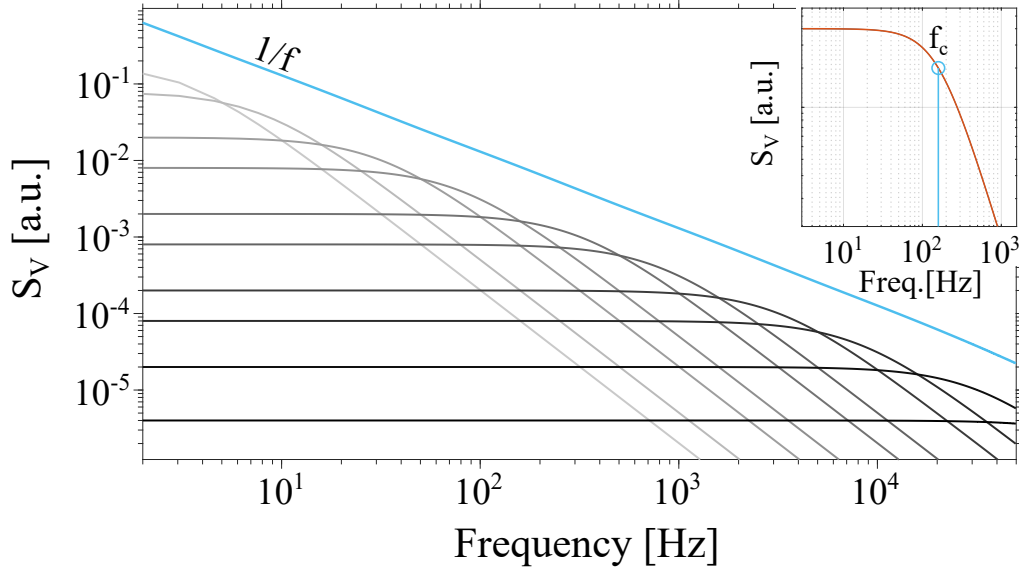


Figure 6.3: Lorentzians with uniformly distributed activation energies (grey color scale). As per the Dutta-Horn model, the sum of these Lorentzians results in $1/f$ noise (blue line). Inset show an example of Lorentzian with $\tau = 1$ ms, here we highlight the corner frequency, $f_c = 1/2\pi\tau \simeq 159$ Hz.

Considering a large ensemble of single TLFs one can introduce the distribution function $D(E)$. This represents the density (per unit energy) of TLFs as a function of activation energy. To obtain the total noise which arises from the ensemble, one needs to integrate the PSD of the TLFs over the entire energy range. Using the distribution function and the expression for $\tau(T)$ from eq. 6.2, one gets

$$S_{\text{tot}}(f) = \int_0^\infty D(E) \frac{4\tau_0 e^{E/(K_B T)}}{1 + \omega^2 \tau_0^2 e^{2E/(K_B T)}} dE \quad (6.3)$$

where $\omega = 2\pi f$. In the Dutta-Horn model a wide distribution of activation energies is assumed. This corresponds to $D(E)$ having a width $\gg k_B T$, so that the distribution can be considered almost constant over small energy intervals. With this assumption, the integral of eq. 6.3 reduces to the general expression for $1/f$ noise

$$S_{\text{tot}}(f) = k_B T D(E_\omega) \frac{1}{f} \quad (6.4)$$

where $E_\omega = -k_B T \ln(\omega \tau_0)$. So one obtains that the noise power spectral density is proportional to $1/f$. This is shown in Fig. 6.3 where we plot a series of Lorentzians with decreasing value of τ . The $1/f$ line in Fig. 6.3 is the sum of the Lorentzians. Here we can see that even few fluctuators with a uniform distribution of activation energies, E_a , leads to a PSD given by eq. 6.4. On the other hand, the PSD of eq. 6.4 is also proportional to the density of TLFs as a function of energy. Thus, measuring $S_{\text{tot}}(f)$ as a function T can reveal information on the energy distribution of the TLFs, $D(E)$.

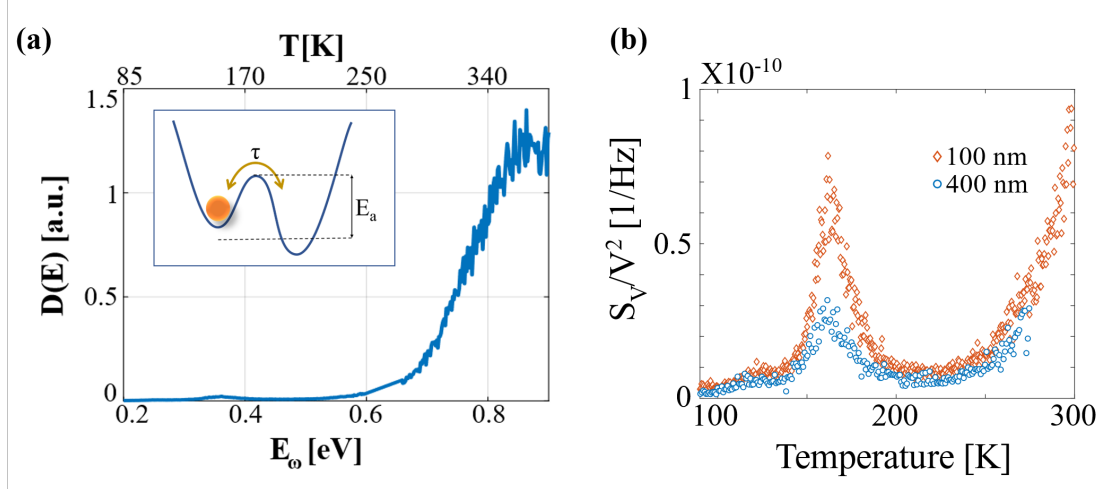


Figure 6.4: (a) Density of activation energies as a function of E_ω . The equivalent temperature, T , is shown on the top axis. The noise is measured on a 400 nm wide, slightly overdoped ($T_c = 86$ K) nanowire, NW400. Inset shows a schematic model for a particle in a double well potential with activation energy E_a separating the two meta-stable wells. (b) Normalized PSD extracted at 10 Hz in the interval $T_c < T < 300$ K for two slightly overdoped nanowires: NW100 with width of 100 nm (red diamonds) and NW400 with width of 400 nm (blue circles). The noise values for NW400 are multiplied by a factor 16 to account for the different volumes of the nanowires.

6.4 Noise for $T_c < T < 450$ K

To better understand the origin of 1/f noise in YBCO and extract $D(E)$, we measure the noise in a 400 nm wide, slightly overdoped ($T_c = 86$ K) YBCO nanowire (sample NW400, MgO substrate) with a constant $I_b = 1100 \mu\text{A}$ applied in the temperature range from T_c up to 450 K. From the measured values of $S_{\text{tot}}(f)$ at 10 Hz we compute $D(E)$ using eq. 6.4. In Fig. 6.4(a) we show the resulting distribution of activation energies, D , as a function of E_ω for NW400. Here we used a typical value for the inverse attempt frequency $\tau_0 = 1.2 \times 10^{-13} \text{ s}$ [158]. Since $E_\omega \propto \ln(\tau_0)$, the chosen value for τ_0 does not influence strongly E_ω . The extracted $D(E)$ shown in Fig. 6.4(a) displays a maximum at energy close to 0.9 eV, which corresponds to the activation energy for oxygen hopping in YBCO[158]. This corroborates the notion that the main mechanism for 1/f noise in our YBCO nanostructures is related to oxygen motion, causing local fluctuations of the electronic properties.

So far, we only considered the noise at high T and the connection between 1/f noise and oxygen motion, however, additional peaks can be observed in $D(E)$ for $T < 250$ K ($E_\omega < 0.6$ eV) shown in Fig. 6.4(a). These peaks can be visualized better when instead of $D(E)$, we plot the values of $S_V/V^2(T)$ extracted at $f = 10$ Hz, $S_V^{10\text{Hz}}/V^2(T)$, as shown in Fig. 6.4(b). Here, we show data obtained for two slightly overdoped nanowires: NW100 (100 nm wide, MgO substrate) and NW400 in the temperature range $300 \text{ K} > T > T_c$, where a number of minor peaks can be observed. Since the normalized PSD, S_V/V^2 , of NW400 is lower than that of NW100 due to the larger device volume, we re-scaled S_V/V^2 of NW400 by a factor 16, i.e. the ratio of the volumes of the two nanowires.

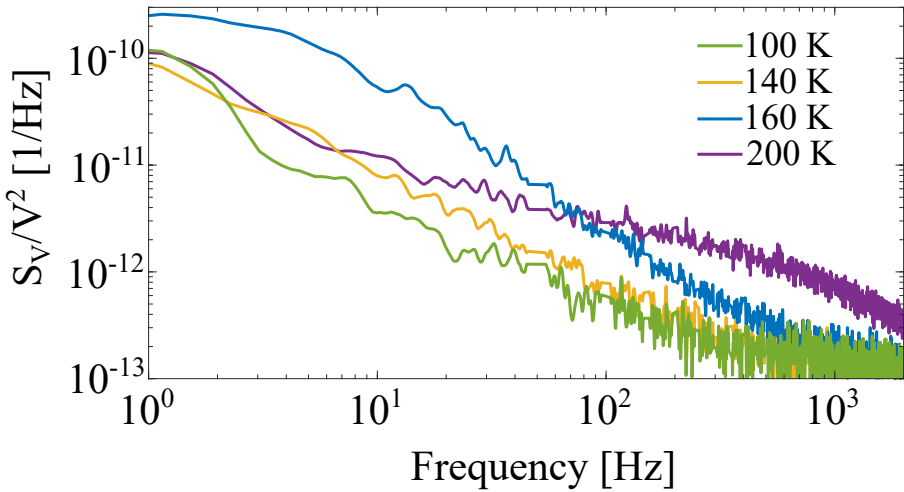


Figure 6.5: PSDs measured on NW100 at four different temperatures (corresponding to the data presented in Fig. 6.4(b)).

To understand the origin of these peaks in $S_V^{10\text{Hz}}(T)$, one can look at the evolution in temperature of the measured voltage noise spectra. In Fig. 6.5 we show the voltage noise spectra measured on NW100 at 4 different temperatures between 100 K and 200 K using a fixed bias current $I_b = 300 \mu\text{A}$. The noise spectra at $T = 100 \text{ K}$ and 140 K show the typical $1/f$ dependence. However, at $T = 160 \text{ K}$ a Lorentzian spectrum superimposed to the $1/f$ background is visible. When the temperature increases to 200 K one can observe that the position of the corner frequency of the Lorentzian, f_c , moves to higher frequencies. This indicates that the Lorentzian noise spectrum originates from a thermally activated TLF. Since the average lifetime of the TLF, τ , decreases with temperature, the amplitude of the Lorentzian noise spectrum decreases with temperature as well, see eq. 6.1. The combination of increasing corner frequency and decreasing amplitude of the Lorentzian noise spectrum with temperature results in a peak when plotting $S_V(T)$ at $f = 10 \text{ Hz}$. The temperature around which a peak is centered corresponds to the value of T for which $f_c = 1/2\pi\tau \simeq 10 \text{ Hz}$. From the above discussion it follows that the temperature around which a peak occurs depends on the frequency, f , at which we choose to extract the values of $S_V^f(T)$.

6.5 TLFs analysis

A single TLF is usually characterized by Random Telegraph Noise (RTN) in the time trace of e.g. the voltage drop across the nanowire. Here, the voltage is expected to switch between two well defined states. The mean life-time of the system in the two switching states, τ , determines the corner frequency of the Lorentzian spectrum, according to Eq. 6.1. In Fig. 6.6(a) we show a single voltage time trace corresponding to the noise spectrum measured at $T = 200 \text{ K}$ for NW100, shown in Fig. 6.5. Here, the corner frequency is roughly 700 Hz, and one would expect RTN with lifetime in the order of 250 μs . However no RTN signal, i.e. discrete switching between two states, can be discerned in the time trace.

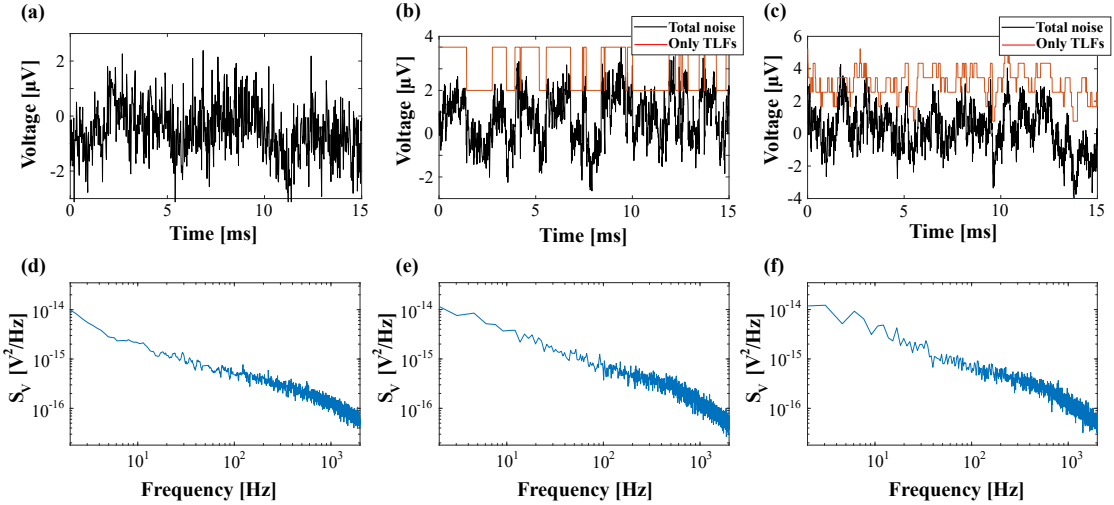


Figure 6.6: (a) Time trace corresponding to the PSD at $T = 200$ K shown in Fig. 6.5. (b) Simulated time trace of a system with $1/f$ noise and a single TLF. (c) Simulated time trace of a system with $1/f$ noise and 5 single TLFs with same E_a . (d),(e) and (f) are the PSDs obtained from the time traces shown in panel (a),(b) and (c), respectively.

To better understand the time traces in combination with the respective noise spectra measured on our nanowires, we performed numerical noise simulations. The simulations can produce time traces (voltage fluctuations versus time) of a system with $1/f$ noise plus an arbitrary number of independent TLFs. By tuning the parameters of the simulations, one can obtain time traces, which correspond to PSDs equal to or closely resembling the measured ones.

First, a system with $1/f$ noise and a single TLF is simulated, the resulting time trace is shown in Fig. 6.6(b), while the corresponding PSD is shown in Fig. 6.6(e). The latter approximates well the PSD measured at $T = 200$ K shown in Fig. 6.6(d) for comparison. However, the simulated time trace clearly shows switching behavior which is not present in the measured time trace. This suggests that the measured Lorentzian is not the result of a single TLF, but arises from an ensemble of microscopic TLFs having similar properties. To help support this, a system with $1/f$ plus 5 independent TLFs is simulated. The fluctuators are chosen to have all the same activation energies and attempt frequencies, i.e. the same τ . The resulting voltage fluctuations are shown in Fig. 6.6(c) and the corresponding PSD is shown in Fig. 6.6(f). One can see that the spectrum obtained from this simulation resembles the measured one as well. The time trace for this simulation follows the general trend of the fluctuations caused by only the TLFs (red line), however, one cannot identify clear switching events in the total time trace (black line). Therefore, the PSD of a system with a large ensemble of microscopic TLFs having similar average lifetimes τ is again a Lorentzian, as for the single TLF case, however, without displaying a characteristic RTN signal in the time trace switching between two distinct values.

This scenario can be obtained as a special case of the Dutta-Horn model: if the distribution $D(E)$ is not broad but instead very narrow in energy it can be approximated by a delta function $\delta(E_a)$ centered at the activation energy of the TLFs E_a .

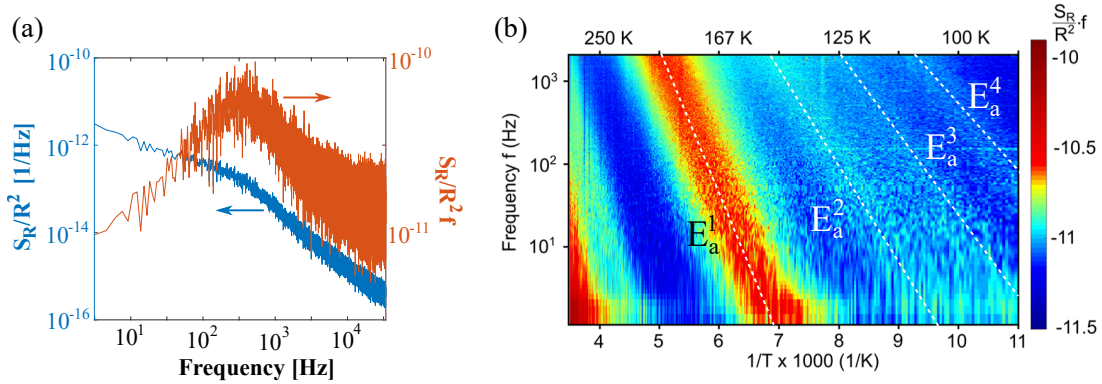


Figure 6.7: (a) Comparison of a spectrum measured spectrum (blue line) and the same spectrum multiplied by the frequency f (red line). (b) Arrhenius plot of $S_R/R^2 \times f$ measured on NW100.

Hence, the integral of eq. 6.3 is reduced to the general expression for a single thermally activated TLF. To obtain the same PSD, the voltage fluctuation amplitude of each TLF, δV , has to decrease with increasing number of TLFs, N ($\delta V \propto 1/\sqrt{N}$). Since δV decreases with increasing number of fluctuators, one eventually cannot distinguish single switching events in the time trace. From the analysis above we can conclude that in our YBCO nanowires the Lorentzian spectrum observed in noise measurements is not the result of a single TLF; it is rather the result of an ensemble of TLFs (5 or more) with very similar properties among each other.

To extract the activation energies E_a and attempt frequencies $1/\tau_0$ of the TLFs, we can analyze the evolution of the TLF corner frequency of the measured Lorentzian spectra as a function of $1/T$ (Arrhenius plot). Since the aim of this study is to understand the properties of the TLFs, the contribution of the $1/f$ noise is "minimized" by plotting $S_R/R^2 \times f$. In Fig. 6.7(a) is shown a comparison of a measured noise spectrum and the same spectrum multiplied by f . In fact, by the multiplication with f the $1/f$ contribution becomes roughly constant whereas the Lorentzian turns into a peak centered at the corner frequency. The Arrhenius plot for NW100 is shown in Fig. 6.7(b), here the amplitude of the spectra is represented in color scale as a function of frequency, f , and inverse temperature, $1/T$. Here, it is easy to observe the temperature dependence of the different TLFs. Some of the TLFs have low amplitude, barely above the $1/f$ noise level, and cannot not be distinguished in a single spectrum or from $S_V^{10\text{Hz}}(T)$. However, low amplitude features are more easily identified in a full Arrhenius plot, as shown in Fig. 6.7(b).

To extract the TLF parameters, we fit the corner frequency in the Arrhenius plot using Eq. 6.2 with fit parameters τ_0 and E_a . For the Arrhenius plot of Fig. 6.7(b) we can identify four main TLFs with activation energies $E_a^1 = 358$ meV, $E_a^2 = 254$ meV, $E_a^3 = 196$ meV and $E_a^4 = 158$ meV. The characteristic attempting frequencies, $f_0 = 1/\tau_0$, of the different TLFs are all approximately 6 THz, with $f_0^1 = 5$ THz, $f_0^2 = 6.9$ THz, $f_0^3 = 8.8$ THz and $f_0^4 = 3.8$ THz. An activation energy of 0.4 eV, which is close to E_a^1 , has been previously observed in noise measurements on YBCO nanobridges, performed by Caplan *et al.*, [152]. However, in this work they did not report the

T_c [K]	E_a^1 [meV]	f_0^1 [THz]	E_a^2 [meV]	f_0^2 [THz]	E_a^3 [meV]	f_0^3 [THz]	E_a^4 [meV]	f_0^4 [THz]
24	396	22	-	-	215	10	81	0.013
50	410	6.9	302	7.5	196	11.9	136	3.1
57	410	10	280	5.6	211	7.5	127	3.1
58	412	3.1	273	3.8	-	-	137	1.9
60	429	10	310	3.1	211	7.5	145	3.1
65	379	2.5	249	8.2	180	6.9	144	2.5
67	398	1.9	260	2.5	212	7.5	147	3.8
71	395	8.8	284	3.8	186	0.4	147	5
79	438	2.3	295	2.8	195	0.2	141	0.1
81	401	6.3	316	1.9	257	1.9	169	5.6
89	360	8.2	291	3.1	212	2.5	-	-
86	358	5	254	6.9	196	8.8	158	3.8

Table 6.1: Summary of the TLFs parameters obtained by fitting the measured Lorentzians corner frequency vs $1/T$ to eq. 6.2 (Arrhenius fit) of samples with different oxygen content (different T_c). The data corresponding to NW100 are reported in the last row, i.e $T_c = 86$ K.

presence of additional thermally activated noise sources with lower activation energies, such as those observed in our nanowires ($E_a^{2,3,4}$). The above described analysis of the observed Lorentzians has been performed on several nanowires, with lateral dimensions ranging from 100 nm up to 800 nm. This revealed that the observed TLFs in samples of different size all have very similar activation energies.

It has been shown that for epitaxially grown films, as in our case with PLD, different lattice mismatch between substrate and thin-film results in different strain induced in the film [27]. Since the strain affects the transport and superconducting properties of cuprates, we want to study if the TLFs also are affected by a change of substrate. So far we presented results obtained with YBCO deposited on MgO substrates. Therefore, we also measured the resistance noise of nanowires fabricated on STO substrates, which induces in a different strain in the YBCO film [27]. Also for these samples, we find TLFs, in the form of Lorentzians superimposed to the $1/f$ noise. The activation energies and attempt frequencies we extract by fitting the TLFs are very close to the ones extracted for samples fabricated on MgO.

In the following we study also the effect of varying oxygen doping on the TLFs. Samples with different doping levels are fabricated on STO substrates and the noise is measured as a function of T , as for the case of the slightly overdoped nanowires discussed above. To obtain nanowires with different doping, we follow the same fabrication procedure presented in Appendix A. Here, the post-annealing pressure during PLD is changed to obtain the desired Oxygen content in the deposited film [153]. Moreover, to preserve the quality of the structures, a liquid nitrogen cooled stage is used during Ar ion milling to reduce the out-diffusion of oxygen due to heating. This allows to obtain nanowires with controllable level of doping and film-like properties down to 200 nm lateral size. A summary of E_a and f_0 obtained from Arrhenius fits of the observed TLFs is reported in Table 6.1.

Also in this case, when the doping is varied, i.e. different T_c values, we obtain

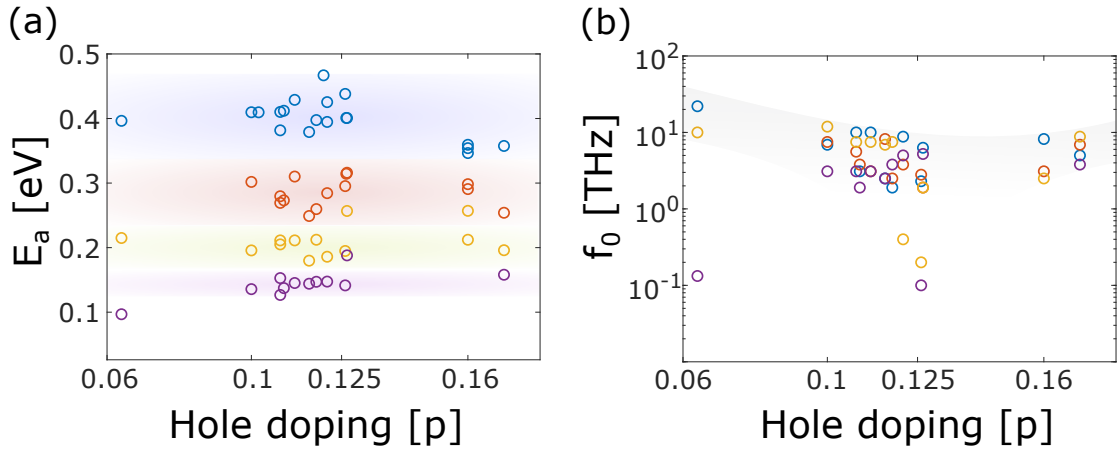


Figure 6.8: (a) Activation energies, E_a , as a function of hole doping. (b) (a) Attempt frequencies, f_0 , as a function of hole doping.

activation energies which are very similar to the slightly overdoped case. A similar behavior has been reported in the work by Caplan *et al.*, where a single activation energy close to 0.4 eV was observed in several YBCO nanowires spanning a wide range of doping. In our case, we can group TLFs with similar activation energies, thus obtaining four main TLFs which can be observed on most samples. In Fig. 6.8 we show all the activation energies extracted from samples with doping levels spanning most of the phase diagram. On the other hand, we notice a much broader distribution in characteristic attempt frequency f_0 . Indeed, while most TLFs can be fitted with values of $f_0 \simeq 6$ THz, some samples, have different values of f_0 , especially around the 1/8 doping, where the TLFs display on average lower values of attempt frequencies, f_0 , with a wider spread. This behavior might be related to the occurrence of static CDW order in YBCO around the 1/8 doping range, which might possibly have an influence of the dynamic electronic properties observed in noise measurements. However, further measurements are needed to confirm this behavior.

In summary, from our measurements we see that the resistance noise in YBCO nanostructures has some interesting, or rather unexplored, behavior at low temperatures, $T < 250$ K. We cannot exclude that the TLFs are present also at higher T , however, at these temperatures the 1/f noise increases rapidly and dominates the spectrum, so that no TLF can be detected in the noise spectra. We have fabricated and measured the resistance noise of nanowires in a wide range of different parameters, such as size, substrate material and doping, and we detect TLFs in all cases, obtaining rather consistent values of activation energies. The TLFs are most likely the result of an intrinsic property of YBCO, however, at present we do not know their origin.

The question to be answered is: could the observed TLFs be related to the dynamics of charge ordering or are they a 'boring' feature of $D(E)$. The latter could be accounted for as a special case of the Dutta-Horn model, where the ensemble of independent fluctuators have a broad distribution $D(E)$, but with local increased density around the activation energies of the TLFs. Our results exclude, however, noise arising from defects in the nanostructures due to the ubiquity and reproducibility of the TLFs

activation energies. Since one of the fundamental feature of charge ordering is the breaking of rotational symmetry we propose in the next chapter a new measurement scheme aimed at understanding if such breaking of rotational symmetry can be detected in noise measurements.

CHAPTER 7

Noise and anticorrelation

In this chapter we want to further investigate if the two level fluctuators, identified in resistance noise measurements performed on YBCO nanowires, can be related to fluctuations of some sort of local charge ordering. In the following, we first describe an experimental setup implementing cross-correlation noise measurements designed for the detection of fluctuating nematic order, which breaks rotational symmetry. The setup is inspired by a theoretical study of the local electronic order in the form of nematic patches in HTSs, which maps to the random field Ising model [149], e.g. a random resistor network, as shown in Fig. 7.1. Here the nematic order results in an in-plane anisotropy of the resistivity, i.e the resistivity has to be represented as a tensor [7]. We then introduce noise simulations to investigate what sort of signatures one can expect in cross correlated noise spectra. Here, we will assume that the total resistance noise is generated by nematic fluctuators and generic "isotropic" 1/f noise sources. In the final part of this chapter we present cross-correlation noise measurements performed on various YBCO nanowires having different lateral dimensions, and doping values.

7.1 Model

An SEM figure of a typical device designed for the detection of nematic fluctuations, plus a schematic of the etching mask, is shown in Fig. 7.2. In the following, this structure will be referred to as an X-bar. The main wire through which a bias current is flowing is patterned at angles $\Theta = 0^\circ$ or 45° with respect to the crystallographic axis ($a - b$). Since the YBCO films are twinned, each $\pi/2$ rotation of the axes is identical to the original. Along the wire, four voltage probes are patterned: V_x^\pm and V_y^\pm . These are used for the measurement of two voltage signals: $V_x = V_x^+ - V_x^-$ and $V_y = V_y^+ - V_y^-$. Since the width, $W_{x\text{bar}}$ and length, $L_{x\text{bar}}$, of the X-bar are equal, $W_{x\text{bar}} = L_{x\text{bar}}$ (see Fig. 7.2 right panel), the "directions" of the voltage signals V_x and V_y are perpendicular to each other. As for the nanowires presented in the previous chapter, we apply a constant bias current, I_b , measure the voltage fluctuations, $\delta V_{x,y}$, and compute

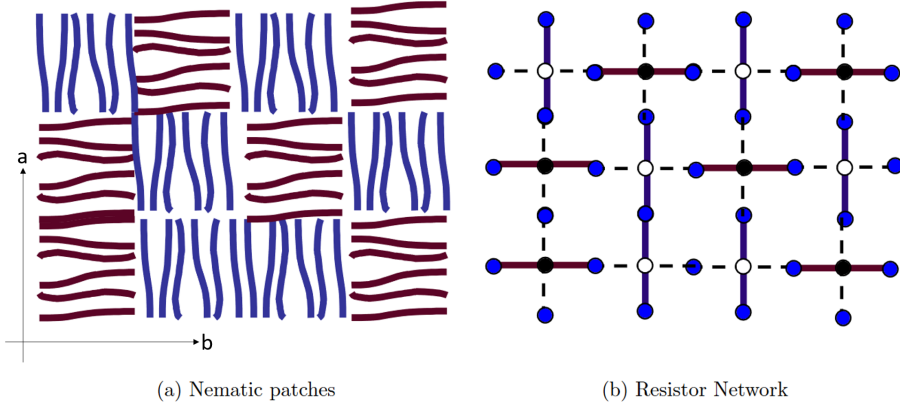


Figure 7.1: Mapping of nematic patches to a random resistor network. (a) The nematic patches align to the crystallographic a - or b -axis. The nematic order is schematically represented as 'irregular' stripes aligned to either a or b . (b) Corresponding random resistor network. Each nematic patch results in local anisotropy of the resistivity: low resistivity state, ρ_l , along the stripes (solid lines) and high resistivity, ρ_h , state perpendicular to the stripes (dashed lines). A fluctuation of a single nematic patch implies the rotation of the patch orientation by $\pi/2$ and, therefore, exchange of the high and low resistivity state in the resistor network (b). (adapted from [149])

the PSD of the two voltage signals separately, i.e. $S_{V,x} = \text{FFT}(\delta V_x) \cdot \text{FFT}(\delta V_x)^*$ and $S_{V,y} = \text{FFT}(\delta V_y) \cdot \text{FFT}(\delta V_y)^*$. Moreover, this configuration allows us also to compute the cross-correlation PSD of the two signals as $S_{V,\text{cross}} = \text{FFT}(\delta V_x) \cdot \text{FFT}(\delta V_y)^*$, i.e. the product of the FFT of δV_x and the complex conjugate of the FFT of δV_y . The cross-correlated spectrum is complex valued and, as we will show below, signatures of nematic fluctuations will be observable in both the amplitude and phase of $S_{V,\text{cross}}$. In fact, if the TLFs have a nematic nature and break rotational symmetry, the result of the cross-correlation depends on the wire orientation Θ , as will be discussed below. This is a consequence of the anisotropy in the resistivity tensor induced by a nematic patch, i.e. if the charge is arranged in stripes, the resistivity is assumed to be lower along the direction of the charge stripes, while it is higher in the perpendicular direction, as shown in Fig. 7.1. Hence, depending on the direction of the current flow with respect to the nematic orientation, one can expect a different voltage drop.

In the following, we consider the effect of a single nematic patch and assume that it is aligned either along e_a or e_b , as shown in Fig. 7.1(a) for an ensemble of nematic patches. The patch can switch stochastically between the two orientations, i.e. rotates by an angle $\pi/2$. Since we can pattern the X-bar at different angles Θ , the bias current will have different incident angle with respect to the nematic patch. In Fig. 7.3 are shown two possible scenarios depending on the orientation of I_b with respect to a nematic patch orientation.

In general, the value of the electric field vector, E , can be calculated from the resistivity tensor ρ and current density vector, j , as $E = \rho j$ [7]. We start by writing the in-plane resistivity tensor in the crystallographic $e_a([100])$, $e_b([010])$ basis, for a fixed orientation of a nematic patch (which aligns to e_a or e_b) as: $\rho = \begin{pmatrix} \rho_h & 0 \\ 0 & \rho_l \end{pmatrix}$, where

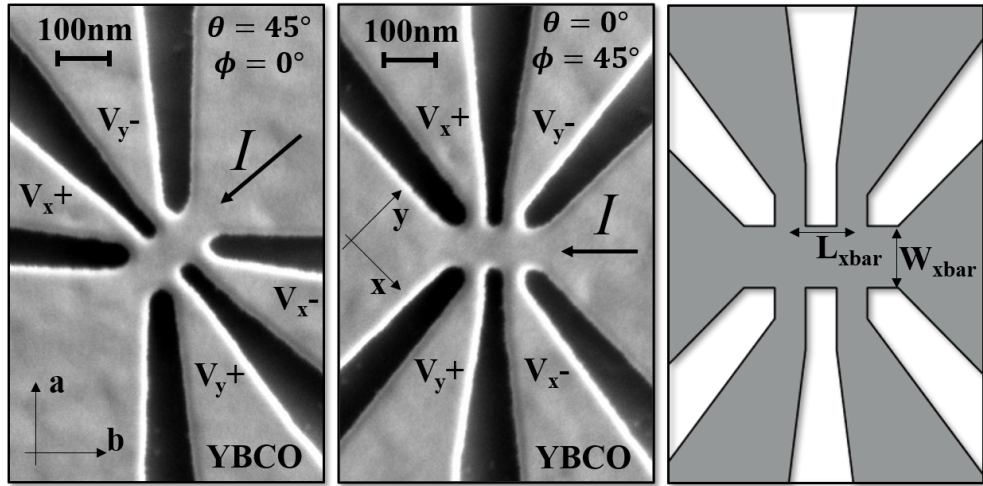


Figure 7.2: Left and centre panels: SEM pictures of two X-bars patterned with different values of Θ . In both cases, the bias current flows along the wire at angle Θ with respect to the crystallographic a - or b -axis while the voltage is measured simultaneously along V_x^\pm and V_y^\pm . The wire rotation is indicated by Θ and the angle corresponding to the measurement coordinate is given by ϕ . Right panel: Schematic of the etching mask for the X-bar design. $W_{x\text{bar}}$ and $L_{x\text{bar}}$ are the width and length of the X-bar, respectively.

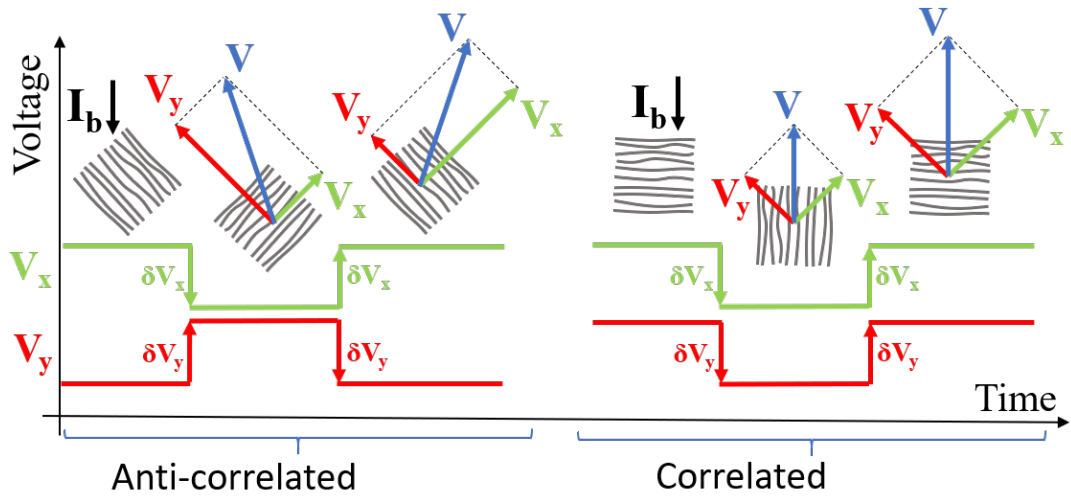


Figure 7.3: Schematic showing the effect of a nematic patch rotation on the measured voltage. (a) For the current flowing along the crystallographic [110] direction, i.e. $\Theta = 45^\circ$ and $\phi = 0^\circ$, the voltage signals along V_x and V_y are anti-correlated. (b) For the current flowing along the a - or b -direction, i.e. $\Theta = 0^\circ$ and $\phi = 45^\circ$, the voltage signals along V_x and V_y are correlated (in phase). The case for anti-correlation(a) and correlation(b) show the difference when the measurement system is rotated at an angle of $\phi = 45^\circ$ (a) or $\phi = 0^\circ$ (b) with respect to the crystallographic axes of the material. (a) and (b) correspond to the left and central panel (SEM images) of Fig.7.2, respectively.

ρ_h and ρ_l are the high and low resistivity values, respectively. When the patch changes orientation by 90° , ρ_h and ρ_l are interchanged, resulting in the tensor $\rho = \begin{pmatrix} \rho_l & 0 \\ 0 & \rho_h \end{pmatrix}$. To simplify the expression, we can write $\rho_h = \bar{\rho} + \Delta\rho$ and $\rho_l = \bar{\rho} - \Delta\rho$, where $\bar{\rho} = (\rho_h + \rho_l)/2$ and $\Delta\rho = (\rho_h - \rho_l)/2$.

One can introduce a different coordinate system e_x and e_y , which corresponds to the measuring coordinate system. Here, e_x is aligned along the direction between the V_x^- and V_x^+ voltage probes and e_y is aligned along the direction between the V_y^- and V_y^+ voltage probes (see Fig. 7.2). The new coordinate system is obtained from the e_a , e_b coordinate system (defined by crystal axes along a and b) through an in-plane rotation by an angle ϕ , such that $e_x = \hat{C}_\phi e_a$ and $e_y = \hat{C}_\phi e_b$. The angle between the e_a , e_b and e_x , e_y coordinate systems, and therefore between I_b and $V_{x,y}$, are fixed by the geometry of the X-bar: for a bias current with direction along a or b , i.e. $\Theta = 0^\circ$, we have $\phi = 45^\circ$, while for bias current diagonal to a and b , i.e. $\Theta = 45^\circ$, we have $\phi = 0^\circ$. The values for Θ and respective ϕ for the two cases are shown in Fig. 7.2.

For an arbitrary rotation of the coordinate system by an angle ϕ , the resistance tensor can be rewritten in the e_x , e_y basis as:

$$\begin{aligned}\hat{C}_\phi \rho \hat{C}_\phi^{-1} &= \begin{pmatrix} \cos\phi & -\sin\phi \\ \sin\phi & \cos\phi \end{pmatrix} \begin{pmatrix} \rho_h & 0 \\ 0 & \rho_l \end{pmatrix} \begin{pmatrix} \cos\phi & \sin\phi \\ -\sin\phi & \cos\phi \end{pmatrix} \\ &= \begin{pmatrix} \bar{\rho} + \Delta\cos(2\phi) & \Delta\rho\sin(2\phi) \\ \Delta\rho\sin(2\phi) & \bar{\rho} - \Delta\rho\cos(2\phi) \end{pmatrix}\end{aligned}\quad (7.1)$$

In our measurement scheme, the bias current always flows at an angle of 45° with respect to the axis e_x and e_y , this corresponds to $I_b = \frac{I_0}{\sqrt{2}} \begin{pmatrix} 1 \\ 1 \end{pmatrix}$, or current density $j =$

$\frac{I_0}{\sqrt{2}W_{xbar}t} \begin{pmatrix} 1 \\ 1 \end{pmatrix}$, where I_0 is the amplitude of the bias current and t is the film thickness.

The resulting voltages along e_x and e_y are $V_x = I_0(\bar{\rho} + \Delta\rho\cos(2\phi) + \Delta\rho\sin(2\phi))/t$ and $V_y = I_0(\bar{\rho} - \Delta\rho\cos(2\phi) + \Delta\rho\sin(2\phi))/t$. Here we used the fact that $V_{x,y} = E_{x,y}\sqrt{2}W_{xbar}$, since $W_{xbar} = L_{xbar}$.

The fluctuation of the single nematic patch implies the exchange of ρ_h and ρ_l . To understand the voltage fluctuations caused by the patch rotation one can introduce δV_x and δV_y as the voltage difference (fluctuation) between the two states of the patch along e_x and e_y , respectively, i.e. $\delta V_x = I_0(-2\Delta\rho\cos(2\phi) - 2\Delta\rho\sin(2\phi))/t$ and $\delta V_y = I_0(2\Delta\rho\cos(2\phi) - 2\Delta\rho\sin(2\phi))/t$. Here we made use of the fact that $\Delta\rho$ changes sign when the nematic patch rotates by 90° . In Fig. 7.3, δV_x and δV_y are shown as arrows in the time traces V_x and V_y , respectively, caused by rotations of a nematic patch.

Let's consider first the case were the wire is oriented along the a or b axis with the two voltage probe pairs rotated by 45° from the in-plane crystallographic axes, i.e. $\phi = 45^\circ$, (see Fig. 7.2(right panel)). From the above considerations it follows that $V_x = V_y = I_0(\bar{\rho} + \Delta\rho)/t$. In this situation, if the nematic patch rotates and $\Delta\rho$ changes sign, the change in the voltage is equal along the two measurement coordinates: $\delta V_x = \delta V_y = -I_0\Delta\rho/t$. This correspond to the "correlated" case shown in

Fig. 7.3(b). On the other hand, when the voltage probe pairs are aligned with the in-plane crystallographic axes ($\phi = 0^\circ$), i.e. the wire and bias current are oriented along the diagonal of a and b , then $\delta V_x = -\delta V_y = -2I_0\Delta\rho/t$ or $\delta V_x = \delta V_y e^{i\pi}$. This means that if a nematic patch flips its orientation the voltage changes along the two voltage probe pairs, however, δV_x and δV_y have opposite signs. This can also be understood when considering the total voltage vector, V , which is not aligned with I_b when the current direction is not aligned with the principal axes of the nematicity or resistance tensor. Hence, V has different projections on e_x and e_y ($V_x \neq V_y$). This is the "anti-correlated" case shown in Fig. 7.3(a).

From Fig. 7.3, we can see that the stochastic dynamic of a nematic patch would result in a RTN signal in the voltage time traces $V_x(t)$ and $V_y(t)$. In the following we assume that the underlying process of the stochastic nematic patch orientation switching can be mapped onto a double well potential model with thermally activated behavior, see inset of Fig. 6.4(a), where the two local minima would correspond to the two different patch orientations. Assuming that the dimensions of the nematic patch are below 10 nm, as is the case of CDW order[6], an X-bar with $W_{x\text{bar}} = L_{x\text{bar}} = 100$ nm would contain an ensemble of at least 100 fluctuators. As shown in section 6.5, if this ensemble of TLFs have a narrow distribution of activation energies, E_a , and attempt frequencies, $1/\tau_0$, the result noise spectrum of such a voltage time trace would have a Lorentzian shape.

Within this model framework, we would expect the noise measured on X-bars to have the following features. The PSDs of the time traces V_x and V_y computed separately, $S_{V,x}$ and $S_{V,y}$, wouldn't differ from the results described in the previous chapter, i.e. Lorentzians superimposed to the $1/f$ noise with corner frequencies proportional to the inverse average life times of the two nematic patch orientations. The advantage of an X-bar is the possibility of calculating the cross-correlation of the voltage signals, $S_{V,\text{cross}}$. Generally, the cross-correlation of two spectra can be used to compare the likeness of the two noise signals. Moreover, the phase of the cross-correlated spectrum holds information on the phase difference between the noise signals. While the PSD of δV_x and δV_y are expected to be almost identical, their cross-correlation reveals important information on the nature of the TLFs. In particular, for correlated signals, one would expect a phase in the cross-correlated spectrum close to zero, while, in the anti-correlated case, we can expect phase values close to $\pm\pi$.

7.2 Simulations

In the following, we will study the effect of nematic fluctuations on the expected cross-correlated noise taking into account also the "omnipresent" $1/f$ background noise. Here, we can use the same program employed in the previous chapter to simulate a system with $1/f$ noise plus an arbitrary number, N , of TLFs. Here, we can generate two voltage signals, $\delta V^{1/f}$ and $\delta V_{x,y}^{\text{TLF}}$, which correspond to the voltage fluctuations due to $1/f$ noise and TLFs, respectively. We can use these signals to simulate the voltage fluctuations of a system along two perpendicular axes, δV_x and δV_y , as:

$$\delta V_{x,y} = \delta V^{1/f} + \delta V_{x,y}^{\text{TLF}} \quad (7.2)$$

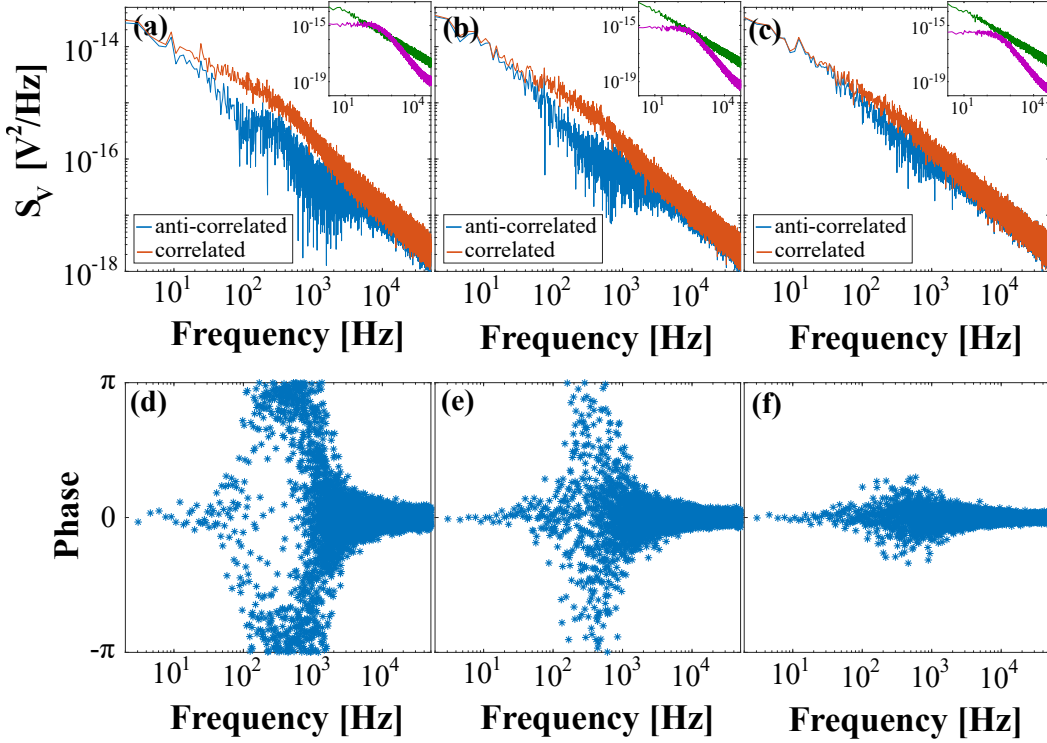


Figure 7.4: (a),(b),(c) Comparison of the PSD (absolute values) obtained from simulations in the case of anti-correlated (blue line) and correlated (red line) TLFs. The simulations are done with increasing magnitude of the TLFs (Lorentzian) with respect to the 1/f noise. For comparison, in the insets of panel (a),(b) and (c) we show the separate spectra of the TLFs (violet line) and 1/f noise (green line) used in the simulations. (d),(e),(f) Phase of the cross-correlated spectra shown in panel (a),(b) and (c), respectively, assuming anti-correlated TLFs.

Since the 1/f noise is assumed to be isotropic, $\delta V^{1/f}$ is the same along x and y . To simulate a correlated system ($\phi = 45^\circ$) we set $\delta V_x^{\text{TLF}} = \delta V_y^{\text{TLF}}$, while to simulate anti-correlation ($\phi = 0^\circ$), we set $\delta V_x^{\text{TLF}} = -\delta V_y^{\text{TLF}}$.

For the simulations, we choose a the total number of TLFs $N = 5$, although the results can be extended to any arbitrary number N . Different simulations are performed using the same amplitude for $\delta V^{1/f}$, i.e the same level of 1/f noise, while the amplitude for $\delta V_{x,y}^{\text{TLF}}$ is varied. The results for three different systems are shown in Fig. 7.4. In panel (a), (b) and (c) we show the PSDs obtained for systems where the TLFs cause anti-correlated noise (blue lines) and compare them to the PSDs where the TLFs result in correlated noise (red lines). In the insets of these panels, we show the noise (Lorentzian and 1/f) obtained separately from $\delta V^{1/f}$ and $\delta V_{x,y}^{\text{TLF}}$ to compare their magnitudes. In the first simulation, Fig. 7.4(a), the magnitude of the Lorentzian is higher than that of the 1/f noise in the frequency interval from 100 Hz to 1 kHz. In the case where the TLFs result in correlated noise the total PSD (red line in Fig. 7.4(a),(b),(c)) is just the sum of the two individual PSDs (insets in Fig. 7.4(a),(b),(c)). In fact the PSD obtained for the correlated noise case is the same as the PSD of the individual time traces δV_x and δV_y . However, for the case where the TLFs cause anti-correlated noise, the total PSD differs quite drastically from the previous case. In fact, the PSD has a local maximum at the corner frequency of the Lorentzian. Moreover two local

minima occur in the total PSD around 100 Hz and 1 kHz where the individual PSDs (Lorentzian and 1/f) are crossing each other. Here the two individual contributions have the same amplitude causing the suppression of the total PSD. In panel (b), the Lorentzian PSD is never above the 1/f noise, albeit having the same value close to the corner frequency. Also in this case we observe a suppression of the total PSD. In panel (c), the amplitude of the Lorentzian is well below the level of the 1/f noise. However, one can still see a suppression of the anti-correlated PSD close to the corner frequency of the Lorentzian. These simulations show that there are specific signatures in the PSD of cross-correlated signals if the latter are anti-correlated. Thus, if the TLFs break the rotational symmetry, resulting in anti-correlated noise, we can expect a change in the PSD as compared to the PSD calculated from the single voltage signals separately.

The phase of the cross-correlated noise spectrum also holds informations which can help to understand the nature of the TLFs. The phase extracted from the cross-correlated noise spectra assuming anti-correlated TLFs from Fig. 7.4(a),(b) and (c), are shown in Fig. 7.4(d),(e) and (f), respectively. In those panels, one can see that when the 1/f noise dominates the spectrum, the phase assumes values close to 0, as expected for correlated and isotropic noise. In the frequency range where the Lorentzian dominates over the 1/f noise, the phase departs from 0 and assumes values close to $\pm\pi$. The spread of the phase values, i.e. the width of the phase distribution, either around 0 or $\pm\pi$, depends on the number of averages used in the simulations. A higher number of averages, results in narrower distribution of the phase, however, we observed that the distribution width of the phase values decreases logarithmically with the number of averages. In our simulation, we use 20 averages, which is also used for the measurements, which are discussed below. This number of averages is enough to show rather clearly if anti-correlated noise is present or not. The signature of anti-correlation (phase values equal $\pm\pi$) can be seen more clearly in panel (d) where the amplitude of the Lorentzian is above the 1/f noise in the frequency interval from 100 Hz to 1 kHz. In panel (e), where the the TLFs noise magnitude is equal to the 1/f noise value close to the corner frequency of the Lorentzian, the phase diverges towards $\pm\pi$ only for a narrow frequency interval. In the last case (i.e. panel (f)), the Lorentzian is never above the 1/f noise and the phase does not reach $\pm\pi$. However, we can still see the effect of an anti-correlated signals by the broad distribution around zero phase for frequencies close to the corner frequency of the Lorentzian.

From the simulations, we can conclude that if the TLFs are the result of nematic fluctuations, and therefore break the rotational symmetry, we should expect signatures in the cross-correlation spectrum (both amplitude signal and phase signal). The phase of the cross-correlated noise spectrum should assume values close to $\pm\pi$. Moreover, the noise spectra for the signals δV_x and δV_y taken separately, $S_{V,x}$ and $S_{V,y}$, have the same shapes as for the PSD in the correlated case, i.e. a Lorentzian superimposed to the 1/f noise. However, the shape of the cross-correlated PSD, $S_{V,cross}$, should differ from $S_{V,x}$ and $S_{V,y}$, if the two noise signals contain both correlated and anti-correlated contributions. Therefore, under the assumption that the fluctuating nematic patches align only along the crystallographic axes, we should only observe signatures of anti-correlated noise in the case were the wire (bias current) is aligned along the crystallographic [110] direction, i.e. $\Theta = 45^\circ$.

7.3 Results

The resistance noise versus temperature of several X-bars has been measured with the scheme introduced above, i.e measuring simultaneously δV_x and δV_y . The X-bars have been patterned with either angle $\Theta = 45^\circ$ or $\Theta = 0^\circ$, with different dimensions ($W_{x\text{bar}}$ and $L_{x\text{bar}}$), and with varying doping levels. For all samples, when computing $S_{V,x}$ and $S_{V,y}$, the noise is consistent with the results obtained on the nanowires, i.e. we observe TLFs with similar values of E_a and τ_0 discussed in chapter 6. On the other hand, when computing $S_{V,\text{cross}}$, we find that in some cases the cross-correlated spectra show the signatures of anti-correlated noise (local minima in the PSD and $\pm\pi$ phase) predicted by the model and simulations presented above. However, we often observe that in the same device only a subset of the observed Lorentzians show signatures of anti-correlated noise, whereas the other Lorentzians display fully correlated noise. Furthermore, we find these anti-correlation signatures for both angles $\Theta = 45^\circ$ and $\Theta = 0^\circ$, which indicates that the nematic patches might not align only to the crystal axes, as we assumed. In the following, we present some exemplary measurements obtained for underdoped and for slightly overdoped samples.

Starting with the results obtained for underdoped X-bars, we see that the cross-correlated noise may differ a lot between different samples. However, some of the measured X-bars show distinct anti-correlation features in both phase and amplitude of the cross-correlated spectra. As an example, the noise measured on an X-bar, which has $W_{x\text{bar}} = L_{x\text{bar}} = 200$ nm, $\Theta = 45^\circ$, and $T_c \simeq 24$ K, is shown in Fig. 7.5. In panel (a), we show the absolute value of the phase of the cross-correlated noise in an Arrhenius plot. Here, the color scale indicates the value of the phase as a function of f and $1/T$. The phase has values close to 0 (blue color, correlated) in almost the full temperature and frequency range, while it shows values close to $\pm\pi$ (yellow and red color, anti-correlated) in a narrow line in correspondence of a Lorentzian observed in the PSD of the single voltage channel. In Fig. 7.5(b), upper panel, we show a comparison between $S_{V,\text{cross}}$ (blue line) and $S_{V,x}$ (red line) measured at $T = 140$ K. In the lower panel of Fig. 7.5(b) we show the phase spectrum of the cross-correlated noise at $T = 140$ K. In these plots (upper and lower panel of Fig. 7.5(b)), we can see rather clearly the signatures of anti-correlated noise, as shown in the simulations: 1) $S_{V,\text{cross}}$ has a minimum at the corner frequency of the Lorentzian, f_c , in contrast to $S_{V,x}$, which has a Lorentzian superimposed to the $1/f$ noise, and 2) the phase assumes values close to $\pm\pi$ for frequencies close to the corner frequency, f_c , and it is 0 where the $1/f$ noise dominates the spectrum. However, in Fig. 7.5(a) we see anti-correlation only for one TLF. Other Lorentzians are present in the noise spectra, similarly to Fig. 6.7(b), but do not show anti-correlation. Moreover, such clear signatures of anti-correlation are not always observable among different samples having the same size and critical temperature T_c .

According to the model, we would expect anti-correlation only for X-bar patterned at angle $\Theta = 45^\circ$, but we find the same signatures also for X-bars patterned at angle $\Theta = 0^\circ$. This suggests that the nematicity is not strictly aligned with the crystallographic axes. If the nematicity could indeed align freely in the ab -plane of YBCO, it would explain why the signatures of anti-correlation are not reproducible among different

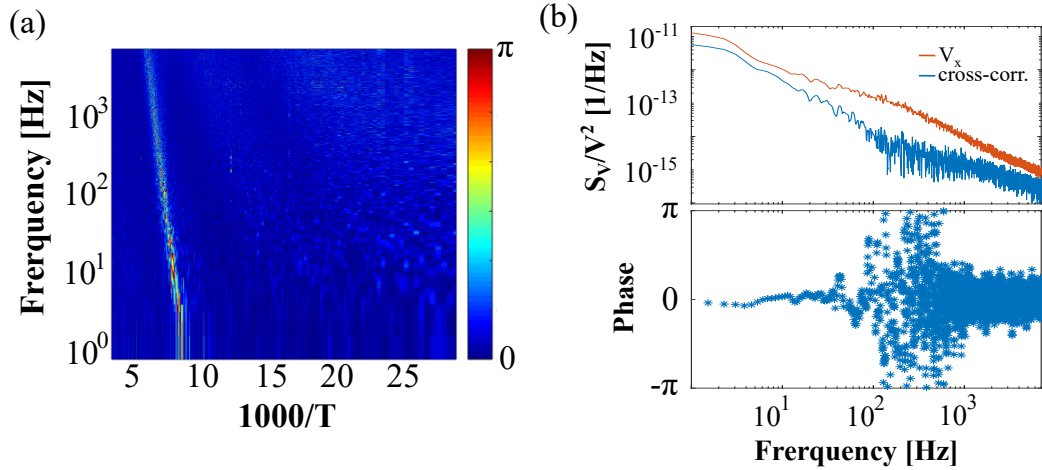


Figure 7.5: (a) Arrhenius plot of the phase of cross-correlated noise spectrum measured on a 200 nm wide X-bar with $T_c = 24$ K. (b) upper panel: comparison between the absolute value of $S_{V,\text{cross}}$ (blue line) and $S_{V,x}$ (red line) obtained at $T \approx 140$ K. Lower panel, phase spectrum of the cross-correlated noise measure at $T \approx 140$ K.

samples and can be detected for both $\Theta = 0^\circ$ and $\Theta = 45^\circ$. However, the assumption of nematic stripes aligned to the crystal axes was based on the observation made for (quasi-)static CDW. The models for fluctuating stripes, see section 2.2, do not necessarily require these dynamic nematic align along specific directions.

In the underdoped case shown above, signatures of anti-correlation have been observed in samples with W_{xbar} and L_{xbar} as large as 400 nm. On the other hand, for optimally- and slightly over-doped X-bars, the presence of the signatures of anti-correlated noise depends on the dimensions of the X-bar. When W_{xbar} and L_{xbar} are ≥ 200 nm, the cross-correlated PSD and phase of the X-bar did not show any signatures of anti-correlation, and all observed Lorentzians seem to be the result of correlated noise sources. However, when W_{xbar} and L_{xbar} are reduced to 100 nm, the phase of the cross-correlated noise changes drastically. The noise measured on a slightly overdoped YBCO X-bar ($T_c = 86$ K), with $\Theta = 0^\circ$ and $W_{\text{xbar}} = L_{\text{xbar}} = 100$ nm, is shown in Fig. 7.6. In panel (a) we use an Arrhenius plot to show the absolute value of the phase of the cross-correlated noise spectra. Here, the phase values are randomly spread between $\pm\pi$ for $f > 1$ kHz (see also Fig. 7.5(b), lower panel), as expected for the uncorrelated white input noise of the two voltage amplifiers, i.e. the white noise of the amplifiers, which dominates the spectra at high frequencies. At lower f , we can see that the phase assumes values close to 0 in most of the f and T range. Similar to the noise data shown in Fig. 7.5, we can identify regions where the phase of the cross-correlated spectra approaches $\pm\pi$ (see white dashed lines in Fig. 3.5 (a)). In Fig. 7.6(b), upper panel, we show the comparison between $S_{V,\text{cross}}$ (blue line) and $S_{V,x}$ (red line) measured at $T \approx 105$ K, while in the lower panel we show the phase spectrum of the cross-correlated noise at the same temperature. As for the underdoped case (Fig. 7.5(a)), we can see the signatures of anti-correlated noise.

In summary, some of the Lorentzians observed in the resistance noise spectra of

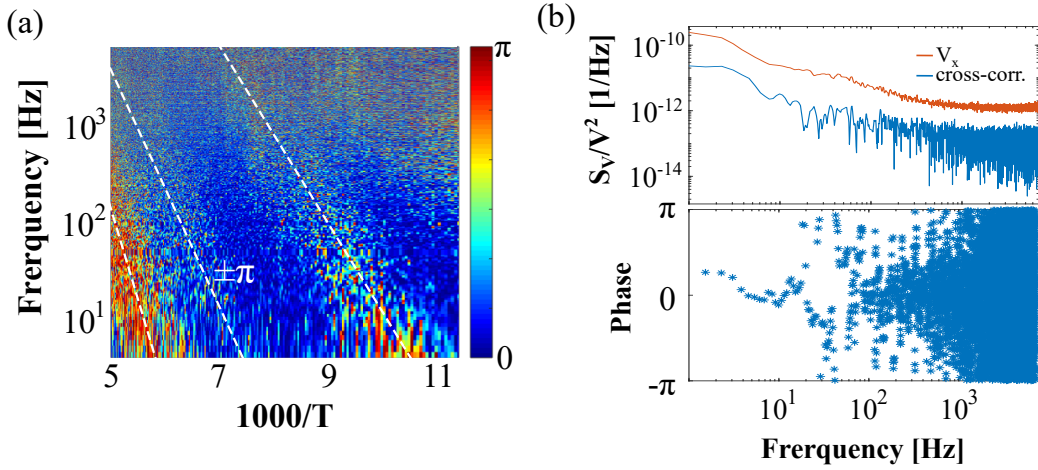


Figure 7.6: (a) Arrhenius plot of the phase of the cross-correlated noise spectrum measured on a 100 nm wide, slightly overdoped YBCO X-bar. The white, dashed lines indicate regions where phase approaches $\pm\pi$. (b) upper panel: comparison between the absolute value of $S_{V,\text{cross}}$ (blue line) and $S_{V,x}$ (red line) obtained at $T \simeq 105$ K. Lower panel, phase spectrum of the cross-correlated noise measure at $T \simeq 105$ K.

YBCO nanowires show strong indications that the underlying noise mechanism is related to the fluctuations of nematic patches. However, a preferential alignment of the nematic patches along the crystallographic *a*- and *b*-axis, similar to the one of CDW order observed in x-ray scattering experiments, could not be confirmed. Further experimental investigations, implementing orienting fields such as strain, electric and magnetic fields, will be required to further understand the microscopic nature of the ubiquitous two level fluctuators observed in YBCO nanostructures over a wide temperature and doping range.

CHAPTER 8

Conclusions

While the field of HTS is now more than 30 years old, the scientific interest of these materials is still at the forefront of research in condensed matter physics. The open questions regarding cuprates are challenging researchers to piece together the different phases and orders characteristic of these materials.

In this thesis work we have investigated the noise properties of cuprate HTS YBCO nanoscale devices. Here, the aim was twofold: 1) To get a better understanding of nanoscale fluctuations in the normal state of HTS, from which superconductivity might evolve. 2) To develop a new kind of YBCO weak link for the realization of a sensitive magnetometer going beyond the state-of-the-art. In these respects, we implemented YBCO nanodevices as tools to obtain new experimental signatures, which can deliver new insights about the complex properties of HTS materials, and as building blocks, i.e. weak links, for the realization of low noise HTS magnetometers.

In the first part of the thesis, we introduced a new type of superconducting weak link, the nanoscale YBCO grooved Dayem bridge. By tuning the width, W , and length, L , of the grooved nanogap, we find that the best performance, in terms of critical current and differential resistance, are obtained for $L = 50$ nm and $W = 200$ nm, with $I_c = 10 \mu\text{A}$ and $\delta V/\delta I = 20 \Omega$. The limiting factors of nanobridges, such as high critical current density, j_c , high parasitic kinetic inductance, L_{kin} , and low differential resistance, δR , are solved in GDBs, resulting in enhanced SQUID performance, i.e. low magnetic flux white noise $S_\Phi^{1/2} = 6 \mu\Phi_0/\sqrt{\text{Hz}}$. The GDBs were also integrated in SQUIDs coupled to an in-plane pickup loop. Magnetic field noise values as low as $63 \text{ fT}/\sqrt{\text{Hz}}$ at $T = 77$ K were obtained. This noise performance is comparable to state-of-the-art HTS magnetometers based on conventional grain boundary junctions.

The promising results obtained with GDB-based SQUIDs, make these device interesting for future applications. Moreover, the novelty of these weak links leave a wide

margin for future improvements. In this respect, we will focus in the future on the fabrication of a series of GDB-based magnetometer for application in a 7-channel magnetoencephalography system. Meanwhile, the GDB will be further improved following the consideration given in section 5.5, i.e. multiple gaps GDB and electromigration for the fine tuning of the device properties.

In the second part of the thesis, we studied resistance noise properties of YBCO nanowires as a function of temperature and hole doping. We first characterized the $1/f$ noise, which is related to oxygen hopping in the material. However, our measurements revealed also the presence of distinct Lorentzians superimposed to the $1/f$ background noise. From the analysis of the voltage time traces we conclude that the Lorentzians are the result of an ensemble of two level fluctuators having similar activation energies E_a and characteristic attempt frequencies $1/\tau_0$. Moreover, we have fabricated and measured the resistance noise of nanowires in a wide range of different parameters, such as size, substrate material and doping, and we detect these TLFs in all cases, obtaining rather similar values of activation energies among all devices. Finally we propose a novel measurement scheme to probe if the observed Lorentzians in the noise spectra are related to electronic nematic fluctuations. Indeed, we observed indications of nematic fluctuations, that is local time dependent fluctuations of the in-plane conductivity anisotropy, in a wide temperature range above the superconducting transition. The observed fluctuations could be related to so-called charge stripe fluctuations, which represent a possible microscopic mechanism for superconductivity in these materials. However, further experimental investigations will be required to further understand the microscopic nature of those two level fluctuators. Such studies will involve the implementation of orienting fields for the nematic order such as strain, electric and magnetic fields.

APPENDIX A

Nanowire fabrication

In the following are reported the fabrication steps and parameters which are used to obtain YBCO nanowires. A schematic of the process is reported in Fig. A.1. First, a thin film of YBCO is epitaxially grown by Pulsed Laser Deposition (PLD) on different choices of substrate, Fig. A.1(a). The latter is chosen according to the epitaxial requirements of YBCO and in this work both substrates of MgO (110) or STO (001) have been used. The PLD process involve ablation of a bulk target of YBCO by high energy laser pulses, this process maintains the stoichiometry of the ablated material. The laser ablation generates a plasma plume and the substrate is positioned to be in the top part of this plume. The YBCO is deposited in a O₂ environment at fixed pressure p_{dep} .

The advantages of PLD lie in the high tunability of the deposition parameters and the flexibility of the process. In fact, all conditions can be varied to optimize the deposition of YBCO on different substrates, for different thicknesses and doping levels. However, the plasma plume size limits the maximum substrate lateral dimensions for which we can achieve uniform YBCO thin-films. In particular, the PLD system in the nanofabrication laboratory here at Chalmers university, which we use to deposit our YBCO thin-films, has lateral dimension of the plasma plume of 6-7 mm. This limits the maximum substrate dimensions for thin-films with uniform, pristine quality to 10×10 mm². A summary of the PLD parameters used to obtain optimally to slightly-

Substrate	T_{dep} [°C]	p_{dep} [mbar]	height [mm]	E_{laser} [mJ]	p_{post} [mbar]	t_{YBCO} [nm]
MgO (110)	740	1.2	54	55	1.2	50
STO (001)	775	1.2	58	58	1.2	50

Table A.1: Summary of the deposition conditions for slightly-overdoped YBCO thin-films. T_{dep} is the deposition temperature of the substrate, p_{dep} and p_{post} are the deposition and post-annealing pressure, respectively, height is the distance between substrate and YBCO target, E_{laser} is the energy of the laser (the laser spot is fixed and have an area of 4 mm²), and t_{YBCO} is the thickness of the YBCO thin-film.

A. Nanowire fabrication

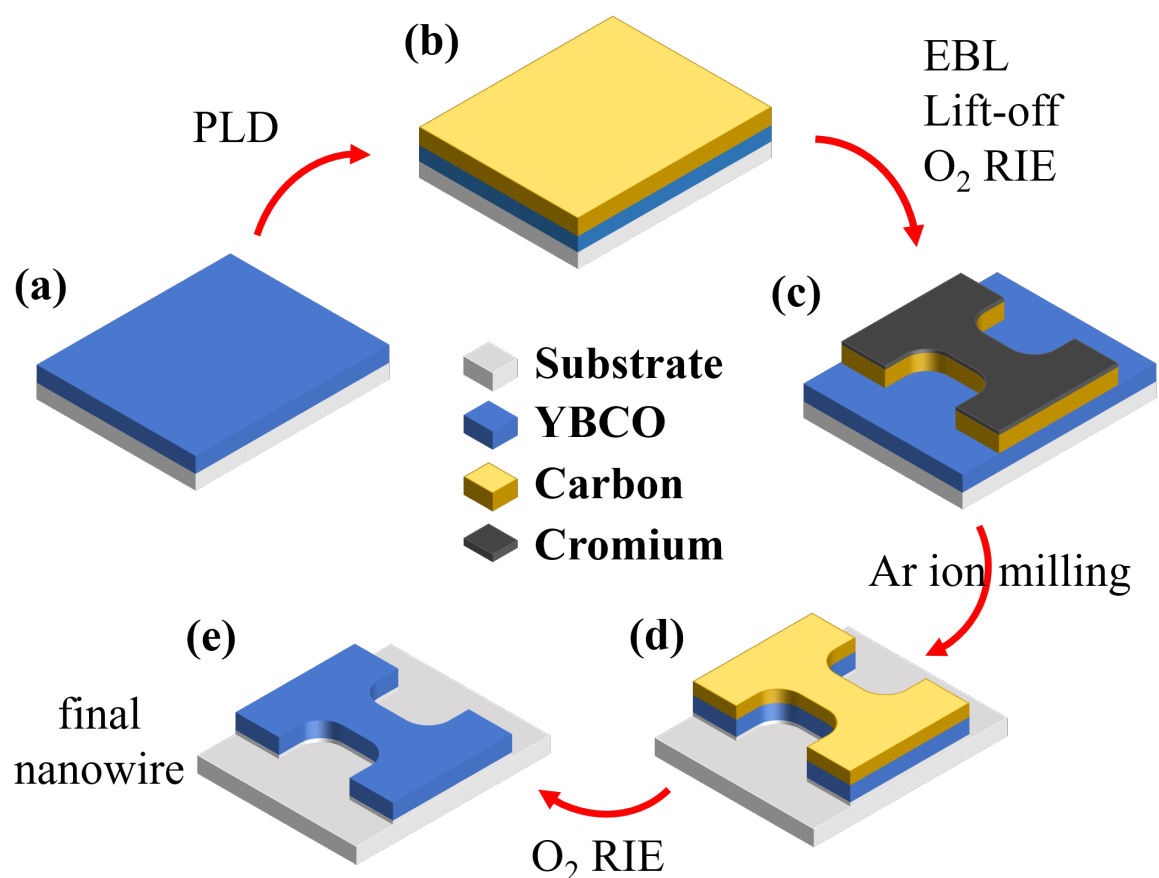


Figure A.1: Schematic of the main steps necessary to the fabrication of YBCO nanostructures

T_{dep} [$^{\circ}\text{C}$]	p_{dep} [mbar]	height [mm]	E_{laser} [mJ]	t_{C} [nm]
30	$3.4 \cdot 10^{-4}$	50	100	100

Table A.2: Summary of the deposition conditions for the carbon mask. T_{dep} is the deposition temperature, p_{dep} is the deposition pressure, respectively, height is the distance between substrate (YBCO thin film) and C target, E_{laser} is the energy of the laser (the laser spot is fixed and have an area of 4 mm^2), and t_{C} is the thickness of the carbon mask.

V_{beam} [V]	I_{beam} [mA]	j_{beam} $\mu\text{A}/\text{cm}^2$	I_{neutr} [mA]	Ar^+ flow [sccm]	etch rate [nm/min]	stage tilt
300	2	30	50	5	0.8	5°

Table A.3: Summary of the main parameters used for the Ar^+ ion milling process. V_{beam} is the acceleration voltage, I_{beam} and j_{beam} are the current and current density of the ion beam, respectively, and I_{neutr} is the neutralizer current

overdoped 50 nm thick films of YBCO is reported in Table A.1, for both MgO and STO substrates.

After the deposition of YBCO, an amorphous thin film of hard (diamond-like) Carbon is deposited in a different PLD system, Fig.A.1(b). The film is deposited at room temperature with thickness $t_{\text{C}} = 100 \text{ nm}$. The Carbon is going to act as a hard mask during the final step of Ar^+ ion milling, protecting the underlying layer of YBCO. This step does not influence the quality of the YBCO thin film. A summary of the parameters used for this step of PLD are reported in Table A.2

The next step is the definition of the device mask with Electron Beam Lithography (EBL), Fig. A.1(c). Here, a double layer of electron beam resist (e-resist) is spinned on top of the Carbon film. The two layers are MMA8.5 MAA EL4 (bottom) ans AR-P6200:IPA 1:3 (top), both are spinned at 6000 rpm and baked for 5 minutes at 95°C . Higher baking temperature may result in degradation of the YBCO thin film. The CAD mask is exposed with a JEOL JBX 9300FS with electron acceleration voltage of 100 kV, the minimum beam spot size is 4 nm, resulting in well-defined structures down to 30 nm feature size. The e-resists are developed for 35 seconds using Oxylene 96 % and MIBK:IPA 1:3 both at room temperature. After, 12 nm of Chromium are evaporated by electron beam Physical Vapour Deposition and subsequently lift-off in a bath of developer 1165 pre-warmed at 73°C for a total time of 10 minutes, followed by ultra-sonication. Here, the double e-resist layer improves the lift-off final result thanks to the undercut formed during development.

The Chromium mask is transferred to the Carbon layer by O_2 plasma Reactive Ion Etching (RIE). The RIE uses a power of 50 W and O_2 pressure of 100 mTorr. These parameters, while completely etching the Carbon, do not degrade the quality of the YBCO. After, the sample is loaded in an Ar^+ ion milling etching machine and etched with a ion current density, j_{beam} , of $30 \mu\text{A}/\text{cm}^2$. The main parameters used during this step are reported in Table A.3. A neutralizer is used to increase the coherence of the ion beam, avoid charging effect of the substrate and improved the fidelity of the etching mask. The etching stage rotates during etching and has two cooling options: water cooled to 18°C (used for optimally to slightly overdoped samples) and LN_2 cooled (used for underdoped samples).

A. Nanowire fabrication

Finally, the carbon mask, which is left after the Ar^+ ion milling, is removed by RIE, Fig. A.1, using the same etching parameters as for the previous RIE step.

Bibliography

- [1] H. Kamerlingh Onnes. “The resistance of pure mercury at helium temperatures”. *Commun. Phys. Lab. Univ. Leiden*, b 120 (1911).
- [2] J. G. Bednorz and K. A. Müller. “Possible highT c superconductivity in the Ba- La- Cu- O system”. *Zeitschrift für Physik B Condensed Matter* 64.2 (1986), pp. 189–193.
- [3] J. Zaanen et al. “Towards a complete theory of high Tc”. *Nature Physics* 2.3 (2006), pp. 138–143.
- [4] V. Emery and S. Kivelson. “Importance of phase fluctuations in superconductors with small superfluid density”. *Nature* 374.6521 (1995), p. 434.
- [5] J. Zaanen et al. “Planckian dissipation, minimal viscosity and the transport in cuprate strange metals”. *SciPost Physics* 6 (2019), p. 061.
- [6] G. Ghiringhelli et al. “Long-range incommensurate charge fluctuations in (Y, Nd) Ba₂Cu₃O_{6+x}”. *Science* 337.6096 (2012), pp. 821–825.
- [7] J. Wu, A. Bollinger, X. He, and I. Božović. “Spontaneous breaking of rotational symmetry in copper oxide superconductors”. *Nature* 547.7664 (2017), p. 432.
- [8] R. Arpaia, M. Arzeo, S. Nawaz, S. Charpentier, F. Lombardi, and T. Bauch. “Ultra low noise YBa₂Cu₃O_{7-δ} nano superconducting quantum interference devices implementing nanowires”. *Appl. Phys. Lett.* 104.7 (2014), p. 072603.
- [9] M. Arzeo, R. Arpaia, R. Baghdadi, F. Lombardi, and T. Bauch. “Toward ultra high magnetic field sensitivity YB₂C_u3O_{7-δ} nanowire based superconducting quantum interference devices”. *J. Appl. Phys.* 119.17 (2016), p. 174501.
- [10] M. Xie et al. “Improved coupling of nanowire-based high-T c SQUID magnetometers—simulations and experiments”. *Supercond. Sci. Tech.* 30.11 (2017), p. 115014.
- [11] W. Meissner and R. Ochsenfeld. “Ein neuer effekt bei eintritt der supraleitfähigkeit”. *Naturwissenschaften* 21.44 (1933), pp. 787–788.
- [12] F. London and H. London. “The electromagnetic equations of the supraconductor”. *Proceedings of the Royal Society of London. Series A-Mathematical and Physical Sciences* 149.866 (1935), pp. 71–88.
- [13] V. Ginzburg and L. Landau. “On the Theory of superconductivity”. *Zh. Eksp. Teor. Fiz.* 20 (1950), p. 1064.
- [14] J. Bardeen, L. N. Cooper, and J. R. Schrieffer. “Theory of superconductivity”. *Physical review* 108.5 (1957), p. 1175.
- [15] M. Tinkham. *Introduction to superconductivity*. Courier Corporation, 2004.
- [16] M.-K. Wu et al. “Superconductivity at 93 K in a new mixed-phase Y-Ba-Cu-O compound system at ambient pressure”. *Physical review letters* 58.9 (1987), p. 908.
- [17] J. R. Waldram. *Superconductivity of metals and cuprates*. CRC Press, 2017.
- [18] T. Sekitani, N. Miura, S. Ikeda, Y. Matsuda, and Y. Shiohara. “Upper critical field for optimally-doped YBa₂Cu₃O_{7-δ}”. *Physica B: Condensed Matter* 346 (2004), pp. 319–324.
- [19] A. Abrikosov. “The magnetic properties of superconducting alloys”. *Journal of Physics and Chemistry of Solids* 2.3 (1957), pp. 199–208.

- [20] W. E. Pickett. "Electronic structure of the high-temperature oxide superconductors". *Reviews of Modern Physics* 61.2 (1989), p. 433.
- [21] Y. Tokura and T. Arima. "New classification method for layered copper oxide compounds and its application to design of new high T_c superconductors". *Japanese journal of applied physics* 29.11R (1990), p. 2388.
- [22] H. Smilde et al. "Admixtures to d-wave gap symmetry in untwinned YBa₂Cu₃O₇ superconducting films measured by angle-resolved electron tunneling". *Physical review letters* 95.25 (2005), p. 257001.
- [23] C. Villard, G. Koren, D. Cohen, E. Polturak, B. Thrane, and D. Chateigner. "ab-Plane Anisotropy of Transport Properties in Unidirectionally Twinned YBa₂Cu₃O_{7-δ} Films". *Physical review letters* 77.18 (1996), p. 3913.
- [24] D. Basov et al. "In-Plane Anisotropy of the Penetration Depth in YBa₂Cu₃O_{7-x} and YBa₂Cu₄O₈ Superconductors". *Physical review letters* 74.4 (1995), p. 598.
- [25] S. Johnson et al. "Flux-Line Lattice Structures in Untwinned YBa₂Cu₃O_{7-δ}". *Physical review letters* 82.13 (1999), p. 2792.
- [26] D. Lu et al. "Superconducting gap and strong in-plane anisotropy in untwinned YBa₂Cu₃O_{7-δ}". *Physical review letters* 86.19 (2001), p. 4370.
- [27] R. Arpaia et al. "Untwinned YBa₂Cu₃O_{7-δ} thin films on MgO substrates: A platform to study strain effects on the local orders in cuprates". *Physical Review Materials* 3.11 (2019), p. 114804.
- [28] R. Liang, D. Bonn, and W. Hardy. "Evaluation of CuO₂ plane hole doping in YBa₂Cu₃O_{6+x} single crystals". *Physical Review B* 73.18 (2006), p. 180505.
- [29] J. R. Schrieffer and J. S. Brooks. *Handbook of high-temperature superconductivity: theory and experiment*. Springer, 2007.
- [30] D. J. Van Harlingen. "Phase-sensitive tests of the symmetry of the pairing state in the high-temperature superconductors—evidence for d_{x2-y2} symmetry". *Reviews of Modern Physics* 67.2 (1995), p. 515.
- [31] C. Tsuei and J. Kirtley. "Pairing symmetry in cuprate superconductors". *Reviews of Modern Physics* 72.4 (2000), p. 969.
- [32] D. Gustafsson, D. Golubev, M. Fogelström, T. Claeson, S. Kubatkin, T. Bauch, and F. Lombardi. "Fully gapped superconductivity in a nanometre-size YBa₂Cu₃O_{7-δ} island enhanced by a magnetic field". *Nature nanotechnology* 8.1 (2013), pp. 25–30.
- [33] J. Tranquada, B. Sternlieb, J. Axe, Y. Nakamura, and S. Uchida. "Evidence for stripe correlations of spins and holes in copper oxide superconductors". *nature* 375.6532 (1995), p. 561.
- [34] C. Varma, P. B. Littlewood, S. Schmitt-Rink, E. Abrahams, and A. Ruckenstein. "Phenomenology of the normal state of Cu-O high-temperature superconductors". *Physical Review Letters* 63.18 (1989), p. 1996.
- [35] T. Timusk and B. Statt. "The pseudogap in high-temperature superconductors: an experimental survey". *Reports on Progress in Physics* 62.1 (1999), p. 61.
- [36] S. Chakravarty, H.-Y. Kee, and K. Völker. "An explanation for a universality of transition temperatures in families of copper oxide superconductors". *Nature* 428.6978 (2004), p. 53.
- [37] J. Chang et al. "Direct observation of competition between superconductivity and charge density wave order in YBa₂Cu₃O_{6.67}". *Nature Physics* 8.12 (2012), p. 871.
- [38] E. H. da Silva Neto et al. "Charge ordering in the electron-doped superconductor Nd_{2-x}CexCuO₄". *Science* 347.6219 (2015), pp. 282–285.
- [39] J. Tranquada et al. "Evidence for unusual superconducting correlations coexisting with stripe order in La_{1.875}Ba_{0.125}CuO₄". *Physical Review B* 78.17 (2008), p. 174529.
- [40] C. V. Parker et al. "Fluctuating stripes at the onset of the pseudogap in the high-T_c superconductor Bi₂Sr₂CaCu₂O_{8+x}". *Nature* 468.7324 (2010), p. 677.
- [41] S. Caprara, C. Di Castro, G. Seibold, and M. Grilli. "Dynamical charge density waves rule the phase diagram of cuprates". *Physical Review B* 95.22 (2017), p. 224511.
- [42] S. A. Kivelson, E. Fradkin, and V. J. Emery. "Electronic liquid-crystal phases of a doped Mott insulator". *Nature* 393.6685 (1998), pp. 550–553.
- [43] E. Carlson, V. Emery, S. Kivelson, and D. Orgad. "Concepts in high temperature superconductivity". In: *Superconductivity*. Springer, 2008, pp. 1225–1348.

- [44] R. Arpaia et al. “Dynamical charge density fluctuations pervading the phase diagram of a Cu-based high-T_c superconductor”. *Science* 365.6456 (2019), pp. 906–910.
- [45] B. D. Josephson. “Possible new effects in superconductive tunnelling”. *Physics letters* 1.7 (1962), pp. 251–253.
- [46] J. Clarke and A. I. Braginski. *The SQUID handbook: Applications of SQUIDs and SQUID systems*. John Wiley & Sons, 2006.
- [47] H. Weinstock. *SQUID sensors: fundamentals, fabrication and applications*. Vol. 329. Springer Science & Business Media, 2012.
- [48] F. Müller, T. Scheller, R. Wendisch, R. Behr, O. Kieler, L. Palafox, and J. Kohlmann. “NbSi barrier junctions tuned for metrological applications up to 70 GHz: 20 V arrays for programmable Josephson voltage standards”. *IEEE Transactions on Applied Superconductivity* 23.3 (2012), pp. 1101005–1101005.
- [49] P. D. Dresselhaus, Y. Chong, J. H. Plantenberg, and S. P. Benz. “Stacked SNS Josephson junction arrays for quantum voltage standards”. *IEEE transactions on applied superconductivity* 13.2 (2003), pp. 930–933.
- [50] W.-T. Tsang and T. Van Duzer. “DC analysis of parallel arrays of two and three Josephson junctions”. *Journal of Applied Physics* 46.10 (1975), pp. 4573–4580.
- [51] K. Hasselbach, D. Mailly, and J. Kirtley. “Micro-superconducting quantum interference device characteristics”. *Journal of applied physics* 91.7 (2002), pp. 4432–4437.
- [52] M. Faucher, T. Fournier, B. Pannetier, C. Thirion, W. Wernsdorfer, J. Villegier, and V. Bouchiat. “Niobium and niobium nitride SQUIDs based on anodized nanobridges made with an atomic force microscope”. *Physica C: Superconductivity* 368.1-4 (2002), pp. 211–217.
- [53] G. Podd, G. Hutchinson, D. Williams, and D. Hasko. “Micro-SQUIDs with controllable asymmetry via hot-phonon controlled junctions”. *Physical Review B* 75.13 (2007), p. 134501.
- [54] R. H. Koch, J. Clarke, W. Goubau, J. M. Martinis, C. Pegrum, and D. J. Van Harlingen. “Flicker (1/f) noise in tunnel junction dc SQUIDS”. *Journal of low temperature physics* 51.1-2 (1983), pp. 207–224.
- [55] V. Foglietti, W. Gallagher, M. Ketchen, A. Kleinsasser, R. Koch, S. Raider, and R. Sandstrom. “Low-frequency noise in low 1/f noise dc SQUID’s”. *Applied physics letters* 49.20 (1986), pp. 1393–1395.
- [56] J. Malmivuo, J. Lekkala, P. Kontro, L. Suomaa, and H. Vihinen. “Improvement of the properties of an eddy current magnetic shield with active compensation”. *Journal of Physics E: Scientific Instruments* 20.2 (1987), p. 151.
- [57] H. J. ter Brake, H. Wieringa, and H. Rogalla. “Improvement of the performance of a mu-metal magnetically shielded room by means of active compensation (biomagnetic applications)”. *Measurement Science and Technology* 2.7 (1991), p. 596.
- [58] R. Koch, J. Sun, V. Foglietti, and W. Gallagher. “Flux dam, a method to reduce extra low frequency noise when a superconducting magnetometer is exposed to a magnetic field”. *Applied physics letters* 67.5 (1995), pp. 709–711.
- [59] E. Dantsker, S. Tanaka, P.-Å. Nilsson, R. Kleiner, and J. Clarke. “Reduction of 1/f noise in high-T_c dc superconducting quantum interference devices cooled in an ambient magnetic field”. *Applied physics letters* 69.26 (1996), pp. 4099–4101.
- [60] E. Dantsker, S. Tanaka, and J. Clarke. “High-T_c super conducting quantum interference devices with slots or holes: Low 1/f noise in ambient magnetic fields”. *Applied physics letters* 70.15 (1997), pp. 2037–2039.
- [61] C. D. Tesche and J. Clarke. “dc SQUID: Noise and optimization”. *Journal of Low Temperature Physics* 29.3 (1977), pp. 301–331.
- [62] M. Faley, U. Poppe, K. Urban, and R. Fagaly. “Noise analysis of DC SQUIDs with damped superconducting flux transformers”. *Journal of Physics: Conference Series*. Vol. 234. 4. IOP Publishing, 2010, p. 042009.
- [63] H. Hilgenkamp, H.-J. H. Smilde, D. H. Blank, G. Rijnders, H. Rogalla, J. R. Kirtley, C. C. Tsuei, et al. “Ordering and manipulation of the magnetic moments in large-scale superconducting π -loop arrays”. *Nature* 422.6927 (2003), pp. 50–53.
- [64] H. Hilgenkamp and J. Mannhart. “Grain boundaries in high-T_c superconductors”. *Reviews of Modern Physics* 74.2 (2002), p. 485.

- [65] D. Dimos, P. Chaudhari, J. Mannhart, and F. LeGoues. “Orientation Dependence of Grain-Boundary Critical Currents in Y Ba₂ Cu₃ O_{7-δ} Bicrystals”. *Physical Review Letters* 61.2 (1988), p. 219.
- [66] K. Daly, W. Dozier, J. Burch, S. Coons, R. Hu, C. Platt, and R. Simon. “Substrate step-edge YBa₂Cu₃O₇ rf SQUIDs”. *Applied physics letters* 58.5 (1991), pp. 543–545.
- [67] K. Char, M. Colclough, S. Garrison, N. Newman, and G. Zaharchuk. “Bi-epitaxial grain boundary junctions in YBa₂Cu₃O₇”. *Applied physics letters* 59.6 (1991), pp. 733–735.
- [68] M. Faley et al. “High-Tc SQUID biomagnetometers”. *Superconductor Science and Technology* 30.8 (2017), p. 083001.
- [69] U. Poppe, Y. Divin, M. Faley, J. Wu, C. Jia, P. Shadrin, and K. Urban. “Properties of YBa₂/Cu₃O₇/thin films deposited on substrates and bicrystals with vicinal offcut and realization of high I_c/R_n/junctions”. *IEEE transactions on applied superconductivity* 11.1 (2001), pp. 3768–3771.
- [70] B. Müller et al. “Josephson Junctions and SQUIDS Created by Focused Helium-Ion-Beam Irradiation of Y Ba₂ Cu₃ O₇”. *Physical Review Applied* 11.4 (2019), p. 044082.
- [71] G. Clark, A. Marwick, R. Koch, and R. Laibowitz. “Effects of radiation damage in ion-implanted thin films of metal-oxide superconductors”. *Applied Physics Letters* 51.2 (1987), pp. 139–141.
- [72] S. A. Cybart, E. Cho, T. Wong, B. H. Wehlin, M. K. Ma, C. Huynh, and R. Dynes. “Nano Josephson superconducting tunnel junctions in YBa₂ Cu₃ O_{7-δ} directly patterned with a focused helium ion beam”. *Nat. Nanotech.* 10.7 (2015), p. 598.
- [73] S. Tinchev. “High-T_c/SQUIDS with local oxygen-ion irradiated weak links”. *IEEE transactions on applied superconductivity* 3.1 (1993), pp. 28–32.
- [74] N. Bergeal, X. Grison, J. Lesueur, G. Faini, M. Aprili, and J. Contour. “High-quality planar high-T_c Josephson junctions”. *Appl. Phys. Lett.* 87.10 (2005), p. 102502.
- [75] K. Chen, S. A. Cybart, and R. Dynes. “Planar thin film YBa₂ Cu₃ O_{7-δ} Josephson junction pairs and arrays via nanolithography and ion damage”. *Applied physics letters* 85.14 (2004), pp. 2863–2865.
- [76] E. Cho et al. “YBa₂Cu₃O_{7-δ} superconducting quantum interference devices with metallic to insulating barriers written with a focused helium ion beam”. *Appl. Phys. Lett.* 106.25 (2015), p. 252601.
- [77] E. Y. Cho, H. Li, J. C. LeFebvre, Y. W. Zhou, R. Dynes, and S. A. Cybart. “Direct-coupled micro-magnetometer with Y-Ba-Cu-O nano-slit SQUID fabricated with a focused helium ion beam”. *Applied physics letters* 113.16 (2018), p. 162602.
- [78] P. Anderson and A. Dayem. “Radio-frequency effects in superconducting thin film bridges”. *Physical Review Letters* 13.6 (1964), p. 195.
- [79] S. Nawaz, R. Arpaia, T. Bauch, and F. Lombardi. “Approaching the theoretical depairing current in YBa₂Cu₃O_{7-x} nanowires”. *Physica C Supercond* 495 (2013), pp. 33–38.
- [80] R. Arpaia et al. “High-temperature superconducting nanowires for photon detection”. *Physica C: Superconductivity and its Applications* 509 (2015), pp. 16–21.
- [81] T. Schwarz et al. “Low-noise YBa₂ Cu₃ O₇ nano-SQUIDs for performing magnetization-reversal measurements on magnetic nanoparticles”. *Phys. Rev. Appl.* 3.4 (2015), p. 044011.
- [82] J. Nagel et al. “Resistively shunted YBa₂Cu₃O₇ grain boundary junctions and low-noise SQUIDs patterned by a focused ion beam down to 80 nm linewidth”. *Superconductor Science and Technology* 24.1 (2010), p. 015015.
- [83] J. Schneider, H. Kohlstedt, and R. Wördenweber. “Nanobridges of optimized YBa₂Cu₃O₇ thin films for superconducting flux-flow type devices”. *Applied physics letters* 63.17 (1993), pp. 2426–2428.
- [84] R. Barth, B. Spangenberg, C. Jaekel, H. G. Roskos, H. Kurz, and B. Holzapfel. “Optimization of YBa₂Cu₃O_{7-δ} submicrometer structure fabrication”. *Applied physics letters* 63.8 (1993), pp. 1149–1151.
- [85] H. Assink et al. “Critical currents in submicron YBa₂/Cu₃O₇/lines”. *IEEE transactions on applied superconductivity* 3.1 (1993), pp. 2983–2985.
- [86] A. van der Harg, E. van der Drift, and P. Hadley. “Deep-submicron structures in YBCO: fabrication and measurements”. *IEEE Transactions on Applied Superconductivity* 5.2 (1995), pp. 1448–1451.

- [87] J. Schneider, M. Mück, and R. Wördenweber. “DC SQUIDs based upon YBa₂Cu₃O₇ nanobridges”. *Applied physics letters* 65.19 (1994), pp. 2475–2477.
- [88] M. Pedyash, D. H. Blank, and H. Rogalla. “Superconducting quantum interference devices based on YBaCuO nanobridges”. *Applied physics letters* 68.8 (1996), pp. 1156–1158.
- [89] S. Nawaz, R. Arpaia, F. Lombardi, and T. Bauch. “Microwave Response of Superconducting Y Ba 2 Cu 3 O 7- δ Nanowire Bridges Sustaining the Critical Depairing Current: Evidence of Josephson-like Behavior”. *Phys. Rev. Lett.* 110.16 (2013), p. 167004.
- [90] R. Arpaia, S. Nawaz, F. Lombardi, and T. Bauch. “Improved nanopatterning for YBCO nanowires approaching the depairing current”. *IEEE Transactions on Applied Superconductivity* 23.3 (2013), pp. 1101505–1101505.
- [91] R. Bagdadi. *YBa₂Cu₃O_{7-γ} Nanogaps: A Path Toward Hybrid Junctions*. Chalmers University of Technology, 2017.
- [92] R. Arpaia et al. “Resistive state triggered by vortex entry in YBa₂Cu₃O_{7- δ} nanostructures”. *Physica C: Superconductivity and its Applications* 506 (2014), pp. 165–168.
- [93] R. Arpaia, M. Arzeo, R. Baghdadi, E. Trabaldo, F. Lombardi, and T. Bauch. “Improved noise performance of ultrathin YBCO Dayem bridge nanoSQUIDs”. *Supercond. Sci. Technol.* 30.1 (2016), p. 014008.
- [94] M. J. Martinez-Pérez and D. Koelle. “NanoSQUIDs: Basics & recent advances”. *Phys. Sci. Rev.* 2.8 (2016).
- [95] E. Trabaldo, R. Arpaia, M. Arzeo, E. Andersson, D. Golubev, F. Lombardi, and T. Bauch. “Transport and noise properties of YBCO nanowire based nanoSQUIDs”. *Superconductor Science and Technology* 32.7 (2019), p. 073001.
- [96] T. Van Duzer and C. W. Turner. “Principles of superconductive devices and circuits” (1981).
- [97] L. Aslamazov and A. Larkin. “Josephson effect in superconducting point contacts”. *ZhETF Pisma Redaktsiiu* 9 (1969), p. 150.
- [98] K. K. Likharev and L. A. Yakobson. “Steady state properties of superconducting bridges”. *Sov. Phys. Tech. Phys.* 20 (1976), pp. 950–954.
- [99] K. Likharev. “Superconducting weak links”. *Reviews of Modern Physics* 51.1 (1979), p. 101.
- [100] R. Vijay, E. Levenson-Falk, D. Slichter, and I. Siddiqi. “Approaching ideal weak link behavior with three dimensional aluminum nanobridges”. *Applied Physics Letters* 96.22 (2010), p. 223112.
- [101] F. Tafuri et al. “Dissipation in ultra-thin current-carrying superconducting bridges; evidence for quantum tunneling of Pearl vortices”. *EPL (Europhysics Letters)* 73.6 (2006), p. 948.
- [102] C. Bean and J. Livingston. “Surface barrier in type-II superconductors”. *Physical Review Letters* 12.1 (1964), p. 14.
- [103] L. Bulaevskii, M. Graf, C. Batista, and V. Kogan. “Vortex-induced dissipation in narrow current-biased thin-film superconducting strips”. *Physical Review B* 83.14 (2011), p. 144526.
- [104] D. Y. Vodolazov, I. Maksimov, and E. Brandt. “Modulation instability of the order parameter in thin-film superconductors with edge barrier”. *EPL (Europhysics Letters)* 48.3 (1999), p. 313.
- [105] E. Trabaldo et al. “Grooved Dayem nanobridges as building blocks of high-performance YBa₂Cu₃O_{7- δ} SQUID magnetometers”. *Nano letters* 19.3 (2019), pp. 1902–1907.
- [106] E. Trabaldo et al. “SQUID magnetometer based on Grooved Dayem nanobridges and a flux transformer”. *arXiv preprint arXiv:1908.09875* (2019).
- [107] E. Trabaldo et al. “Properties of Grooved Dayem Bridge based YBa₂Cu₃O_{7- δ} Superconducting Quantum Interference Devices and Magnetometers”. *arXiv preprint arXiv:2001.08554* (2020).
- [108] D. M. Manos and D. L. Flamm. *Plasma etching: an introduction*. Elsevier, 1989.
- [109] G. Alvarez, K. Taylor, and G. Russell. “Josephson behaviour of variable thickness bridges in textured YBa₂Cu₃O_{7- δ}”. *Physica C: Superconductivity* 165.3-4 (1990), pp. 258–264.
- [110] R. Arpaia et al. “Transport properties of ultrathin YBa 2 Cu 3 O 7- δ nanowires: A route to single-photon detection”. *Physical Review B* 96.6 (2017), p. 064525.
- [111] E. Mitchell et al. “2D SQIF arrays using 20 000 YBCO high R n Josephson junctions”. *Supercond. Sci. Technol.* 29.6 (2016), 06LT01.
- [112] T. Wolf, N. Bergeal, J. Lesueur, C. J. Fourie, G. Faini, C. Ulysse, and P. Febvre. “YBCO Josephson junctions and striplines for RSFQ circuits made by ion irradiation”. *IEEE Transactions on applied superconductivity* 23.2 (2013), pp. 1101205–1101205.

- [113] S. A. Cybart et al. “Large voltage modulation in magnetic field sensors from two-dimensional arrays of Y-Ba-Cu-O nano Josephson junctions”. *Applied Physics Letters* 104.6 (2014), p. 062601.
- [114] V. Kornev, I. Soloviev, N. Klenov, A. Sharafiev, and O. Mukhanov. “Array designs for active electrically small superconductive antennas”. *Physica C: Superconductivity* 479 (2012), pp. 119–122.
- [115] W. Wernsdorfer. “From micro-to nano-SQUIDs: applications to nanomagnetism”. *Superconductor Science and Technology* 22.6 (2009), p. 064013.
- [116] W. Wernsdorfer, K. Hasselbach, D. Mailly, B. Barbara, A. Benoit, L. Thomas, and G. Suran. “DC-SQUID magnetization measurements of single magnetic particles”. In: *Quantum Tunneling of Magnetization—QTM'94*. Springer, 1995, pp. 227–241.
- [117] D. Drung. “High-Tc and low-Tc dc SQUID electronics”. *Supercond. Sci. Technol.* 16.12 (2003), p. 1320.
- [118] S. Ruffieux et al. “The role of kinetic inductance on the performance of YBCO SQUID magnetometers”. *Superconductor Science and Technology* (2019).
- [119] F. Öisjöen et al. “High-T c superconducting quantum interference device recordings of spontaneous brain activity: Towards high-T c magnetoencephalography”. *Appl. Phys. Lett.* 100.13 (2012), p. 132601.
- [120] M. Faley et al. “High-Tc DC SQUIDS for magnetoencephalography”. *IEEE Trans. Appl. Supercond.* 23.3 (2013), pp. 1600705–1600705.
- [121] M. Chukharkin et al. “Improvement of ultra-low field magnetic resonance recordings with a multilayer flux-transformer-based high-Tc SQUID magnetometer”. *IEEE Trans. Appl. Supercond.* 23.3 (2013).
- [122] E. Mitchell and C. Foley. “YBCO step-edge junctions with high I_{cRn} ”. *Supercond. Sci. Technol.* 23.6 (2010), p. 065007.
- [123] M. Faley, D. Meertens, U. Poppe, and R. Dunin-Borkowski. “Graphoepitaxial high-Tc SQUIDS”. *Journal of Physics: Conference Series*. Vol. 507. 4. IOP Publishing. 2014, p. 042009.
- [124] J. Bardeen. “Critical fields and currents in superconductors”. *Reviews of modern physics* 34.4 (1962), p. 667.
- [125] M. Beasley, J. Mooij, and T. Orlando. “Possibility of vortex-antivortex pair dissociation in two-dimensional superconductors”. *Physical Review Letters* 42.17 (1979), p. 1165.
- [126] H. Bartolf, A. Engel, A. Schilling, K. Il'In, M. Siegel, H.-W. Hübers, and A. Semenov. “Current-assisted thermally activated flux liberation in ultrathin nanopatterned NbN superconducting meander structures”. *Physical Review B* 81.2 (2010), p. 024502.
- [127] J. Johansson, K. Cedergren, T. Bauch, and F. Lombardi. “Properties of inductance and magnetic penetration depth in (103)-oriented $\text{YBa}_2\text{Cu}_3\text{O}_{7-\delta}$ thin films”. *Phys. Rev. B* 79.21 (2009), p. 214513.
- [128] D. Koelle, R. Kleiner, F. Ludwig, E. Dantsker, and J. Clarke. “High-transition-temperature superconducting quantum interference devices”. *Reviews of Modern Physics* 71.3 (1999), p. 631.
- [129] R. Fischer, F. Longo, P. Nielsen, R. Engelhardt, R. C. Hider, and A. Piga. “Monitoring long-term efficacy of iron chelation therapy by deferiprone and desferrioxamine in patients with β -thalassaemia major: application of SQUID biomagnetic liver susceptometry”. *British journal of haematology* 121.6 (2003), pp. 938–948.
- [130] M. Faley et al. “Magnetoencephalography using a Multilayer hightc DC SQUID Magnetometer”. *Physics Procedia* 36 (2012), pp. 66–71.
- [131] H. Koch. “SQUID magnetocardiography: Status and perspectives”. *IEEE Trans. Appl. Supercond.* 11.1 (2001), pp. 49–59.
- [132] H.-C. Yang, H.-E. Horng, S.-Y. Yang, and S.-H. Liao. “Advances in biomagnetic research using high-Tc superconducting quantum interference devices”. *Superconductor Science and Technology* 22.9 (2009), p. 093001.
- [133] B. P. Weiss, E. A. Lima, L. E. Fong, and F. J. Baudenbacher. “Paleomagnetic analysis using SQUID microscopy”. *Journal of Geophysical Research: Solid Earth* 112.B9 (2007).
- [134] C. P. Foley et al. “Field trials using HTS SQUID magnetometers for ground-based and airborne geophysical applications”. *IEEE transactions on applied superconductivity* 9.2 (1999), pp. 3786–3792.

- [135] V. Glyantsev, Y. Tavrin, W. Zander, J. Schubert, and M. Siegel. “The stability of dc and rf SQUIDs in static ambient fields”. *Superconductor Science and Technology* 9.4A (1996), A105.
- [136] F. Ludwig, J. Beyer, D. Drung, S. Bechstein, and T. Schurig. “High-performance high-T/sub c/SQUID sensors for multichannel systems in magnetically disturbed environment”. *IEEE transactions on applied superconductivity* 9.2 (1999), pp. 3793–3796.
- [137] E. Dantsker et al. “Addendum:“Low noise $\text{YBa}_2\text{Cu}_3\text{O}_{7-\delta}$ - x-SrTiO_3 - $\text{YBa}_2\text{Cu}_3\text{O}_{7-\delta}$ - x multilayers for improved superconducting magnetometers”[Appl. Phys. Lett. 66, 373 (1995)]”. *Applied Physics Letters* 67.5 (1995), pp. 725–726.
- [138] M. Xie. *Development of high-Tc SQUID magnetometers for on-scalp MEG*. Chalmers University of Technology, 2017.
- [139] M. Chukharkin, A. Kalabukhov, J. F. Schneiderman, F. Öisjöen, O. Snigirev, Z. Lai, and D. Winkler. “Noise properties of high-Tc superconducting flux transformers fabricated using chemical-mechanical polishing”. *Applied Physics Letters* 101.4 (2012), p. 042602.
- [140] J. E. Knuutila et al. “A 122-channel whole-cortex SQUID system for measuring the brain’s magnetic fields”. *IEEE transactions on magnetics* 29.6 (1993), pp. 3315–3320.
- [141] J. F. Schneiderman. “Information content with low-vs. high-Tc SQUID arrays in MEG recordings: The case for high-Tc SQUID-based MEG”. *J. Neurosci. Methods* 222 (2014), pp. 42–46.
- [142] N. A. Masluk, I. M. Pop, A. Kamal, Z. K. Minev, and M. H. Devoret. “Microwave characterization of Josephson junction arrays: implementing a low loss superinductance”. *Physical review letters* 109.13 (2012), p. 137002.
- [143] P. K. Day, H. G. LeDuc, B. A. Mazin, A. Vayonakis, and J. Zmuidzinas. “A broadband superconducting detector suitable for use in large arrays”. *Nature* 425.6960 (2003), p. 817.
- [144] J. Sydow, D. Chamberlain, R. Buhrman, K. Char, and B. Moeckly. “Electromigration study of SNS ramp edge Josephson junctions”. *Applied superconductivity* 6.10-12 (1999), pp. 511–517.
- [145] B. Moeckly, D. Lathrop, and R. Buhrman. “Electromigration study of oxygen disorder and grain-boundary effects in $\text{YBa}_2\text{Cu}_3\text{O}_{7-\delta}$ thin films”. *Physical Review B* 47.1 (1993), p. 400.
- [146] X. D. Baumans, A. Fernández-Rodríguez, N. Mestres, S. Collienne, J. Van de Vondel, A. Palau, and A. V. Silhanek. “Electromigration in the dissipative state of high-temperature superconducting bridges”. *Applied Physics Letters* 114.1 (2019), p. 012601.
- [147] O. Cyr-Choinière et al. “Two types of nematicity in the phase diagram of the cuprate superconductor $\text{YBa}_2\text{Cu}_3\text{O}_y$ ”. *Physical Review B* 92.22 (2015), p. 224502.
- [148] Y. Sato et al. “Thermodynamic evidence for a nematic phase transition at the onset of the pseudogap in $\text{YBa}_2\text{Cu}_3\text{O}_y$ ”. *Nature Physics* 13.11 (2017), p. 1074.
- [149] E. W. Carlson, K. A. Dahmen, E. Fradkin, and S. Kivelson. “Hysteresis and noise from electronic nematicity in high-temperature superconductors”. *Physical review letters* 96.9 (2006), p. 097003.
- [150] E. Carlson and K. A. Dahmen. “Using disorder to detect locally ordered electron nematics via hysteresis”. *Nature communications* 2.1 (2011), pp. 1–6.
- [151] J. Bonetti, D. Caplan, D. J. Van Harlingen, and M. Weissman. “Electronic transport in under-doped $\text{YBa}_2\text{Cu}_3\text{O}_{7-\delta}$ nanowires: evidence for fluctuating domain structures”. *Physical review letters* 93.8 (2004), p. 087002.
- [152] D. S. Caplan, V. Orlyanchik, M. B. Weissman, D. J. Van Harlingen, E. Fradkin, M. Hinton, and T. R. Lemberger. “Anomalous Noise in the Pseudogap Regime of $\text{YBa}_2\text{Cu}_3\text{O}_{7-\delta}$ ”. *Physical review letters* 104.17 (2010), p. 177001.
- [153] R. Arpaia, E. Andersson, E. Trabaldo, T. Bauch, and F. Lombardi. “Probing the phase diagram of cuprates with $\text{YBa}_2\text{Cu}_3\text{O}_{7-\delta}$ thin films and nanowires”. *Phys. Rev. Mater.* 2.2 (2018), p. 024804.
- [154] S. Kogan. *Electronic noise and fluctuations in solids*. Cambridge University Press, 2008.
- [155] F. Hooge. “ $1/f$ noise”. *Physica B + C* 83.1 (1976), pp. 14–23.
- [156] E. Trabaldo, M. Arzeo, R. Arpaia, R. Baghdadi, E. Andersson, F. Lombardi, and T. Bauch. “Noise properties of YBCO Nanostructures”. *IEEE Trans. Appl. Supercond.* 27.4 (2017).
- [157] J. A. Testa, Y. Song, X.-D. Chen, J. Golben, S.-I. Lee, B. R. Patton, and J. R. Gaines. “ $1/f$ noise-power measurements of copper oxide superconductors in the normal and superconducting states”. *Physical Review B* 38.4 (1988), p. 2922.

- [158] S. Scouten, Y. Xu, B. Moeckly, and R. Buhrman. “Low-frequency noise in the normal state of thin-film high-temperature superconductors”. *Physical Review B* 50.21 (1994), p. 16121.
- [159] Y. Song, A. Misra, P. Crooker, and J. R. Gaines. “ $1/f$ noise and morphology of $\text{YBa}_2\text{Cu}_3\text{O}_{7-\delta}$ single crystals”. *Physical review letters* 66.6 (1991), p. 825.
- [160] Y. Feng, Z. Dian-Lin, and X. Ji-Wu. “Thermally activated behavior of $1/f$ noise in $\text{YBa}_2\text{Cu}_3\text{O}_{7-\delta}$ ”. *Physical Review B* 51.2 (1995), p. 1334.
- [161] L. Liu, K. Zhang, H. Jaeger, D. Buchholz, and R. Chang. “Normal-state resistance fluctuations in high-T_c cuprate films”. *Physical Review B* 49.5 (1994), p. 3679.
- [162] K. Han, S.-I. Lee, S.-H. S. Salk, H. Shin, S. H. Lee, and J. K. Ku. “Enhancement of the noise spectral densities near the resistive transition region of YBCO micro-bridge”. *Solid state communications* 81.3 (1992), pp. 269–273.
- [163] Y. Bei, Y. Gao, J. Kang, G. Lian, X. Hu, G. Xiong, and S. Yan. “Size effect of $1/f$ noise in the normal state of $\text{YBa}_2\text{Cu}_3\text{O}_{7-\delta}$ ”. *Physical Review B* 61.2 (2000), p. 1495.
- [164] A. Miklich, D. Koelle, E. Dantsker, D. Nemeth, J. Kingston, R. Kromann, and J. Clarke. “Bicrystal YBCO DC SQUIDs with low noise”. *IEEE transactions on applied superconductivity* 3.1 (1993), pp. 2434–2437.
- [165] M. Heideman, D. Johnson, and C. Burrus. “Gauss and the history of the fast Fourier transform”. *IEEE ASSP Magazine* 1.4 (1984), pp. 14–21.
- [166] M. Sampietro, L. Fasoli, and G. Ferrari. “Spectrum analyzer with noise reduction by cross-correlation technique on two channels”. *Review of scientific instruments* 70.5 (1999), pp. 2520–2525.
- [167] P. Dutta, P. Dimon, and P. Horn. “Energy scales for noise processes in metals”. *Physical Review Letters* 43.9 (1979), p. 646.
- [168] F. Herbstritt, T. Kemen, L. Alff, A. Marx, and R. Gross. “Transport and noise characteristics of submicron high-temperature superconductor grain-boundary junctions”. *Applied Physics Letters* 78.7 (2001), pp. 955–957.